NTNU

Norwegian University of
Science and Technology

# Synthesis and Properties of $YBaCo_2O_{5+\delta}$ for Solid Oxide Fuel Cell Cathodes

Simon Lindau Jørgensen

Materials Science and Engineering
Submission date: July 2016
Supervisor: Tor Grande, IMTE
Co-supervisor: Carlos Bernuy-Lopez, IMTE

Norwegian University of Science and Technology
Department of Materials Science and Engineering

# Description of Thesis

This is the description given from supervisor Tor Grande before the thesis was initiated.

**Synthesis and Properties of $YBaCo_2O_{5+\delta}$ for Solid Oxide Fuel Cell Cathodes**

In this thesis cathodes of $YBaCo_2O_{5+\delta}$ will be investigated to see if they can enhance the performance in fuel cells where $BaZrO_3$ based proton conductors are used as electrolyte. $YBaCo_2O_{5+\delta}$ can potentially have both a high electronic conductivity combined with high ionic conductivity of oxygen ions and protons. Especially the proton conductivity of the cathode will reduce the cathodic overpotential and enhance the performance of the fuel cell. This thesis will characterise the cathodic properties of YB. This includes high temperature XRD, thermogravimetry, dillatommetry, conductivity as well as impedance spectroscopy to determine area specific resistance as indirect measure of proton conductivity.

# Preface

This master thesis was conducted as a part of the degree in Materials Science, with specialisation in Materials for Energy Technology, at Norwegian University of Science and Technology (NTNU). The master work leading to the thesis was conducted spring 2016 as a continuation of the project "Synthesis and properties of $YBaCo_2O_{5+\delta}$ for solid oxide fuel cell cathodes" conducted fall 2015.

I would like to thank my supervisor Tor Grande and co-supervisor Carlos Bernuy Lopez for fruitful discussions, guidance and support. Further I want to thank Technical Staff at the Institute for practical help with equipment and experiments, and Ph.D. students Singh, Kanas and Rokas for practical ideas and motivation throughout my work. Tolchard also deserves thanks for all XRD related questions he thoroughly answered. At last I want to thank my wife Sandra for support and proof reading.

# Abstract

The layered double perovskite $YBaCo_2O_{5+\delta}$ was synthesised and characterised. The synthesis was done by solid-state reaction with several calcination steps at temperatures between 1000 °C and 1130 °C. The structure was investigated at elevated temperatures, from room temperature to 800 °C, in oxygen, air and nitrogen using X-ray diffraction. The oxygen content, $5+\delta$, was determined by thermogravimetric analysis in the same atmospheres from room temperature and up to 1100 °C.

The crystal structure of $YBaCo_2O_{5+\delta}$ at room temperature is orthorhombic (space group Pmmm) with ordered oxygen vacancies and alternating layers of yttrium and barium. Oxygen content, $5+\delta$, was determined to 5.42, thus showing large oxygen deficiency compared to the stoichiometric compound $LnBaM_2O_6$. Heating of the material induces a phase transition to a tetragonal (space group P4/mmm) oxygen disordered phase. Heating in both nitrogen and oxygen causes decomposition. In oxygen decomposition to single perovskites occur above 600 °C:

$$YBaCo_2O_{5+\delta} + O_2 \longrightarrow YCoO_3 + BaCo_{3-\delta}$$

At approximately 925 °C the reaction is reversed and $YBaCo_2O_{5+\delta}$ forms again. In nitrogen, decomposition results in both primary and ternary oxides according to:

$$YBaCo_2O_{5+\delta} \longrightarrow YBaCo_4O_7 + Y_2O_3 + BaCo_xY_{1-x}O_{3-\delta} + O_2.$$

No sign of secondary phases was seen during high temperature XRD in air, but annealing at 800 °C caused decomposition as seen in oxygen.

Thermal expansion coefficient of $YBaCo_2O_{5+\delta}$ in oxygen, air and nitrogen, for temperatures between 500 °C and 700 °C, was respectively, $18.6 \times 10^{-6}\,K^{-1}$, $15.9 \times 10^{-6}\,K^{-1}$ and $17.0 \times 10^{-6}\,K^{-1}$ in direction $a$ and $19.2 \times 10^{-6}\,K^{-1}$, $25.3 \times 10^{-6}\,K^{-1}$ and $27.0 \times 10^{-6}\,K^{-1}$ in direction $c$ . The isotropic thermal expansion based on volumetric thermal expansion was determined to $20.0 \times 10^{-6}\,K^{-1}$ for all atmospheres.

# Sammendrag

Den lagdelte doble perovskitten $YBaCo_2O_{5+\delta}$ har i denne oppgaven blitt fremstilt og karakterisert. Syntesen ble gjort ved å bruke faststoffmetoden med flere (fem) kalsineringssteg ved temperaturer mellom 1000 °C og 1130 °C. Krystallstruktur til $YBaCo_2O_{5+\delta}$ ble undersøkt med røntgendiffraksjon i oksygen-, luft- og nitrogenatmosfære fra romtemperatur til 800 °C. Oksygeninnholdet, $5+\delta$, ble bestemt ved hjelp av termogravimetrisk analyse i de samme atmosfærene fra romtemperatur opp til 1100 °C.

Resultatene viser at krystallstrukturen til $YBaCo_2O_{5+\delta}$ ved romtemperatur er ortorombisk (Pmmm) med både ordnede oksygenvakanser og ordnede lag av yttrium og barium. Oksygeninnholdet, $5+\delta$, ble bestemt til 5.42 ved hjelp av ex situ TGA. Stoffet har dermed betydelig oksygenunderskudd sammenlignet med støkiometrisk $LnBaM_2O_6$. Oppvarming av materialet fører til en overgang til en tetragonal fase (P4/mmm) med uordnede vakanser i yttriumlaget. I oksygen dannes de to binære perovskittene ved 600 °C. Dekomponeringen kan beskrives med reaksjonslikning:

$$YBaCo_2O_{5+\delta} + O_2 \longrightarrow YCoO_3 + BaCo_{3-\delta}$$

Ved omtrent 925 °C reverseres reaksjonen og $YBaCo_2O_{5+\delta}$ gjendannes. I nitrogen dannes både primære- og ternære oksider. Dekomponeringen kan beskrives med reaksjonslikning:

$$YBaCo_2O_{5+\delta} \longrightarrow YBaCo_4O_7 + Y_2O_3 + BaCo_xY_{1-x}O_{3-\delta} + O_2.$$

Stoffet dekomponerte ikke under høytemperaturrøntgendiffraksjon i luft, men gløding ved 800 °C førte til samme dekomponeringsreaksjon som i oksygen.

Anisotrop termisk utvidelse til $YBaCo_2O_{5+\delta}$ i oksygen, luft og nitrogen, ved temperaturer mellom 500 °C og 700 °C, var henholdsvis, $18.6 \times 10^{-6}\,K^{-1}$, $15.9 \times 10^{-6}\,K^{-1}$ og $17.0 \times 10^{-6}\,K^{-1}$ i a-retning mens den i c-retning var $19.2 \times 10^{-6}\,K^{-1}$, $25.3 \times 10^{-6}\,K^{-1}$ og $27.0 \times 10^{-6}\,K^{-1}$. Den isotrope termiske utvidelsen beregnet fra volumetrisk termiskekspansjon ble bestemt til $20.0 \times 10^{-6}\,K^{-1}$ for alle atmosfærer.

# Contents

# List of Figures

# Chapter 1

# Introduction

## 1.1 Background

Two of the biggest challenges the world is facing today is the global warming and the so called terra watt challenge – providing trillions of watts of power to meet the growing energy demand of the world today and in the future.[8,9] Energy is a necessary resource for human progress, and more and more energy will therefore be needed, especially in developing countries.[9] Continuing relaying more and more on fossil fuel cannot continue due to their limited abundance and emissions. New technologies are needed to meet the growing demand of energy and to reduce emissions.

Internal combustion engines usually have an overall efficiency of 20 – 30 %, thus wasting a huge fraction of the thermal energy.[9] Combustion engines are limited by Carnot efficiency, whereas fuel cells which are not thermal engines, but electrochemical energy conversion units have higher theoretical efficiencies. In combined heat and power plants the theoretical efficiency is about 80 %.[10] Employing fuel cells can thus significantly reduce emissions and fuel costs. Fuel cells are proposed to play a vital role in the future energy picture, both for storing renewable energy and for efficient combustion of fossil fuels.

The history of fuel cells goes back to 1839 with the invention of William Grove's gas battery, the first fuel cell.[11,12] In 1905 F. Haber got the first patent for a solid oxide fuel cell (SOFC).[13] In 1959 an alkaline 5kW fuel cell was demonstrated by Francis Bacon, and during the 1970s phosphoric acid fuel cell were developed prompted by the oil crisis. During the 1990s SOFCs were developed for commercial and industrial locations.[12] Today there are several different fuel cell technologies with different pros and cons. NASA used alkaline fuel cells in space missions already in the 1960s, but fuel cells should be affordable, not only for special use. During the years efficiency and cost has improved, but still more research is needed to make fuel cells more affordable.

The most promising technology for grid scale applications, and the focus of this thesis is SOFC. They do not possess a very corrosive electrolyte like the molten carbonate fuel cells,[14] neither is platinum group metal needed to catalyse the reaction, as other fuel cells need.[11,15,16] SOFCs are already in the market as power plants for

buildings giving cheaper electricity compared to grid (though subsidised).[17] SOFC can run on hydrocarbon fuels, this makes SOFC a technology feasible today and not only in a distant hydrogen society.[18] However, challenges are still to be resolved with SOFC.

To reduce the cost of fuel cells it is beneficial to use less expensive materials and improve the lifetime of the cell. However, conventional SOFCs run at high temperatures, approximately 1000 °C, causing reduced lifetime and material constraints. The high temperature is needed to make the electrolyte sufficiently conducting and to assure high activity of the electrodes, in particular the air electrode (cathode). By developing new electrode and electrolyte materials with decreased operational temperature, the widespread use of fuel cells necessary to influence the energy picture can be realised.

The conventional SOFCs today use cathodes made of lanthanum strontium manganite (LSM). This material is an excellent electronic conductor and has low activation energy for reduction of oxygen gas at 800-1000 °C. Below 700 °C the overpotential is too high, and other cathode materials have been developed to allow operation at lower temperatures. Two of the best cathode materials working at lower temperatures are lanthanum strontium cobalt ferrite (LSCF) and barium strontium cobalt ferrite (BSCF). These materials are called mixed ionic electronic conductors (MIECs) since they in addition to electrical conduction can conduct oxygen ions. This increase the area of reaction, thus reducing current density and overpotential.

A second aspect of reducing the operational temperature of fuel cells is the ionic conductivity of the electrolyte. The ohmic resistance of the electrolyte can be reduced either by making it thinner, or by using materials with higher ionic conductivity. Ceramic materials having higher oxygen conductivity than YSZ exists, but to significantly reduce the resistance at lower temperatures it has been proposed to use materials conducting protons rather than oxygen ions. Protons are much smaller than oxygen ions and show a lower activation energy for conduction.

## 1.2 Motivation

To further reduce the operational temperatures of fuel cells a new kind of fuel cells have been proposed, proton conducting fuel cells (PCFC), having solid oxide electrolytes that instead of conducting oxygen ions conduct the much smaller $H^+$. Exploiting proton conductors can be beneficial for reducing the ohmic resistance, but on the same time the anode and cathode reactions are drastically changed. In an oxygen conducting fuel cell the water is created on the fuel electrode (anode) as shown in **Figure 2.1**, while proton conducting fuel cell form water on the air electrode (cathode), **Figure 2.2** and Equation (1.1). Water formation on the air electrode is advantageous since unreacted fuel can be sent back into the cell without first removing water, but the cathode needs to be designed to work optimal in this new environment. The reduction reaction is more complex with two new species ($H^+$ and $H_2O$) and this limits the reaction to sites where protons, oxygen ions, electrons, oxygen gas and humidity can coexist. This is usually the area called triple phase boundary where electrolyte, cathode and porosity meets. To increase the number

of sites for reaction it is advantageous to have a cathode with good conductivity of protons, oxygen ions and of course electricity.

$$\frac{1}{2}O_2 + 2e^- + 2H^+ \longrightarrow H_2O \tag{1.1}$$

$$\frac{1}{2}O_2 + 2e^- \longrightarrow O^{2-} \tag{1.2}$$

Many perovskites and the related layered double perovskite (LDP), have been investigated to see if they work well as cathode material. LDPs are reported to work better than their single perovskites counterparts because of their inherent oxygen deficient layers creating channels promoting oxygen conduction. The general formula for layered double perovskites is $LnBaM_2O_{5+\delta}$, where Ln is a lanthanide or the similar but smaller yttrium, Ba is barium which is chosen because of its beneficial effect on proton conductivity and M is a transition metal typically Co, Mn or Fe.

## 1.3 Aim of the work

Cathode materials with good oxygen and electronic conductivity exists, but achieving good proton conductivity in cathode environment still remains a challenge. The aim of the work has been to synthesise and characterise the layered double perovskite $YBaCo_2O_{5+\delta}$ to hopefully find a material with good conductivity of protons, oxygen ions and electrons.

After obtaining the phase-pure material by solid state synthesis, properties relevant for application as cathode material was to be investigated. First to be investigated was high temperature structure and oxygen content in a range of $p_{O_2}$ and prove the stability of the cathode material. If the stability was good conductivity and electrochemical performance was to be tested, both dry and after hydration (to see if protonic conductivity enhanced performance). If, however, the stability turned out to be poor, the natural next aim would be to document the decomposition reaction.

If all the properties seemed good, the material could work excellent as a cathode, allowing production of fuel cells with intermediate operating temperature. Having an intermediate operating temperature would further imply lower cost of SOFC enabling widespread use in the energy market.

# Chapter 2

# Theory and background

In this chapter the solid oxide fuel cell is presented in more detail with requirements for optimal performance is stated. The perovskite structure (Section 2.2) and defect chemistry (Section 2.3), with the focus on conductivity, are presented as a background to explain the structure (Section 2.4) and properties (Section 2.5) of layered double perovskites (LDPs).

## 2.1 Solid oxide fuel cell

Solid oxide fuel cells (SOFCs) are all ceramic electrochemically conversion units, efficiently converting chemical energy directly to electrical energy. Fuel cells consist of an anode, an electrolyte and a cathode. On the anode, fuel is oxidised and on the cathode, oxygen is reduced. Electrons are conducted from anode to cathode through an outer circuit performing work. Charge neutrality and the two half-cell reactions are fulfilled by ions conducted through the electrode, either by oxygen ions, which is commonly used and shown in **Figure 2.1**, or protons, **Figure 2.2**, in a Proton conducting/ceramic fuel cell (PCFC).

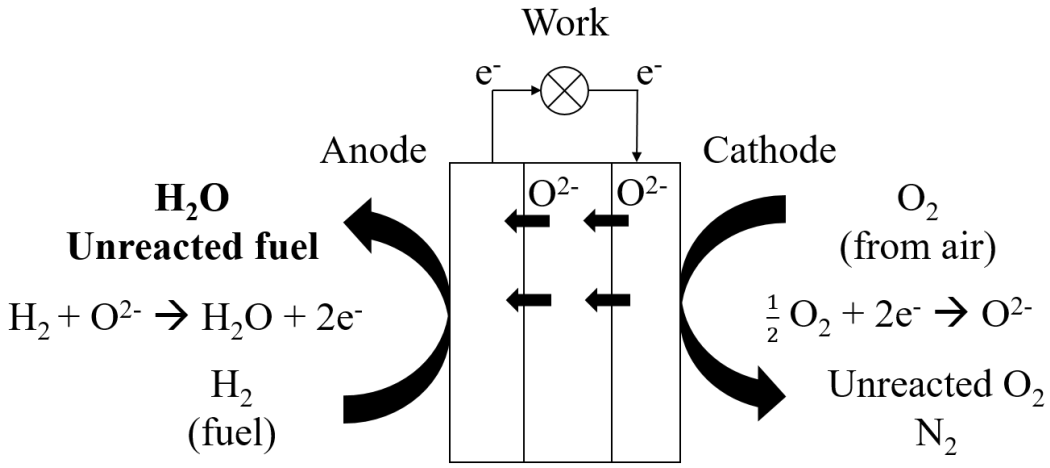


**Figure 2.1:** Schematic of an oxygen conducting solid oxide fuel cell.

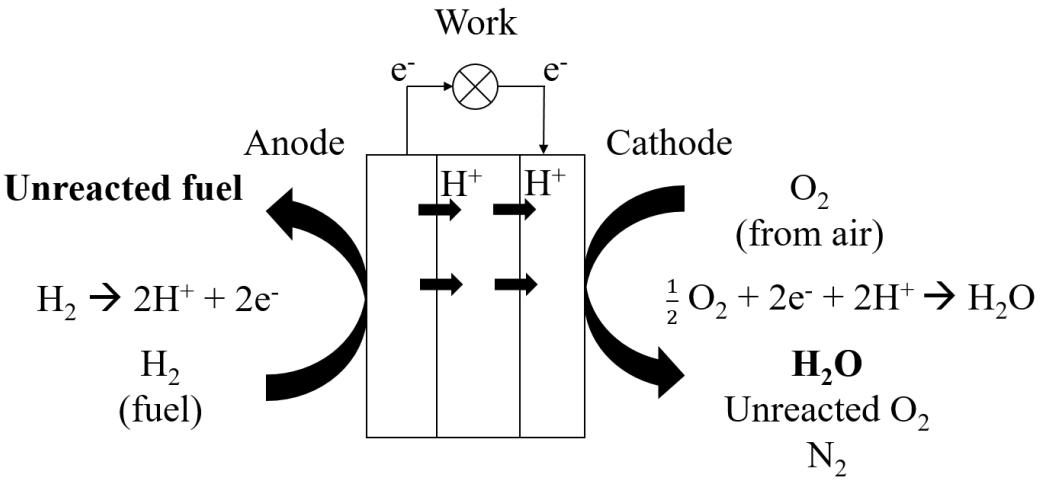


**Figure 2.2:** Schematic of a proton conducting solid oxide fuel cell.

### 2.1.1 Requirements

For an SOFC to function properly several requirements need to be fulfilled. The anode and cathode should be porous to allow flow of fuel and air, respectively, while the electrolyte needs to be dense to avoid crossover of fuel and air since this would reduce the efficiency of the cell. The electrolyte needs to have low ohmic resistance, which is obtained by having a high ionic conductivity. A dense electrolyte is also beneficial since this increases the area of the conductor, thus reducing the ohmic resistance. The electrolyte should be an electronic insulator to avoid short-cutting the cell, whereas the electrodes should be electrical conductors. Electrical conductivity of 100 S/cm is often stated to be a minimum for the electrodes.[19,20]

The overpotential[a] for oxygen reduction reaction (ORR) is high, leading to the requirement of good catalytic activity on the cathode. Having a large area to sustain the reaction reduces the current density and thus the overpotential. In conventional SOFC the reaction is limited to the area where electrolyte, cathode and porosity are in contact, called the triple phase boundary (TPB). This means that to fulfil the reduction of oxygen, as shown in **Equation (1.2)**, the three following components are needed: a material which is conducting oxygen ions (electrolyte), a material which is conducting electrons (cathode), and oxygen from the atmosphere. To enlarge the reaction area electrodes need to be made from mixed ionic-electronic conductors (MIEC), to have a fine structure, or to have a composite electrode constituted of the electrode and electrolyte materials.

Further it is important that the cathode material is cheap, abundant, chemically stable in a range of partial pressure of oxygen as well as chemical compatible with the electrolyte and interconnects. The material should have a similar thermal expansion as the rest of the cell to reduce degradation from thermal mismatch.

[a] Overpotential is a measure of the extra force needed to make a reaction occur, the deviation from reversibility.

### 2.1.2 Conventional SOFC

Oxygen conducting SOFC is a mature technology developed in the 1990s,[20] nevertheless it is not heavily implemented in the market due to high cost and short lifetime. The cell is operated at high temperatures, 800 - 1000 °C, to assure high oxygen conductivity in the electrolyte, and high catalytic activity at the cathode.[16,21]

The electrolyte is usually made of yttria-stabilised zirconia (YSZ), which is an excellent oxygen conductor at 1000 °C with a ionic conductivity of 0.1 S/cm.[20] The anode material is usually a mixture of the electrolyte material and nickel, while the cathode is made of lanthanum strontium manganite (LSM).[20] The mixture of YSZ and nickel creates increased TPB and gives an increased area for oxidation of fuel. LSM has a good catalytic activity with polarisation resistance less than $1\,\Omega\,cm^2$ at 1000°C, but if the temperature is reduced to 500 °C the polarisation resistance increase to $2000\,\Omega\,cm^2$, far more than practical applicable.[20]

The high temperature is advantageous since relatively cheap oxides can be used as cathode instead of expensive platinum group materials. Another advantage is that the cell can internally reform fuels, thus avoiding external reformers that increase complexity and decrease output. However, the high temperature causes problem with long start up times, material degradation and short lifetime. Short lifetime makes SOFC expensive, since they need to be replaced after a few years of operation. To give an impression of the lifetime of fuel cells; the world record for longest running solid oxide fuel cell was held by Siemens Westinghouse with operation for 69 000 h (almost 8 years), until October 2015 when Scientist from Jülich Research Centre got the record with operation for more than 70 000 h.[22–24]

### 2.1.3 Approaches to reduce operational temperature

If SOFC were operated at lower temperatures significant cost savings would be possible by using less expensive materials for interconnect and heat exchangers.[20] Other technologies are therefore needed to reduce the operational temperature of SOFC, both for electrolyte and electrodes, in particular the cathode. This is because the kinetics of oxygen reduction is slower than reduction of hydrogen.

Many groups of materials have been investigated to find promising cathode materials, as well as known materials have been engineered to give better performance. The area where the ORR can occur is often optimised by having a fine microstructure creating more TPB. A common strategy to further increase the reaction area is to make a composite cathode, similar to the cermet on the anode side. One oxide conduct electrons, while another conduct oxygen, e.g. LSM and YSZ.[15] Though the amount of catalyst is less, the active catalytic area can be increased because the TPB is increased. Instead of having separate oxygen and electronic conducting materials, materials conducting both electrons and oxygen the same material have been developed. These materials are called mixed ionic-electronic conductors (MIECs). **Figure 2.3** is a schematic to compare **(a)** an only electrical conducting cathode and **(b)** an MIEC cathode used with an oxygen conducting electrolyte. The green area indicate the electrochemically active area, which is only the TPB in **(a)**,

while **(b)** can exploit the whole cathode-porosity interface. The increase of TPB with a cathode mixture of electrolyte and electronic conductor can be seen in **(c)**.

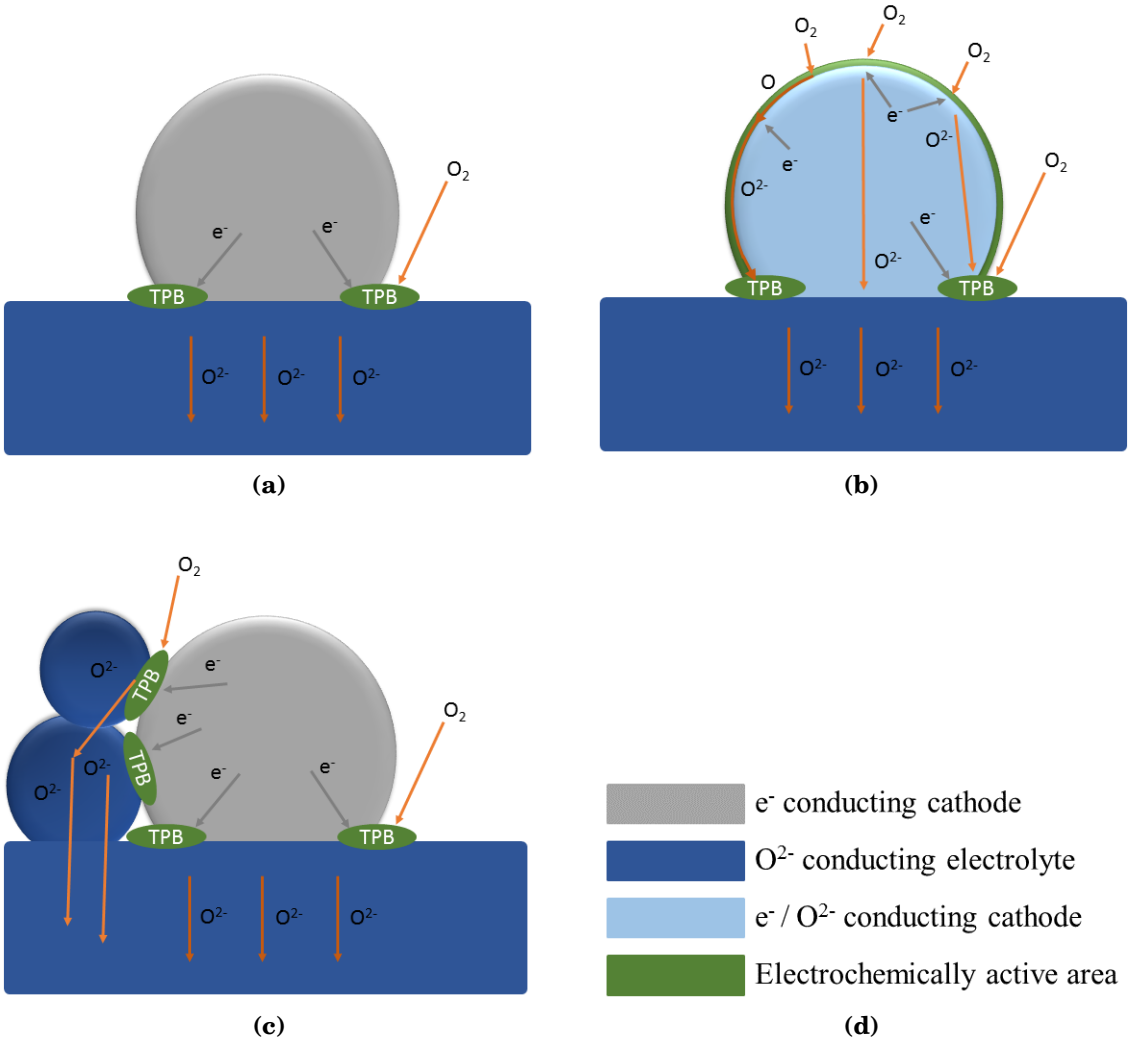


**Figure 2.3:** Schematic of oxygen conducting electrolyte with:
**(a)** pure electronic conducting cathode (grey),
**(b)** mixed ionic-electronic conducting cathode (blue) and
**(c)** composite cathode made of electronic conducting cathode material mixed with electrolyte (grey/dark blue).
Green area indicate the electrochemically active area.

Several material systems exhibiting MIEC properties have been investigated including perovskites ($ABO_3$), A-site ordered layered perovskite ($LnBaCo_2O_{5+\delta}$), Ruddlesden-Popper intergrowth oxides and hexagonal ($RBa(Co_{1-y}Zn_y)_4O_7$ (R = rare earth or alkaline earth)) oxides,[5] as well as fluorites $AO_2$.[25] Perovskites are the most investigated. Today MIEC materials are a developed technology allowing fuel cell to operate in the temperature range 600 - 800 °C. Two of the best cathode materials are LSCF and BSCF, which both are perovskite materials. Layered double perovskite has also proved to be good MIEC materials.

Regarding the electrolyte two methods have been employed to reduce the operating temperature. One aim has been to reduce the electrolyte resistance by reducing the

thickness. This has been employed in microcells, but for large scale it is difficult to control that the extremely thin electrolyte is gas tight, and if it is not gas tight cell efficiency deteriorates. At small dimensions, (e.g. 10 µm) reducing thickness further does not yield better performance since surface exchange kinetics become rate determining step and not the bulk diffusion. The other approach to reduce the operational temperature is to find materials with higher conductivity at lower temperatures. YSZ[b], LSGM[c] and CGO[d] are three systems that have been thoroughly investigated. Assuming a minimum thickness of 10 µm and conductivity of 0.01 S/cm their minimum operational temperatures are about 700 °C (YSZ) and 550 °C (LSGM and CGO).[20]

LSGM and CGO can be used at intermediate temperature, 600 - 800 °C, but for reducing operational temperature of the electrolyte below 600 °C it has been proposed to use proton conductors instead of oxygen ionic conductors. Hydrogen is a smaller atom than oxygen, and it has a lower activation energy for jumping giving it a higher mobility than oxygen ions. PCFC can potentially work between 300 and 600 °C, significantly reducing the operational temperature.[26] Iwahara et al.[27] investigated doped strontium cerates ($SrCeO_3$) and doped barium cerates ($BaCeO_3$) and found that when used as fuel cell electrolyte water was formed at the cathode, which indicatea that the electrolyte was proton conducting. They also found that water could be formed at both sides indicating that both proton and oxygen conduction was present. Fuel cells based on barium cerate gave much higher power than those based on strontium cerate.[27] Two state-of-the-art proton conductors today are BZY[e] and BCZY[f]. Proton conductivity of these materials are $1 - 2$ orders of magnitude greater than oxygen conducting electrolytes like YSZ and LSGM.[10]

The switch to a a proton conducting electrolyte complicates the reduction reaction since both protons and water is incorporated. Using a MIEC cathode with oxygen conducting electrolyte expand the electrochemically active region, while if a MIEC cathode is used with proton conducting electrolyte the active region is still limited to the TPB, **Figure 2.4 (b)**.[28] Notwithstanding this, the performance can be increased since the oxygen reduction can occur on a larger area and oxygen ions can be transported to the triple phase boundary. If a mixture of MIEC and proton conductor is used as cathode, the TPB can be increased, Figure 2.4 **(c)**. Using a mixed protonic-electronic conductor as cathode, **Figure 2.4 (d)**, or a triple-conducting cathode, Figure 2.4 **(e)** the electrochemically active area increase to the whole cathode-porosity interface.

Changing from oxygen to proton conducting electrolyte impose new requirements for the cathode to work optimally. It would be advantageous with either mixed protonic-electronic conductors or triple-conducting materials, but none have been reported to be both stable in cathodic environment and have sufficient conductivity.[9,29] Research have been done on making proton electrolyte materials also electrical conducting by appropriate doping (to overcome the percolation threshold) for the use of cathodes, unfortunately the conductivities found are rather small and not

[b] Zirconia doped with Yttrium Oxide
[c] Lanthanum Gallate doped with Strontium Oxide and Magnesium Oxide
[d] Ceria doped with Gadolinium Oxide
[e] Yttria-doped barium zirconate
[f] Zirconia- and yttria- doped barium cerate

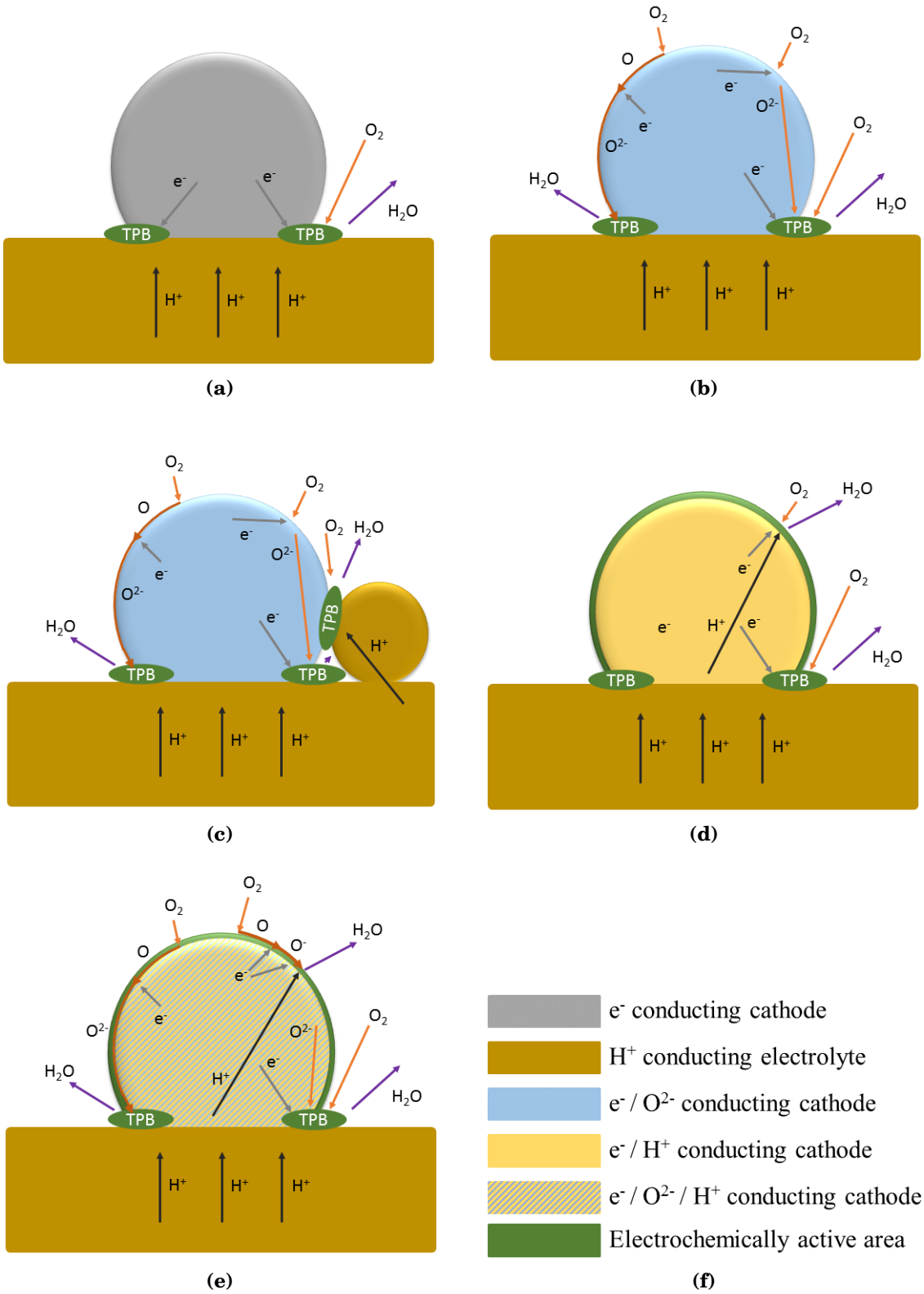


**Figure 2.4:** Schematic of proton conducting electrolyte with:
**(a)** a pure electronic conducting cathode (grey),
**(b)** a mixed ionic-electronic conducting cathode (blue),
**(c)** a mixed ionic-electronic conducting cathode mixed with electrolyte (blue/dark yellow),
**(d)** a mixed protonic-electronic conducting cathode (yellow) and
**(e)** a triple-conducting cathode (blue and yellow).
Green area indicates the electrochemically active area.

sufficient for use as single phase cathode.[9,30]

The elementary cathode reaction steps in a triple-conducting cathode are summarised in Table 2.1. In a MIEC cathode only reaction step 1 - 5 is present. Yang et al. found that $SmBaCo_2O_{5+\delta}$ is a good cathode material for conventional SOFC, while it did not perform well in a PCFC.[28] This might be due to the limited area for the reaction with a MIEC on a proton conducting electrolyte.

**Table 2.1:** Elementary cathode reaction steps for a proton/oxygen-ion/electron conducting cathode working in a protonic SOFC.[9]

| Elementary reaction steps | | |
|---|---|---|
| (1) | $O_{2(g)} \longrightarrow O_{2(ad)}$ | (oxygen adsorption) |
| (2) | $O_{2(ad)} \longrightarrow 2O_{(ad)}$ | (oxygen dissociation) |
| (3) | $O_{(ad)} + e^- \longrightarrow O^-_{(ad)}$ ; $O_{(ad)} + 2\,e^- \longrightarrow O^{2-}_{(ad)}$ | (oxygen reduction) |
| (4) | $O_{(ad)} \longrightarrow O_{(TPB)}$ ; $O^-_{(ad)} \longrightarrow O^-_{(TPB)}$ | (surface diffusion) |
| (5) | $O^-_{(bulk)} \longrightarrow O^-_{(TPB)}$ | (bulk diffusion) |
| (6) | $2\,H^+_{bulk} \longrightarrow 2\,H^+_{TPB}$ | (proton migration) |
| (7) | $H^+_{TPB} + O^{2-}_{TPB} \longrightarrow OH^-_{TPB}$ ; $H^+_{TPB} + OH^-_{TPB} \longrightarrow H_2O_{TPB}$ | (water formation) |
| (8) | $H_2O_{TPB} \longrightarrow H_2O_g$ | (water evaporation) |

Triple-conducting materials are quite new field, and only a few compounds have been reported to possess proton conductivity in addition to being MIEC.[29,31] Grimaud et al. investigated $PrBaCo_2O_{5+\delta}$, BSCF and $PrNi_2O_{4+\delta}$ and found that they perform better with increasing partial pressure of water, $p_{H_2O}$. The explanation for this is that water is inserted to the structure creating proton conductivity.[29] Layered double perovskites are known to be good MIEC materials, and perhaps can they prove to possess fair proton conductivity as well.

### 2.1.4 Proton conducting solid oxide fuel cell

Going from an oxygen conducting to a proton conducting solid oxide fuel cell have several implications. In a conventional SOFC both hydrogen and carbon monoxide can be electrochemically oxidised, while in a PCFC oxygen ions are not present and only oxidation of hydrogen is possible.[18,32] However, dehydrogenation, Equation (2.1), is possible, and if water is present fuel can be internally reformed.

$$2CH_4 \longrightarrow C_2H_4 + 2H_2 \tag{2.1}$$

The production of ethylene ($C_2H_2$) and other high-molecular hydrocarbons can be seen as an advantage since ethylene production usually demands energy and ethylene and other high-molecular hydrocarbons are needed in chemical industry.[32,33]

## 2.2 Structure of perovskite

The class of materials with chemical formula $LnBaM_2O_{5+\delta}$ are called layered double perovskites (LDP), their structure is related to the simpler single perovskite. The single perovskite structure consists of two cations, a larger metal ion A, a smaller metal ion B, and an anion, typically oxygen. The structure of generic simple perovskite is shown in **Figure 2.5**. A-ions (green) prefer to be 12 coordinated (number of nearest neighbouring oxygen), while B-ions are smaller and prefer to be 6 coordinated (blue, located within light blue octahedron). The perovskite structure can combine a wide range of elements, and this makes it an interesting structure for a wide range of applications. If the atomic radii of the elements do not fit with the ideal perovskite structure distortions (e.g. tilting of octahedrons) can occur to compensate.

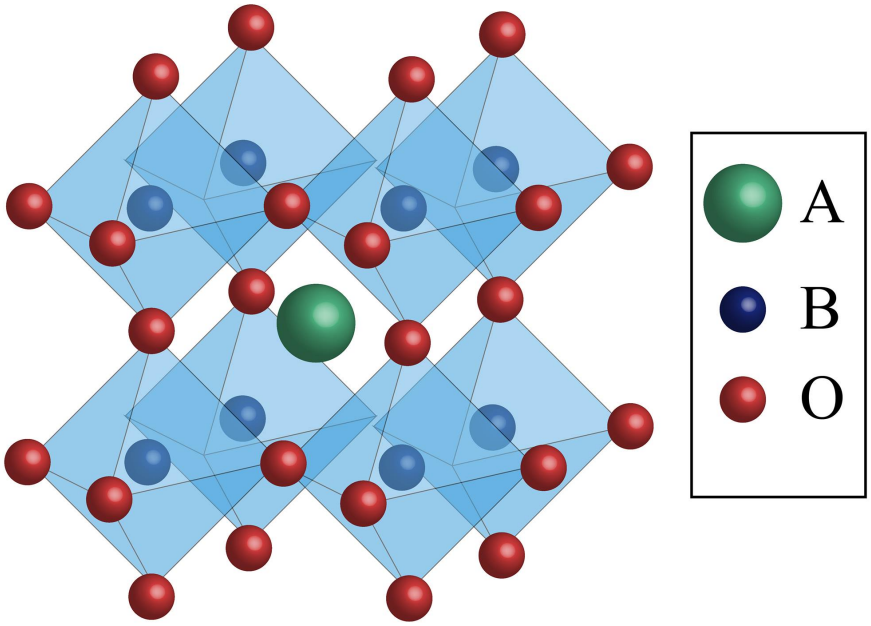


**Figure 2.5:** Structure of generic perovskite, $ABO_3$

For an ideal perovskite structure: $r_A+r_O = \sqrt{2}\,(r_B+r_O)$, where $r_A$, $r_B$ and $r_O$ is the ionic radii of the large A-atom, the smal B-atom and the anion . Deviations from this can be described by the Goldschmit tolerance factor, $t$, Equation (2.2).[34] The tolerance factor is based upon simple geometric considerations and can be used to predict the structure. t = 1 describes an ideal perovskite structure. Values of $t$ below unity down to 0.75 is found to be distorted perovskite and if t>1 the structure will usually be hexagonal. If $t$ is lower than unity the symmetry is reduced from cubic to tetragonal, rhombohedral, orthorhombic etc.[34]

$$t = \frac{r_A + r_O}{\sqrt{2}(r_B + r_O)} \tag{2.2}$$

## 2.3 Defect chemistry

Defects might sound negative, but their existence is of fundamental importance especially due to their ability to reduce the energy necessary to create changes i.e. the activation energy. Instead of moving a row of atoms simultaneously defects allow simply moving one at the time. In this section the standard notation for defect chemisty is first introduced before it is used to explain charge compensation and how conductivity is dependent upon suitable defects.

### 2.3.1 Kröger-Vink notation

Kröger-Vink notation is a simplified syntax to write chemical equations with point defects. A chemical equation in Kröger-Vink notation both contain the species involved, relative charge and their position. The syntax is:

$$\mathrm{Specie}^{\text{Relative charge}}_{\text{Lattice position}}$$

The specie can either be an atom or a vacancy, (V). Instead of using absolute charge of an element the relative charge compared to the lattice position is given, either as positive ($^{\bullet}$), neutral ($^{\times}$) or negative ($^{\prime}$). With Kröger-Vink notation mass, relative charge, number of ions and sum of oxidation numbers should balance. As an example, inserting a divalent barium atom at the postion of a tetravalent yttrium atom would yield:

$$2\,\mathrm{Y}_{\mathrm{Y}}^{\times} + 2\,\mathrm{BaO} + \mathrm{O}_{\mathrm{O}}^{\times} \longrightarrow 2\,\mathrm{Ba}_{\mathrm{Y}}^{\prime} + \mathrm{Y_2O_3} + \mathrm{v}_{\mathrm{O}}^{\bullet\bullet}$$

Where $\mathrm{Y}_{\mathrm{Y}}^{\times}$ and $\mathrm{O}_{\mathrm{O}}^{\times}$ indicate an yttrium atom at the lattice position of yttrium and oxygen at position of oxygen, respectively. $\mathrm{Ba}_{\mathrm{Y}}^{\prime}$ indicates barium at yttrium position with a negative charge, and $\mathrm{v}_{\mathrm{O}}^{\bullet\bullet}$ oxygen vacancy with a relative charge of +2. BaO is a dopant and not a part of the structure and it is therefore not given any lattice position.

### 2.3.2 Conductivity and charge compensation

Conductivity is a measure of how easily a material can conduct current, either electrical or ionic. The conductivity of a material is the sum of the conductivity of its constituents, and the conductivity of the constituents is given by the product of the mobility of the charge carrier, the charge and the number of charge carriers, as given in Equation (2.3). The greatest conductivity is usually found with a tradeoff between number of charge carriers and their mobility. In most cases, where both ionic conductivity ($\sigma_i$) and electronic conductivitiy ($\sigma_e$) are present, the electronical conductivity is several orders larger ($\sigma_i \ll \sigma_e$).

$$\sigma = \sum_j \mu_j n_j q_j \tag{2.3}$$

In solids defects are needed to allow conduction. For electrical conductivity the charge carriers are either electrons (excess of electrons) or holes (deficiency of elec-

trons). Ionic conduction needs ionic defects, either as interstitials or vacancies. The perovskite structure has little or no room for interstitial oxygen, so creating vacancies is usually done to promote oxygen conductivity.

Charge carriers can be created by doping the A site of the perovskite structure with a lower valent atom A'. The structure needs to compensate for this change to obtain charge neutrality. The material can compensate in two ways, either by an electronic compensation mechanism, increasing the B-cation charge according to (2.4), or by ionic compensation mechanism, creating oxygen vacancies according to Equation (2.5). Often is both compensation mechanisms present, electronic dominating at high $p_{O_2}$ and low temperatures, while ionic is favoured at low $p_{O_2}$ and high temperatures.[5] At high $p_{O_2}$ the structure can even incorporate excess oxygen by oxidation of B either with interstitial oxygen or by creating cation vacancies.

$$ABO_3 \xrightarrow{xA'} A_{1-x}A'_xB^{n+}_{1-y}B^{(n+1)+}_y O_3 \tag{2.4}$$

$$ABO_3 \xrightarrow{xA'} A_{1-x}A'_xB^{n+}O_{3-\frac{x}{2}} \tag{2.5}$$

Depending on which elements A, A' and B represents, as well as partial pressure of oxygen ($p_{O_2}$) and temperature, the dominating compensation mechanism will vary.[5] State of the art cathode material for conventional SOFC is LSM (A = $La^{3+}$, A' = $^{2+}$, B = $Mn^{3+}$). This compound can only have oxygen deficiency at very low $p_{O_2}$ and electronic compensation is dominating[35] making it a poor ionic conductor. A wide range of materials have been investigated for MIEC propetries, and among them the layered double perovskites are promising.

To achieve proton conductivity protonic defects are needed. The perovskite structure generally does not contain protons, but protons can be incorporated into the structure. Protons do not occupy interstitial positions, but bond with oxygen forming hydroxide. Incorporation of protons can occur without vacancies according to Equation (2.6) in dry atmosphere. However hydration of oxides, Equation (2.7), where oxygen vacancies ($v_O^{\bullet\bullet}$) and lattice oxygen ($O_O^{\times}$) adsorb water to form hydroxide ($OH_O^{\bullet}$) is dominating. This occurs especially at lower temperatures because water absorption is an exothermic reaction.

$$H_2(g) + 2\,O_O^{\times} \longleftrightarrow 2\,OH_O^{\bullet} + 2\,e' \tag{2.6}$$

$$v_O^{\bullet\bullet} + H_2O(g) + O_O^{\times} \xleftrightarrow{K} 2\,OH_O^{\bullet} \tag{2.7}$$

To achieve high proton conductivity the material should be tailored to give suitable amount of oxygen vacancies and a high equilibrium constant. The concentration of oxygen vacancies is conventionally controlled by the amount of substitution, or, in the case of layered double perovskites, by the size of the lanthanide. The degree of hydration depends on the atoms present. The equilibrium constant, K, is larger when A-site atom is Ba compared to Sr, and for B-site atom Ce followed by Zr, Nb, Ti.[32,36] Thus proton conduction in LDP with barium is supposed to be greater than

with strontium. The amount of $OH^{\bullet}$ formed is double compared to initial oxygen vacancy content, according to Equation (2.7), but this has been found to only be possible to achieve if tolerance factor is close to unity.[32,36]

Protons are conducted in perovskites through hopping of protons from one oxygen to another, rotation around oxygen before a new jump. This process is called Grotthuss-type mechanism,[1,32,37] opposed to vehicle transportation were protons are fixed to a moving oxygen.[1] A schematic of Grutthuss-type mechanism is given in **Figure 2.6**.

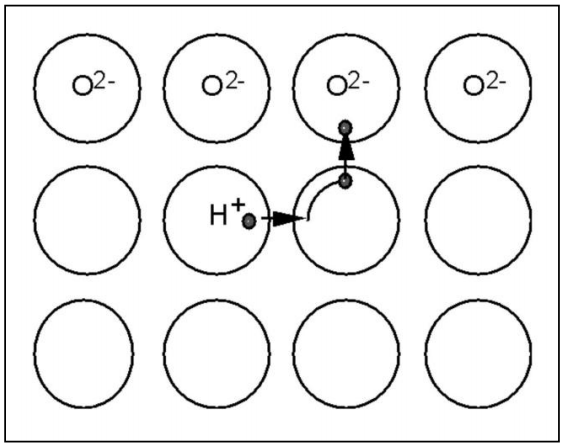


**Figure 2.6:** Schematic illustration of Grotthuss-type mechanism in oxides. Taken from Pan.[1]

## 2.4 Layered double perovskite

### 2.4.1 Structure

In perovskites doping can be performed either on the A-site, B-site or both. The compounds with formula $Ln_{0.5}Ba_{0.5}MO_{3-\delta}$ can be looked at as $LnMO_3$ where the A-site is half substituted by $Ba^{2+}$ for $Ln^{3+}$.The lanthanide, Ln, and Ba atoms are randomly distributed and the structure remain cubic, **Figure 2.7 (a)**. For most compounds the difference in size between Ln and Ba is large and the cation order into alternating layers of $LnMO_{3-\delta}$ and $BaMO_3$, the formula is then written as $LnBaM_2O_{5+\delta}$ to emphasise that the structure is ordered. If the difference in size is small between Ln and Ba (i.e. Ln = La) the cubic disordered structure is favoured. However, the ordered structure is also possible to obtain by carefully tailored annealing.[38]

The acceptor doping of $LnMO_3$ by barium needs to be compensated, and this is done either through the ionic compensation mechanism by creating oxygen vacancies or by electronic compensation increasing the valence of M. The amount of oxygen is written as 3-$\delta$ in the disordered case and by convention 5+$\delta$ for ordered case to emphasise the large oxygen deficiency. Some do use 6-$\delta$ in the ordered case. To avoid confusion the oxygen content for layered double perovskite will be referred to as 5+$\delta$, not just $\delta$, throughout this thesis.

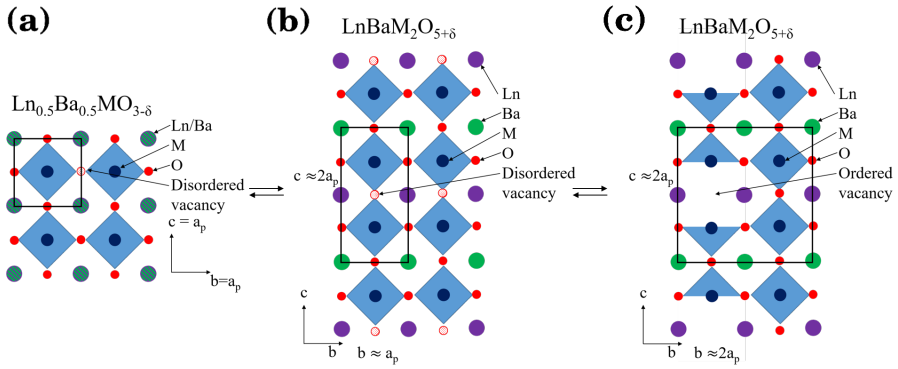


**Figure 2.7:** **(a)** Structure of A-site disordered and vacancy disordered $Ln_{0.5}Ba_{0.5}MO_{3-\delta}$, **(b)** Structure of A-site ordered and vacancy disordered $LnBaM_2O_{5+\delta}$, **(c)** Structure of A-site ordered and vacancy ordered $LnBaM_2O_{5+\delta}$.

Several possibilities exist for ordering of ions in the perovskite structure, either as rock salt, columns or layers.[39] In the group of materials with chemical formula $LnBaM_2O_{5+\delta}$ they all form alternating layers of Ln and Ba. This helps to reduce tension since Ln and Ba can have considerable difference in ionic size.[39] In between the Ln and Ba layers are the B-positions occupied by a transition metal (M). The vacancies are situated within the lanthanide layer, either randomly distributed as in **Figure 2.7 (b)**, or ordered, as in **Figure 2.7 (c)**. The Ln-ion is smaller than Ba-ion, and this cause the vacancies to favour the Ln-layer. This cause the coordination number of Ba to remain at 12, while the Ln coordination number can be reduced.[5] The structure form a stacking sequence $[CoO_2]$-$[LnO_\delta]$-$[CoO_2]$-[BaO] along the c-axis.[3,40–45]

### 2.4.2 Superstructure

In the literature several superstructures are given for the $LnBaM_2O_{5+\delta}$ compounds. If they are A-site ordered, as implicated by the formula (compared to $Ln_{0.5}Ba_{0.5}MO_{3-\delta}$), they have a doubling of the c-parameter compared to single perovskite. How the a and b lattice parameters increase by ordering are not so straight forward .

The oxygen ordering can be as shown in **Figure 2.7 (c)**, with a doubling in a- or b-lattice parameter, compared to the cubic perovskite lattice parameter $a_p$. This is called a 122-phase (or 212-phase) since the unit cell is doubled in b- and c-direction (or a- and c-direction). Oxygen ordering can also lead to other structures such as 332-phases with a tripling of the a and b parameter, doubling of all three lattice parameters or even larger unit cells e.g. factor of $3\sqrt{2}$.[4]

The superstructures are dependent upon the oxygen stoichiometry as well as the size of cations. To obtain a 122 superstructure the oxygen content needs to be relative close to 5.5 to allow half of the sites to be unoccupied forming pyramidal oxygen coordination and the other half occupied forming octahedral occupation.[41] A lot of literature exists about the LDPs, ecspecially for sub zero temperatures with the aim of finding interesting magnetic and electronic properties.[3,46–49] In the later years more papers have also started to include high temperature data with the aim of finding materials for solid oxide fuel cells.[10,45,50]

While the 122 structure is observed for a wide range of lanthanides (Pr-Ho) and Y, the 222 structure is reported for only large lanthanides (Pr-Gd).[51] The 332 structure has been reported for Dy and Ho, which are small lanthanides and yttrium. Aksenova et al. could only find superstructure for Y, and stated that Dy and Ho had 112 structure.[52] Maignan et al., however, stated that Ho and Dy show 332 superstructure.[3] The 332 structure has further been reported for Y by Zhou,[2] Akahoshi and Yueda,[53] Urusova et al.[54] and McKinlay et al.[4]

X-ray diffraction form factor scales with atomic number, whereas neutron scattering lengths do not show the same dependence. This makes neutron diffraction superior to investigate lighter elements such as oxygen.[37] The superstructures formed due to oxygen ordering is often not visible with XRD, and they require electron microscopy investigations.[55] The superstructures are usually verified by electron diffraction patterns.[4,54,55] Zhou reported the 332 structure for $YBaCo_2O_{5+\delta}$ evidenced by selected area electron diffraction (SAED), but after only one second of electron radiation the superstructure vanished and the pattern resembled the 112 structure, **Figure 2.8 a**.[2]

Superstructures are of great importance for magnetic properties.[55] However, for application as fuel cell cathodes the superstructures are not that important, and at best the vacancies are disordered to give the highest possible ionic conductivity.

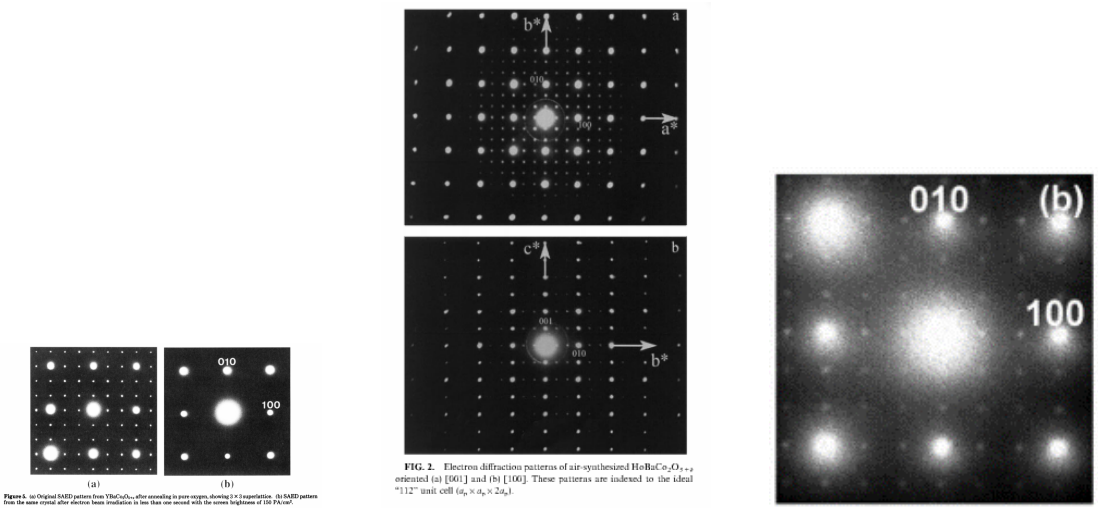


**(a)** **(b)** **(c)**

**Figure 2.8: (a)** Diffraction pattern of $YBaCo_2O_{5+\delta}$ from Zhou.[2] Left: Diffraction pattern shows a 3x3 superstructure. Right: The superstructure has disappeared. **(b)** Diffraction pattern of $HoBaCo_2O_{5+\delta}$ from Maignan et al.[3] Upper: ab-plane with tripling of a- and b-parameter. Lower: bc-plane with tripling of b and doubling of c. **(c)** Diffraction pattern of $YBaCo_2O_{5+\delta}$ from McKinlay et al. showing tripling of a and b.[4]

## 2.5 Layered double perovskite properties

The effect of varying the lanthanide upon oxygen stoichiometry, electrical conductivity, ionic conductivity, electrochemical activity, thermal expansion and stability

is reviewed in this section. Among the LDPs with different transition metals the cobaltites are the most researched since cobalt containing perovskites have high mixed electronic-ionic conductivity and exceptional electrochemical activity.[20] Because of their good properties cobaltites are used as reference material, and doping or total substitution of transition metal is compared to cobalt throughout this section.

### 2.5.1 Oxygen stoichiometry

The oxygen stoichiometry is important for cathode materials to work both for oxygen and proton conductors. Without oxygen vacancies neither can be conducted. It also effects the electrical conductivity. The oxygen content decreases with increasing temperature and increases with partial pressure of oxygen ($p_{O_2}$), further the elements in the structure influence the oxygen content. The vacancy concentration is reported to increase linearly with the difference in radii between Ba and Ln – the smaller the lanthanide the higher the vacancy concentration.[5,38] For large lanthanides the oxygen content can be fully stoichiometric with $5+\delta = 6$, while smaller lanthanides always possess oxygen vacancies.

The amount of oxygen in single perovskites is adjusted with the degree of doping, similarly the oxygen content can be tuned by doping the transition metal. Doping with a trivalent atom ($Fe^{3+}$) decrease the vacancy concentration in $YBaCo_2O_{5+\delta}$, while the opposite occurs with a divalent atom ($Cu^{2+}$).[54] The oxygen content of undoped $YBaCo_2O_{5+\delta}$ was $5+\delta \leq 5.5$, corresponding to cobalt valency $\leq 3$. Doping with an atom of lower valency than the average M valency increase the vacancy concentration while doping with a higher valency atom decrease vacancy content.

The compensation mechanism is also effected by the transition metal. The binding energy between M and O increase from Co to Fe to Mn, making ionic charge compensation least favoured for M = Mn compounds. It is well known that LSM's[g] oxygen deficiency is very limited making it a pure electronic conductor, while LSC[h] is a MIEC.[56,57] Looking at one of the few Mn compounds reported $NdBaMn_2O_{5+\delta}$ had only oxygen deficiency at reducing conditions,[58] while $NdBaCo_2O_{5+\delta}$ is oxygen deficient.

### 2.5.2 Electrical conductivity

LDPs are p-type conductors having cobalt holes ($Co^{\bullet}_{Co}$) as charge carriers. Earlier it was believed that LDPs had metallic conduction, but it is widely supported that they have small polaron p-type conduction.[10,54] The electrical pathway of LDPs with M = Co is through the overlapping between Co:3d and O:2p orbitals. Below metal-insulator transition (MI) the conductivity increase with increasing temperature, while at higher temperatures oxygen vacancies are created and the amount of cobalt holes are reduces, according to Equation (2.8). For YBCO the MI transition is approximately 200 °C,[6] for larger Ln the transition temperature is decreased.[40]

[g] Strontium doped lanthanum manganite

[h] Strontium doped lanthanum coboltite

The MI transition is stated to originate in the change from low-spin ($t_{2g}^6 e_g^0$) to high-spin ($t_{2g}^5 e_g^1$) of $Co^{3+}$.[5] As the size of Ln increase, the oxygen content and valency of cobalt increase making the transition less pronounced.[5]

$$2\,Co_{Co}^{\bullet} + O_O^{\times} \longrightarrow 2\,Co_{Co}^{\times} + V_O^{\bullet\bullet} + \frac{1}{2}\,O_2(g) \tag{2.8}$$

Another effect which reduces the electronic conductivity is as the Ln size decrease, the Co-O-Co bond is bending. Ideally this angle is 180° giving good overlap of the Co:3d and O:2p orbitals. However, as the structure becomes more distorted, the overlap is reduced, the bandwidth is narrowed and conductivity reduced.[5,10] The bond bending, narrowing of bandwidth and decreased overlap can be seen in **Figure 2.9**.

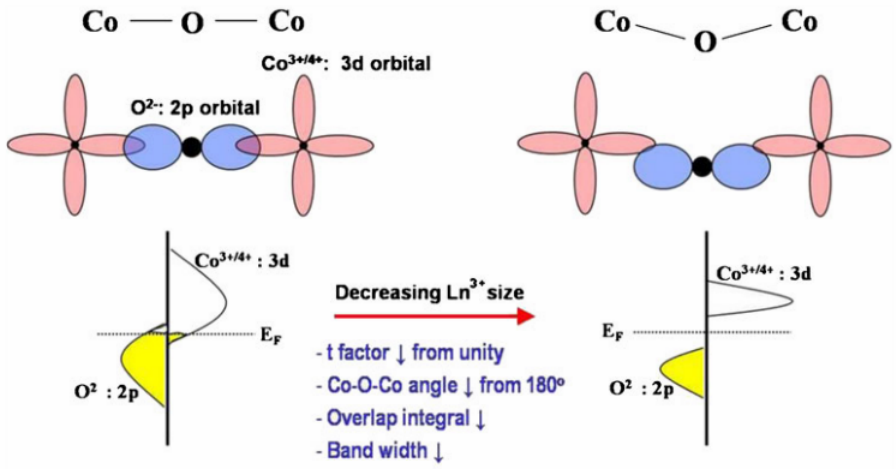


**Figure 2.9:** Effect of lattice strain on bandwidth and orbital overlap between oxygen and cobalt. Taken from Manthiram et al.[5]

The conductivity of cobaltites are superior compared to other 3d metals.[5] Zhang et al. report that the conductivity of $LnBaCo_2O_{5+\delta}$ is high with maximum conductivity above 50 $S\,cm^{-1}$ for all Ln investigated (La, Pr, Nd, Sm, Gd, Y).[59] The highest conductivity was reported for Ln = La with 370 $S\,cm^{-1}$.[59] Kim and Manthiram report significantly higher conductivities, all above 100 $S\,cm^{-1}$ and maximum for Ln = La of 2500 $S\,cm^{-1}$.[10] Looking at at $YBaCo_2O_{5+\delta}$ which should have the lowest conductivity the numbers range from 20–40 $S\,cm^{-1}$,[4] 50–140 $S\,cm^{-1}$,[60] 250–500 $S\,cm^{-1}$,[61] and ~100 $S\,cm^{-1}$.[21] In the project[6] leading up to this thesis the electrical conductivity was measured for a sample with some secondary phases (yttrium and barium cobaltite) and a relative density of 70 %, the conductivity ranged from 100–500 $S\,cm^{-1}$ as shown in **Figure 2.10**. Though the numbers might be incorrect due to secondary phases and porosity (which was corrected for by dividing by relative density) the graph shows how p-type conductor behave with respect to temperature and $p_{O_2}$. The conductivity increases with $p_{O_2}$ and above the MI-transition conductivity decrease with temperature. The values for conductivities stated above are all for temperatures above 300 °C.

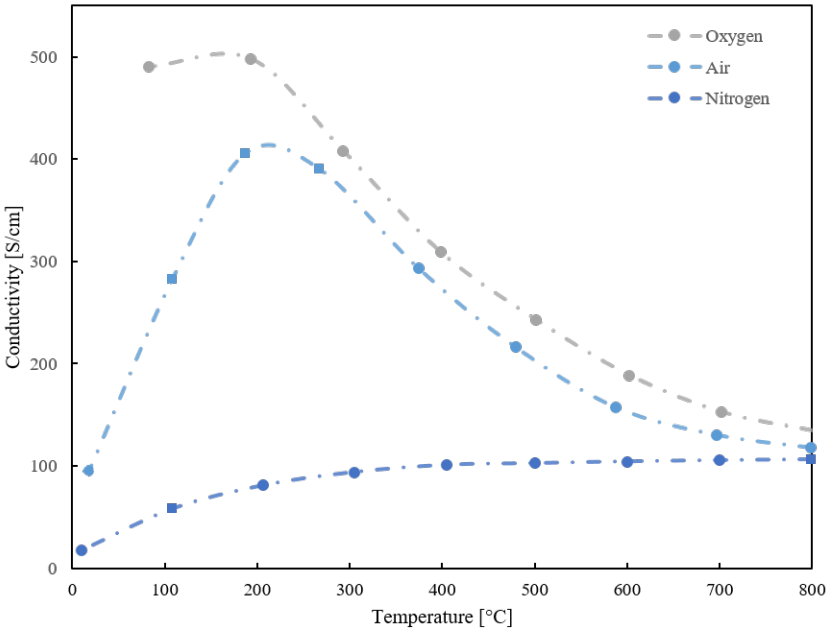


**Figure 2.10:** Total conductivity of $YBaCo_2O_{5+\delta}$ as function of temperature in $O_2$, air and $N_2$, data from project fall 2015.[6]

### Conductivity of $LnBaFe_2O_{5+\delta}$

Chen et al. reported the conductivity of $LnBaFe_2O_{5+\delta}$ for Ln = La, Pr, Nd, Sm, Gd and Y as function of temperature with varying $p_{O_2}$ (Ln = La, Pr being cation disordered). The maximum conductivities in oxygen were 180, 55, 37, 14, 10 and 2 $S cm^{-1}$, respectively. As $p_{O_2}$ decrease the conductivity drops far more than in the case of M = Co.[62]

### Conductivity of $LnBaMn_2O_{5+\delta}$, Ln = Nd

Pineda et al. investigated $NdBaMn_2O_{5+\delta}$ and found conductivity of 0.06 $S cm^{-1}$ for $5+\delta$ = 5, and for 20 $S cm^{-1}$ for $5+\delta$ = 6.[58] Both are far below required conductivity of an electrode. Broux et al. investigated $NdBaCo_2O_{5+\delta}$ both partially and fully subsituted with Mn for Co.[63] They found that the conductivity was >100 $S cm^{-1}$ for $NdBaMn_2O_{5+\delta}$, which is sufficient as cathode, but small compared to >500 $S cm^{-1}$ as for $NdBaCo_2O_{5+\delta}$.[63] This shows that despite large variations in reported values cobaltites have better/superior electrical conductivity.

### Sr doping

If the B-site is doped with the smaller Sr, the size differency between Ln and Ba/Sr is reduced. This increases the bond angle towards 180°, increasing the covalency

and the bandwidth, giving the Sr-doped compounds a higher electrical conductivity than the pristine compound.[4,21]

### 2.5.3 Ionic conductivity

Compared to single perovskite the oxygen conduction is enhanced due to the anisotropy of LDPs, giving lower activation energy for conduction.[64] As Ln decrease, the number of vacancies increase. Having more charge carriers should increase ionic conductivity. Despite this, the trend seems to be the opposite, smaller lanthanides leads to lower ionic conductivity. This is probably because smaller Ln gives more strain, and this deteriorates the mobility.[5,65] Mogensen et al. stated that a critical parameter for ionic conductivity in perovskites is the lattice strain.[25] This is also valid for LDPs. A distorted structure will have varying bonding energies for oxygen, and this increase the activation energy for hopping.[65]

The binding energy for oxygen is larger in M = Mn and Fe compounds than for M = Co, thus the oxygen ionic conductivity is lower.[5] The increased binding energy can be seen from the increasing difference in electronegativity between M and O going from M = Co to Fe to Mn.

### 2.5.4 Thermal expansion

The electrical and ionic conductivity, as well as electrochemical performance, is superior for M = Co. Unfortunately, the thermal expansion coefficient (TEC) is high, giving large mismatch with most electrolytes.[64] The high TEC is related to the ease of cobalt changing oxidation state and spin state.[66] In cobalt the difference between energy of crystal field splitting of d-electrons and the interatomic excange interaction is small, thus $Co^{3+}$ can easily switch between low-spin (LS, $t_{2g}^6e_g^0$), intermediate-spin (LS, $t_{2g}^5e_g^1$) and high-spin (LS, $t_{2g}^4e_g^2$).[47] The layered double perovskites based on cobalt also have high TEC, but it can be tailored by changing the lanthanide. The TEC of $LnBaM_2O_{5+\delta}$ decreases with decrasing size of Ln due to decrease in ionicity of the Ln-O bond, as covalent bonds generally exhibit smaller thermal expansion than ionic bonds.[5,67–69]

Doping with other transitionmetals is commonly used to decrease TEC. Doping to reduce TEC is usually limited by a compromise with reduced conductivity and electrochemical performance. TEC can also be reduced by making composite electrodes of cathode- and electrolyte material.

**Table 2.2** shows TEC value for several electrolytes and cathode materials, ideally these values should be the same for cathode and electrolyte (and anode) to avoid cell degradation during thermal cycling. From the table it can be seen that smaller Ln reduce TEC and that partial or fully substitution of Co for other transition metals reduce TEC.

**Table 2.2:** Thermal expansion coefficient (TEC) of several cathode and electrolyte materials.

| Application | Material | TEC [$10^{-6}\,K^{-1}$] | Reference |
|---|---|---|---|
| P-Electrolyte | BCZY | 10.2 - 12.5 | [70] |
| Cathode | $La_{1-x}Sr_xCoO_{3-\delta}$ | 21.3 | [5] |
| O-Electrolyte | YSZ, GDC, LSGM | 10.0–12.5 | [5] |
| Cathode | $LaBaCo_2O_{5+\delta}$ | 29.3–40.3 | [71] |
| Cathode | $GdBaCo_2O_{5+\delta}$ | 17 | [5] |
| Cathode | $YBaFe_2O_{5+\delta}$ | 14.6 | [67] |

### 2.5.5 Electrochemical performance

The electrochemical performance is reported to decrease as following: Pr > Gd > Nd > Sm > La > Y. The low performance of La and Y was due to instability of the LDP structure.[59] The area specific resistance (ASR) of $PrBaCo_2O_{5+\delta}$ was $0.213\,\Omega\,cm^2$ which approach the best working cathode material BSCF with ASR of $0.1\,\Omega\,cm^2$.[59] Other report $583\,mW\,cm^2$ and $0.51\,\Omega\,cm^2$ at 600 °C for the same cathode material.[72]

The compound $Pr_{1.6}Fe_{0.4}BaCo_2O_{5+\delta}$ with Pr partly substituted by Fe was found to have better properties than the pristine material. The power density and ASR was $446\,mW\,cm^2$ and $0.13\,\Omega\,cm^2$, respectively. The improvement is believed to be related to the change of structure from tetragonal to cubic.[50]

The results mentioned above are for oxygen conducting electrolyte, while reported data on $LnBaM_2O_{5+\delta}$ cathodes with BZCY (10 - 25 µm) proton conducting electrolyte are as follows. At 700 °C $SmBaCo_2O_{5+\delta}$,[73] $GdBaCo_2O_{5+\delta}$[74] and $PrBaCo_2O_{5+\delta}$[75] had respectively power density/ASR of: $382\,mW\,cm^{-2}/0.15\,\Omega\,cm^2$, $266\,mW\,cm^{-2}/0.16\,\Omega\,cm^2$ and $520\,mW\,cm^{-2}/0.06\,\Omega\,cm^2$.[75] The superior results for $PrBaCo_2O_{5+\delta}$ are believed to be due to unusual rapid oxygen ion diffusion rate and surface exchange kinetics,[75] which Kim et al.[76] found to be 2 - 3 orders of magnitude larger than for $GdBaCo_2O_{5+\delta}$.

Doping with yttria to reduce TEC yield $Pr_{1-x}Y_xBaCo_2O_{5+\delta}$ with worse electrochemical properties. The performance was comparable to the level of $GdBaCo_2O_{5+\delta}$, though with higher power density than $GdBaCo_2O_{5+\delta}$.[77]

### 2.5.6 Stability

The last aspect of LDP properties is their stability. The cathode material should be stable in a wide range of partial pressures of oxygen, have no side reactions with $CO_2$ from air and be compatible with the electrolyte.

Zhang et al. state that stability is directly related to the size of $Ln^{3+}$ under reducing conditions. Ln = Pr, Nd, Sm and Gd are stable double perovskite while Ln = La and Y show phase transition.[59,64] Further Zhang et al. also state that $YBaCo_2O_{5+\delta}$ is unstable in oxidising conditions.[59] The instability of $LaBaCo_2O_{5+\delta}$ in reducing conditions is not found reported elsewhere, only the transition from

ordered to disordered, $LaBaCo_2O_{5+\delta} \longrightarrow La_{0.5}Ba_{0.5}MO_{3-\delta}$.[71] However, the instability of $LnBaM_2O_{5+\delta}$ in oxidising conditions with small Ln (e.g. Y, Ho) is described by Kim et al., and stabilisation of the structure by Sr substitution for Ba is shown.[68]

The stability in contact with electrolyte (and interconnects) is also important. In contact with YSZ is $LnBaM_2O_{5+\delta}$ reported to be unstable, while stability in contact with GDC and LSGM depends on Ln.[5] Ln = La and Nd have been found to be stable in contact with GDC and LSGM, while Ln = Gd and Y were unstable. Manthiram et al. state therefore that larger Ln are more stable in contact with GDC and LSGM electrolyte.[5] Kim et al. found similarly instability of Ln = Y and Gd, while Ln = La, Nd and Sd was stable with LSGM.[69] Further the stability is reported to increase by doping Sr for Ba.[5]

Instability in presence of $CO_2$ was reported by Zhang et al. for all Ln investigated (Ln = La, Pr, Nd, Sm, Gd and Y). All compounds show pickup of $CO_2$ forming carbonate at high $p_{CO_2}$.[59] For Ln = Gd Tarancon et al. found that pickup occur if $p_{CO_2}$ > 1 %, while in air ($p_{CO_2}$ < 500 ppm) carbonates are not formed.[64,78]

## 2.6 Interpretation of X-ray diffraction patterns

X-ray powder diffraction is a widely used experimental technique to identify which phases are present, and to investigate the structure of these phases. An incident beam of X-rays hits the plane surface of powder to be analysed. The lattice is of the same length scale as the X-rays and will therefore diffract the beam. The angle of the refracted beams is then a fingerprint for the compound. Both the kind of lattice and the atoms within it effect the diffraction pattern. An example of a cubic perovskite structure is given in **Figure 2.11**. In a cubic structure all crystallographic planes with permutations of (hkl) are equal. If the symmetry is reduced to tetragonal (a = b $\neq$ c) only permutations of h and k gives the same angle of refraction. This cause the peaks to split into two peaks with one more intense. If symmetry is further reduced to orthorhombic (a $\neq$ b $\neq$ c) three peaks will appear instead of a single in the cubic case.

Most commonly radiation used is Cu K$\alpha_{1,2}$. The two are very similar in wave length making it hard to filter out only one of them. Cu K$\alpha_2$ has slightly longer wavelength ($\lambda$ = 1.5444 Å) which leads to a small shift to higher angles compared to the peak from Cu K$\alpha_1$ ($\lambda$ = 1.5406 Å). The X-ray beam can also have other wavelengths for instance from tungsten which is typically the filament in an X-ray source. Tungsten radiation, W L$\alpha_{1,2}$, has shorter wavelength ($\lambda$ = 1.4706 Å) than Cu K$\alpha_1$ yielding peaks shifted to lower angles. Filters can be used to remove unwanted X-ray wavelengths but at the cost of intensity in the scan. If a material is heated, the lattice expands is cause a shift of peaks towards lower angles.

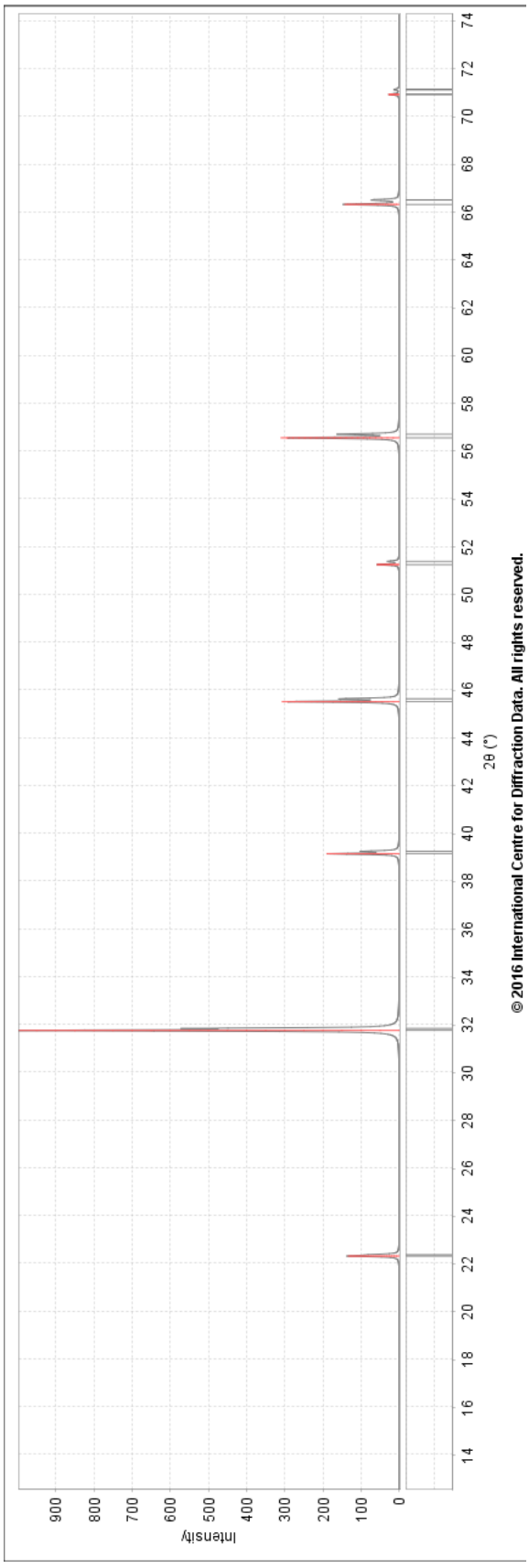


**Figure 2.11:** XRD pattern of cubic perovskite.

# Chapter 3

# Experimental

## 3.1 Synthesis

$YBaCo_2O_{5+\delta}$ (YBCO) have been synthesised by the solid state method. Manufacturer and purity of the precursors are given in **Table 3.1**. Precursors of $Y_2O_3$, $BaCO_3$ and $Co_3O_4$ were dried for at least 12 hours in a chamber furnace. Yttria is the most hygroscopic compound and was therefore dried at 700 °C, while barium carbonate and cobalt oxide was dried at 200 °C. The compounds were then, one at the time, taken out of the hot furnace and put into a desiccator with silica to avoid water absorption while cooling to room temperature. When cooled the precursors were weighed in stoichiometric ratios, according to **Equation (3.1)**. Both yttria and cobalt oxide powder quickly adsorb water and weighing therefore needs to be performed fast to assure stoichiometric amounts. To reduce the problem of water adsorption during weighing, the time to weigh yttria was reduced taking out a rough amount and measure it exactly, and use it to calculate the amount of other precursors, instead of weighing all compounds to predetermined masses.

$$\frac{1}{2}Y_2O_3 + BaCO_3 + \frac{2}{3}Co_3O_4 + \frac{6\delta - 1}{12}O_2 \longrightarrow YBaCo_2O_{5+\delta} + CO_2 \tag{3.1}$$

Yttria was ball milled in ethanol for 24 hours with yttria stabilised zirconia (YSZ) balls in a 250 mL PET bottle. Cobalt oxide and barium carbonate was added and all three precursors mixed together for 12 hours. The rotation speed was adjusted to give an optimal milling angle to achieve efficient milling and mixing. The slurry was separated from the balls with a sieve and rinsed off with more ethanol. The ethanol in the slurry was evaporated on a hot plate for several hours to achieve a powder.

**Table 3.1:** Overview of the precursors used for solid state synthesis of $YBaCo_2O_{5+\delta}$.

| Compound | Producer | Purity |
|---|---|---|
| $Y_2O_3$ | Alfa Aesar | ≥ 99.9 |
| $BaCO_3$ | Sigma-Aldrich | ≥ 99 |
| $Co_3O_4$ | Inframat Advanced Materials | ≥ 99.9 |

The powder was then ground in an agate mortar before it was sieved through a sieve with 70 µm openings. The powder was then pressed into Ø15 mm pellets with 50 MPa pressure. Further the pellets were calcined for 48 hours at 1000 °C with ramp rate of 200 °C/h. When it was cooled to room temperature it was ground, first with a steel mortar, then with an agate mortar. The two grinding steps were performed to avoid fracturing of the agate mortar. Powder were ground in small quantities to assure thoroughly grinding. Further it was mixed together and ground again to thoroughly grind and mix the powder. The phase purity was investigated with XRD, see Section 3.2. To increase the phase purity the material was re-calcined and re-ground five times, and the calcination temperature was increased to 1130 °C to increase reactivity. In total the five repetitions of calcination took 132 hours at temperature in the range of 1000 – 1130 °C. Drying and calcination were performed in Nabertherm chamber furnaces, **Figure 3.1 (a)**.

After successfully obtaining a phase-pure material the powder was annealed in oxygen atmosphere at 350 °C for 12 hours with ramp rate of 200 °C $h^{-1}$ in a tubular Nabertherm furnace, **Figure 3.1 (b)**.

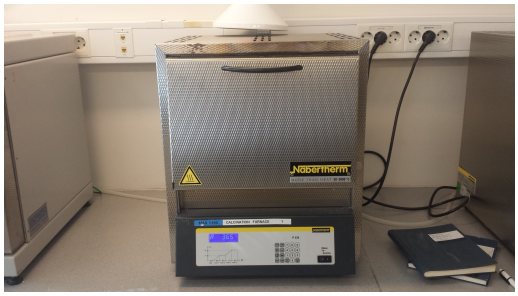


**(a)**

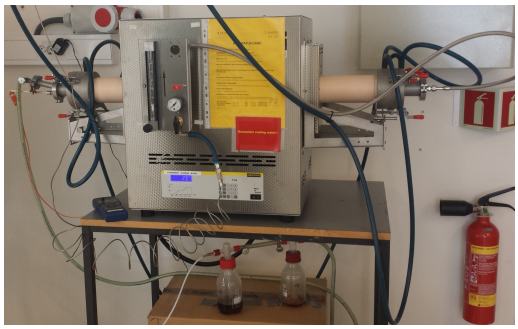

**(b)**

**Figure 3.1: (a)** Chamber furnace used for drying and calcination. **(b)** Tubular furnace used for controlled atmosphere.

## 3.2 X-ray powder diffraction

### 3.2.1 Ambient measurements

The phase purity and structure of the as-synthesised and oxidised powders were examined with x-ray powder diffractomter *Bruker D8 Advance DaVinci*. $2\theta$ range used was 10° to 75° with step size of 0.0136°, and a total scan time of one hour.

Another diffractometer, *Bruker D8 Focus*, was used to verify reduction after ex situ TGA, and to analyses phases after in situ TGA. The instrument was also used to investigate the structure of $YBaCo_2O_{5+\delta}$ after annealing in argon for 12 hours at 800 °C, and after annealing in air (chamber furnace) at 800 °C and 900 °C for 5 hours. $2\theta$ range used was 10° to 76° with step size of 0.0128°, and a total scan time of 63 min.

**Table 3.2:** Experimental parameters for X-ray diffraction measurements

| | Bruker D8 Advance | Bruker DaVinci-1 | Bruker D8 Focus |
|---|---|---|---|
| Geometry: | Bragg–Brentano | Bragg–Brentano | Bragg–Brentano |
| Goniometer type: | $\theta$ / $\theta$ | $\theta$ / $\theta$ | $\theta$ / $2\theta$ |
| Radiation: | Cu K$\alpha_{1,2}$ | Cu K$\alpha_{1,2}$ (Cu K$\beta_1$,W L$\alpha_{1,2}$) | Cu K$\alpha_{1,2}$ |
| Rotation: | no | yes | no |
| Soller Slit: | 2.5° | 2.5° | 2.5° |
| Goniometer Radius: | 217.5 | 280 | 200.5 |
| Detector PSD: | Vantec-1 | LynxEye XE | LynxEye SuperSpeed |
| PSD Window: | 6° | 3° | 3° |
| Generator: | 40kV, 40mA | 40kV, 40mA | 40kV, 40mA |
| Divergence slit: | 0.2° | 0.2° | 0.5° |

### 3.2.2 Non ambient measurements

For high temperature structure determination a *Bruker D8 Advance* diffractometer was used with a resistive heating element inside a small cylindrical furnace. The setup of diffractometer and furnace can be seen in **Figure 3.2 (a)**. The sample holder used was a rectangular crucible made of alumina, **Figure 3.2 (b)**. The instrument has a lot of irregular background noise below 20°, and this was therefore set as minimum for $2\theta$ range. The maximum of the $2\theta$ range was set to 72°. When analysing the data the minimum for the $2\theta$ was increased to 22° due to irregular background without information below 22°. The scan had a step size of 0.0163° and a scan time of one hour per temperature.

The XRD-measurement was conducted upon heating. X-ray diffractogram was collected at room temperature, and then programmed to increase with steps of 100 °C up to 400 °C, and further up to 1000 °C with steps of 50 °C, and finally at room temperature again. The actual temperature was lower than programmed in the diffractometer, and can be seen as legend in the results section, e.g. **Figure 4.9**. The actual temperature was determined by running a parallel of the experiment in advance with alumina, and calculating the temperature based on the thermal expansion. The heating rate between measurements was fast, $9\,^{\circ}\mathrm{C\,min^{-1}}$, with 10 minutes hold to (hopefully) obtain equilibrium before measuring the diffraction pattern. The measurement was conducted in oxygen, air and nitrogen with the same starting material for all atmospheres.

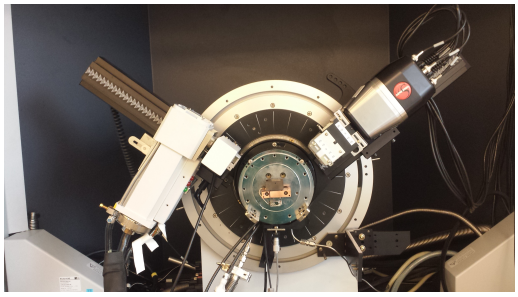

**(a)**

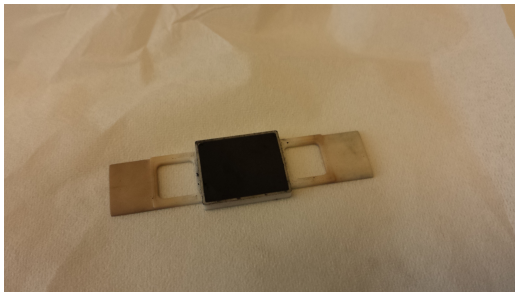

**(b)**

**Figure 3.2: (a)** HTXRD setup. **(b)** Aluminia sample holder for HTXRD measurements.

### 3.2.3 Analysis of diffraction patterns

Measured diffractograms were compared with powder diffraction files/patterns from *International Centre for Diffraction Data*-database with *Bruker DIFFRAC.EVA V4.1* software. Pawley-fitting and Rietveld refinment was conducted with the software *Bruker Topas 5*.

## 3.3 Thermogravimetric analysis

### 3.3.1 Ex-situ TGA (absolute oxygen content)

The absolute oxygen content of oxidised $YBaCo_2O_{5+\delta}$ was found by weighing an exact amount of powder ≈ 100 mg before and after reduction. The powder was reduced in a tubular Nabertherm furnace in a gas mixture of 5 % $H_2$ and 95 % Ar at 1100 °C for 12 hours. The complete reduction of cobalt was verified by ambient XRD.

### 3.3.2 In-situ TGA (relative oxygen content)

A Netzsch Thermal analysis system 4 (STC449), **Figure 3.3 (a)**, was used to measure the weight loss/gain during heating in oxygen, air and nitrogen. A small amount of powder (≈ 30 mg) was put into a small alumina crucible and accurately weighed. The sample was placed on the platinum holder together with the empty reference crucible before the chamber was closed, evacuated and filled with appropriate gas (oxygen, air or nitrogen). The flow was set to 30 $cm^3$/min throughout the measurement, but fluctuated to a slight extent. To correct for buoyancy a background measurement with only the empty crucible was obtained for each atmosphere and subtracted from each measurement. **Figure 3.3 (b)** shows a crucible with powder to be analysed together with an empty reference crucible on the platinum holder.

Thermogravimetric analysis was performed stepwise with a heating rate of 9 °C $min^{-1}$. Initially the sample was heated up to 150 °C to remove water, then cooled to a temperature of 100 °C before steps of 25 °C was used up to a temperature of 1100 °C.

Each temperature was held for 30 minutes to obtain equilibrium. The oxygen content at each step was calculated by a mass balance equation based upon the initial mass, initial oxygen content and the mass after holding for 30 minutes, according to **Equation 3.2**, which is solved for $5+\delta$ in **Equation 3.3**.

$$\frac{m}{M} = \frac{m_{initial}}{M_Y + M_{Ba} + 2M_{Co} + (5+\delta)_i M_O} = \frac{m_{final}}{M_Y + M_{Ba} + 2M_{Co} + (5+\delta)_f M_O} \tag{3.2}$$

$$(5+\delta)_{final} = \frac{\frac{m_f}{m_i}(M_Y + M_{Ba} + 2M_{Co} + (5+\delta)_i M_O) - (M_Y + M_{Ba} + 2M_{Co})}{M_O} \tag{3.3}$$

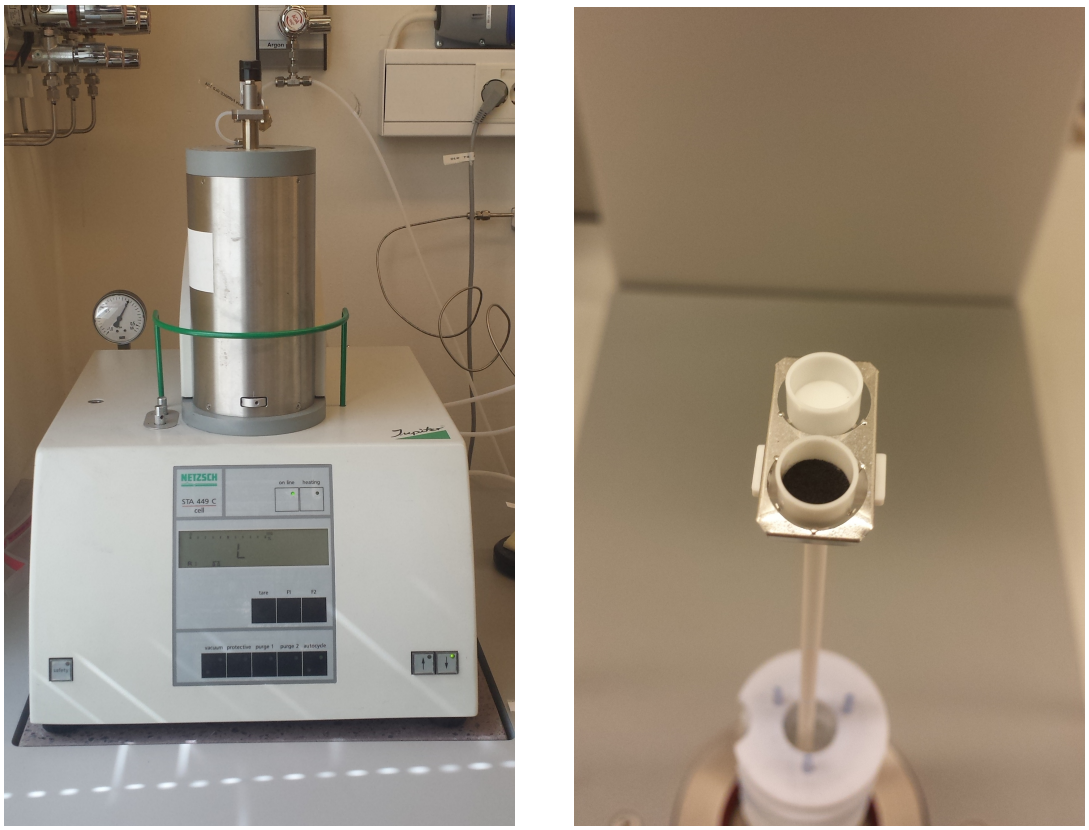


**(a)** **(b)**

**Figure 3.3:** **(a)** Thermal analysis system used for in situ TGA **(b)** Crucible with powder and empty reference crucible.

# Chapter 4

# Results

## 4.1 Phase purity

A phase-pure material was obtained after five calcination steps at 1000 – 1130 °C. The XRD pattern after each calcination step can be seen in **Figure 4.1**. Initially secondary phases corresponding to yttria (square symbol) and barium cobaltite (triangle symbol) were present, but with several grinding and calcination steps the amount of secondary phases were reduced, yielding a phase pure material. The circle symbol corresponds to main phase due to traces of tungsten radiation. The uppermost diffraction pattern is from the material which later was oxidised and used for HTXRD and TGA.

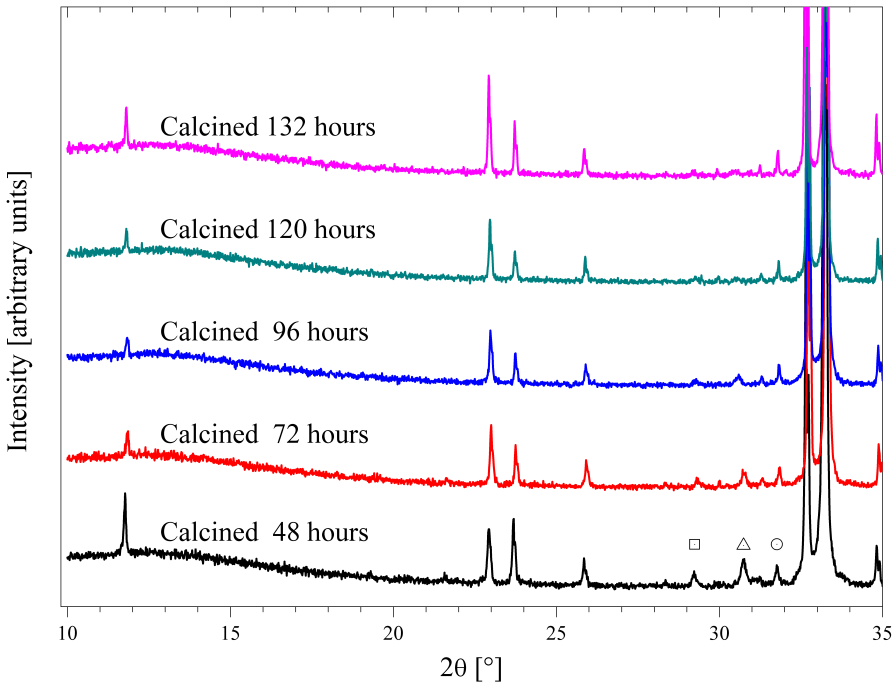


**Figure 4.1:** X-ray diffractogram of $YBaCo_2O_{5+\delta}$ after one to five calcination steps. Square marks the main reflection of yttria, triangle corresponds to barium cobaltite, while circle correspond to main phase from tungsten radiation. The pink curve (calcined five times, total of 132 hours) is from the powder which later was annealed in oxygen and used for HTXRD and TGA.

## 4.2 Crystal structure

### 4.2.1 Room temperature structure of as-synthesised YBCO

The as-synthesised diffraction pattern matches PDF04-017-9319 based on the work of Aurelio et al.[79] The space group is given as Pmmm with a = 3.8752 ≈ b = 3.8777, c = 7.4992 (122 structure). However, using tetragonal P4/mmm (a $\stackrel{!}{=}$ b = 3.87, c = 7.50, 112 structure) also explains all reflections. The closest model was PDF01-075-3613 by Vogt et al. with a = 3.891, c = 7.499, however, no lattice sites were given in the model.[80] A similar model based on $HoBaCo_2O_{5+\delta}$, PDF04-019-2264, was therefore adopted for Rietveld refinement. **Figure 4.2** shows diffractogram with bars indicating allowed reflections for different models. Crystallographic data are given in **Table 4.1**. The lattice positions for the Ho-adapted model are given in **Table 4.2**. The lattice parameter c is doubled compared to single perovskite as expected from A-site ordering of yttrium and barium ions.

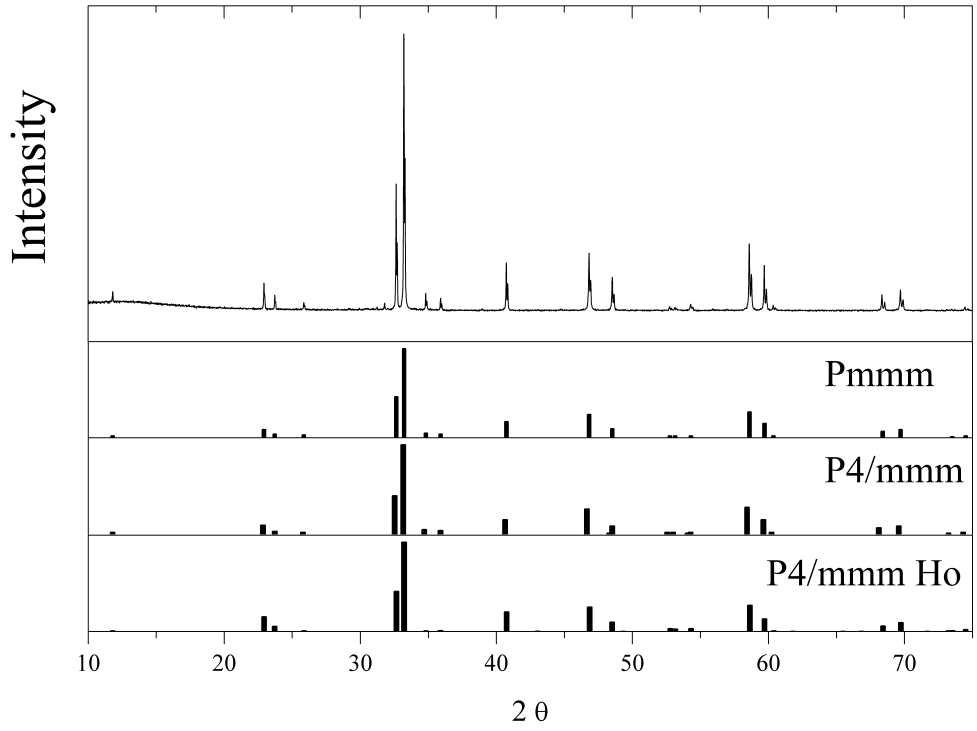


**Figure 4.2:** X-ray diffractogram of phase-pure, as-synthesised $YBaCo_2O_{5+\delta}$.

**Table 4.1:** Room temperature crystallographic data of as-synthesised $YBaCo_2O_{5+\delta}$ from literature and Rietveld refinement.

| Figure legend | PDF | Space group | a [Å] | b [Å] | c [Å] | Reference |
|---|---|---|---|---|---|---|
| Pmmm | 04-017-9319 | Pmmm | 3.875 | 3.878 | 7.499 | [79] |
| P4/mmm | 01-075-3613 | P4/mmm | 3.891 | — | 7.499 | [80] |
| P4/mmm Ho | 04-019-2264 | P4/mmm | 3.875 | — | 7.5 | [81] |
| — | — | P4/mmm | 3.879 | — | 7.502 | Refined |

**Table 4.2:** Structure adapted from Ho-model. Only the lanthanide is changed. x,y,x = Atomic position in unit cell. Np = Multiplicity of atomic position in unit cell. Occ. = Occupancy. Beq. = thermal motion parameter.

| Atom | Np | x | y | z | Occ. | Beq. |
|---|---|---|---|---|---|---|
| $O^{2-}$ #1 | 4 | 0 | 0.5 | 0.2085 | 1 | 1 |
| $Co^{3+}$ | 2 | 0 | 0 | 0.242 | 1 | 1 |
| $Ba^{2+}$ | 1 | 0.5 | 0.5 | 0.5 | 1 | 1 |
| $Y^{3+}$ | 1 | 0.5 | 0.5 | 0 | 1 | 1 |
| $O^{2-}$ #2 | 1 | 0 | 0 | 0.5 | 1 | 1 |
| $O^{2-}$ #3 | 1 | 0 | 0 | 0 | 0.25 | 1 |

A diffractogram with only refined lattice parameters is shown in **Figure 4.3**. Result of Rietveld refinement of as-synthesised $YBaCo_2O_{5+\delta}$ refined with adapted Ho-model are shown in **Table 4.3**. The first column is from only refining lattice parameters, while for the second column lattice parameter, $z_{O^{2-}\ \#1}$, $z_{Co^{3+}}$ and occupancy of $O^{2-}$ #3 are refined.

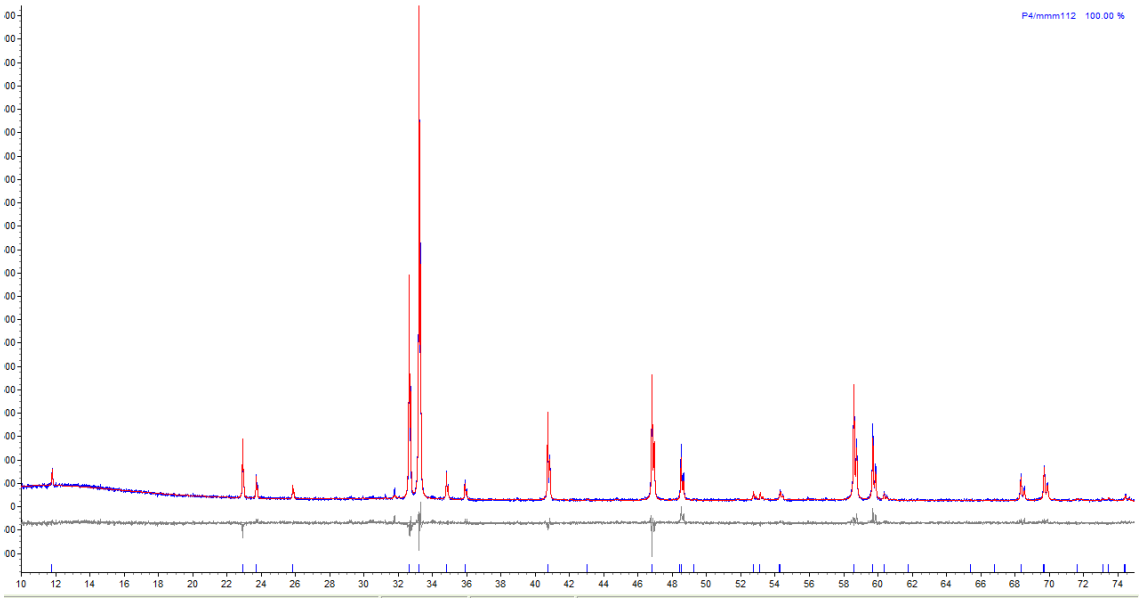


**Figure 4.3:** X-ray diffractogram (blue) with calculated (red) and difference curve (grey) of as-synthesised $YBaCo_2O_{5+\delta}$.

**Table 4.3:** Result of Rietveld refinement of as-synthesised $YBaCo_2O_{5+\delta}$. Refinement 1 shows result when only lattice parameters are refined. Refinement 2 shows result when refining lattice parameters, lattice positions and occupancy of oxygen are refined. Refined values are shown in red. The lowest 8 rows are parameters describing the accuracy of the refinement.

| | Refinement 1 | Refinement 2 |
|---|---|---|
| a [Å] | 3.87936 | 3.87938 |
| c [Å] | 7.50166 | 7.50170 |
| $z_{O^{2-}\ \#3}$ | 0.2085 | 0.19241 |
| $z_{Co^{3+}}$ | 0.242 | 0.24503 |
| Occ. $O^{2-}$ | 0.25 | 0.2663 |
| GOF | 1.44 | 1.39 |
| Rexp | 6.4 | 6.39 |
| Rwp | 9.19 | 8.86 |
| Rp | 7.03 | 6.78 |
| Rexp-dash | 15.08 | 15.07 |
| Rwp-dash | 21.65 | 20.88 |
| Rp-dash | 26.57 | 25.62 |
| Weighted Durbin Watson | 1.09 | 1.16 |

### 4.2.2 Room temperature structure after oxidation

After annealing in oxygen the structure is orthorhombic, evident by peaks splitting into three, instead of two peaks in the tetragonal case. The diffraction pattern correspond to $YBaCo_2O_{5+\delta}$ with PDF 04-014-5240 based on the work of Aurelio et al.[40] The space group is given as Pmmm with a = 3.822, b = 7.858 and c = 7.525. However, using Pmmm with a = 3.927, b = 3.828 and c = 7.521 seems also able to explain the orthorhombic pattern, without having to double the b parameter. These values of cell parameters are not found in the database. PDF 04-017-2845, based on Seddon et al.,[82] has Pmmm 112 structure, but with different cell parameters. Diffractogram with bars indicating the allowed reflections are presented in **Figure 4.4**. Crystallographic information are given in in **Table 4.4**.

Although the smaller model (Pmmm 112 structure) was thought to fit all peaks and was used for refining the XRD-data initially, the later refinements were conducted with 122 structure. The change in structure from tetragonal to orthorhombic is reported to be caused by ordering of vacancies. Doubling of one cell parameter is the smallest unit cell which can account for this ordering. Further there exists one weak reflection in the pattern that the 122 structure can explain – the (011) reflection at 16.3°, which the 112 structure cannot explain. **Figure 4.5** shows Pawley fitting with both models for a selected range to highlight the forbidden reflection with 112 model. The blue triangles show the allowed reflections with 122 structure, while bars below the triangles show allowed reflections for 112 model – which is absent at 16.3°.

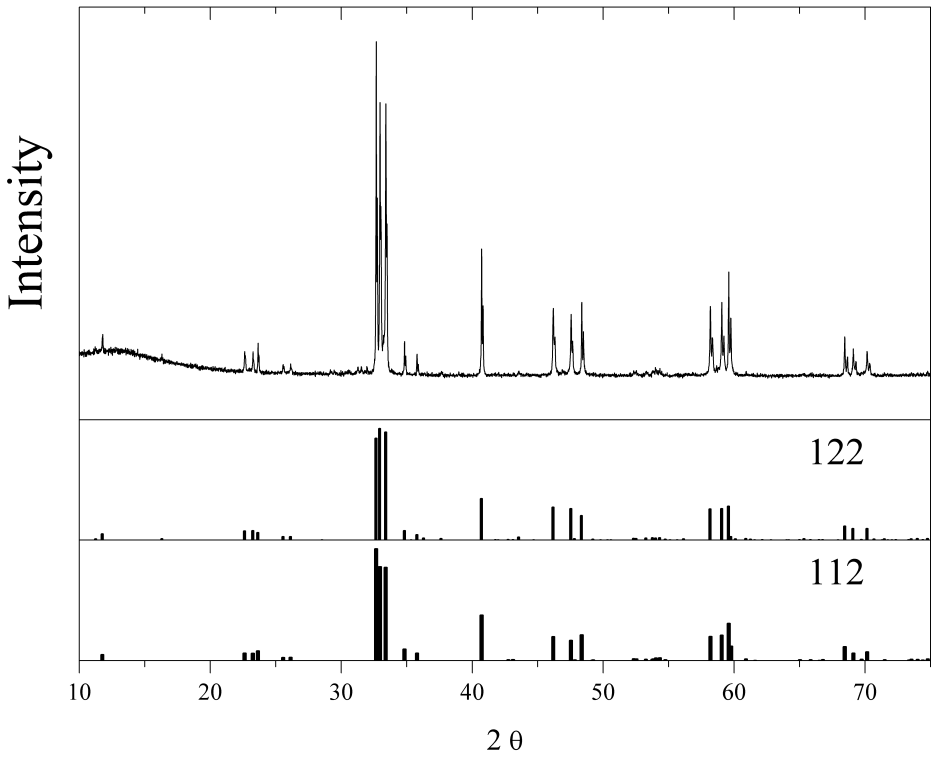


**Figure 4.4:** X-ray diffractogram of oxidised $YBaCo_2O_{5+\delta}$.

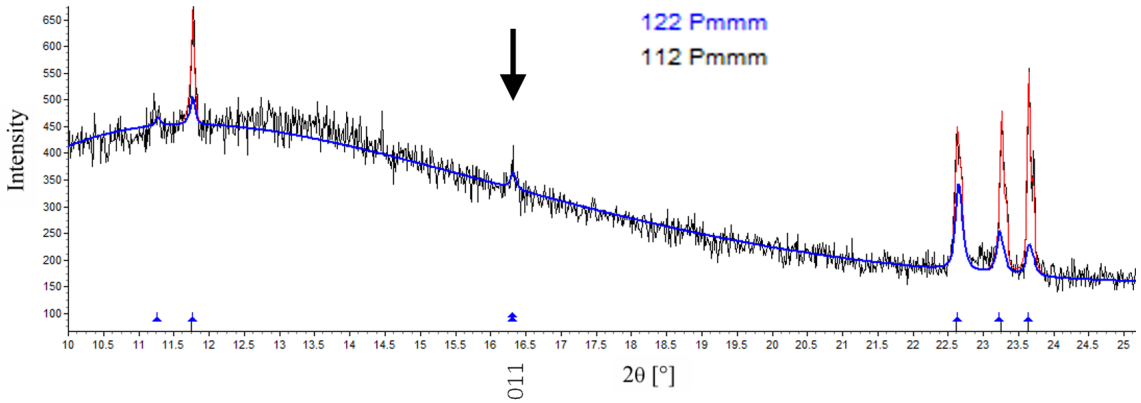


**Figure 4.5:** X-ray diffractogram of oxidised $YBaCo_2O_{5+\delta}$ showing minor reflecting which is only present in 122 structure and not 112 structure.

**Table 4.4:** Room temperature crystallographic data of oxidised $YBaCo_2O_{5+\delta}$ from literature and Rietveld refinement.

| Figure legend | PDF | Space group | a [Å] | b [Å] | c [Å] | Reference |
|---|---|---|---|---|---|---|
| 112 | — | Pmmm | 3.927 | 3.828 | 7.521 | Refined |
| 122 | 04-014-5240 | Pmmm | 3.822 | 7.858 | 7.525 | [40] |
| not used | 04-017-2845 | Pmmm | 3.930 | 3.866 | 7.603 | [82] |
| — | — | Pmmm | 3.823 | 7.857 | 7.523 | Refined |

**Table 4.5:** 122 structure from Aurelio et al.[40] x,y,x = Atomic position in unit cell. Np = Multiplicity of atomic position in unit cell. Occ. = Occupancy. Beq. = thermal motion parameter.

| Atom | Np | x | y | z | Occ. | Beq. |
|---|---|---|---|---|---|---|
| $Y^{3+}$ | 2 | 0.5 | 0.2692 | 0.5 | 1 | 1 |
| $Ba^{2+}$ | 2 | 0.5 | 0.244 | 0 | 1 | 1 |
| $Co^{3+}$ | 2 | 0 | 0.5 | 0.25 | 1 | 1 |
| $Co^{3+}$ | 2 | 0 | 0 | 0.26 | 1 | 1 |
| $O^{2-}$ #1 | 1 | 0 | 0 | 0 | 1 | 1 |
| $O^{2-}$ #2 | 1 | 0 | 0.5 | 0 | 1 | 1 |
| $O^{2-}$ #3 | 1 | 0 | 0.5 | 0.5 | 0.81 | 1 |
| $O^{2-}$ #4 | 1 | 0 | 0 | 0.5 | 0.12 | 1 |
| $O^{2-}$ #5 | 2 | 0.5 | 0 | 0.3126 | 1 | 1 |
| $O^{2-}$ #6 | 2 | 0.5 | 0.5 | 0.267 | 1 | 1 |
| $O^{2-}$ #7 | 4 | 0 | 0.2437 | 0.2984 | 1 | 1 |

Result of Rietveld refinement of oxidised $YBaCo_2O_{5+\delta}$ refined with 122-model are shown in **Table 4.6**. Only lattice parameters were refined. Initially the pattern was believed to be single phase orthorhombic, but closer examination showed presence of tetragonal phase (~7 %). The diffractogram is shown in **Figure 4.6**, tetragonal phase is highlighted in blue. The selected ranges with reflections indicating that the tetragonal phase is present are shown in **Figure 4.7**.

**Table 4.6:** Result of Rietveld refinement of oxidised $YBaCo_2O_{5+\delta}$. The lowest 8 rows are parameters describing the accuracy of the refinement.

| | **Pmmm** | **P4/mmm** |
|---|---|---|
| Wt % phase | 93.09 | 6.91 |
| a [Å] | 3.82280 | 3.87361 |
| b [Å] | 7.85672 | — |
| c [Å] | 7.52306 | 7.50504 |
| | | |
| GOF | 1.42 | |
| Rexp | 6.64 | |
| Rwp | 9.45 | |
| Rp | 7.38 | |
| Rexp-dash | 16.34 | |
| Rwp-dash | 23.24 | |
| Rp-dash | 28.47 | |
| Weighted Durbin Watson | 1.1 | |

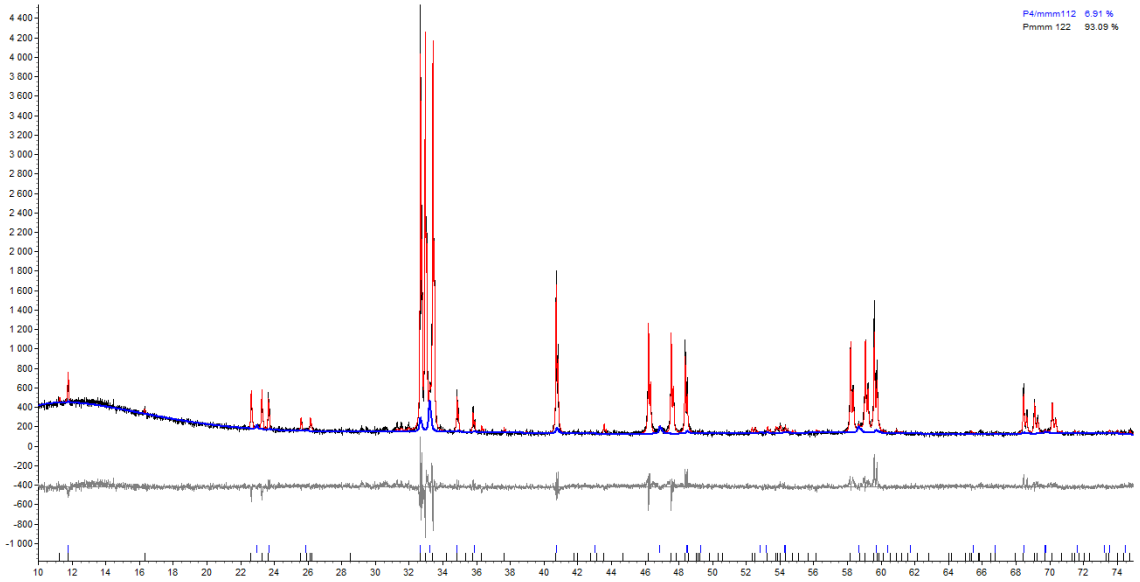


**Figure 4.6:** Refined X-ray diffractogram (black) with tetragonal contribution (blue), calculated (red) and difference curve (grey) of oxidised $YBaCo_2O_{5+\delta}$.

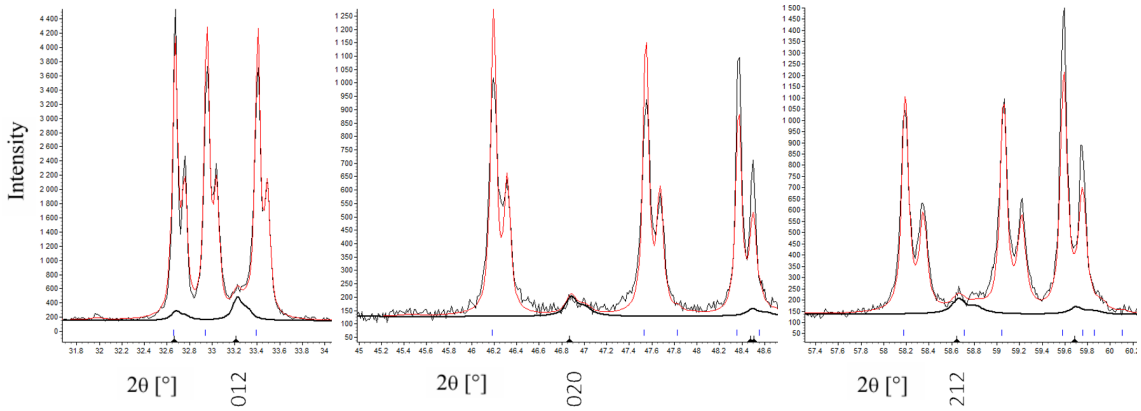


**Figure 4.7:** Refined X-ray diffractogram of oxidised $YBaCo_2O_{5+\delta}$ from selected ranges indicating that tetragonal phase is present.

### 4.2.3 Evolution of crystal structure at high temperature

The development of the crystal structure upon heating in different atmospheres are shown in **Figure 4.8** ($O_2$, first measurement), **Figure 4.9** ($O_2$, second measurement), **Figure 4.10** (air) and **Figure 4.11** ($N_2$). The measurement was conducted twice in oxygen to verify that the decomposition was reproducible.

At room temperature and up to 158 °C, the structure is orthorhombic in all atmospheres. In oxygen, the structure is still orthorhombic at 240 °C, whereas the pattern in air and nitrogen shows the presence of both tetragonal and orthorhombic phases. Above 322 °C the structure is tetragonal in all atmospheres. As earlier explained the orthorhombic pattern is recognised by peak splitting into three peaks, while tetragonal has two peaks, one weak and one more intense. The coexistence of tetragonal and orthorhombic structures can be seen by four peaks since the less intense peak from tetragonal overlap with the orthorhombic pattern. The "fourth" peak is most easily seen at $2\theta = 47°$, and can also be seen at $33°$ and $58.5°$. The transition temperature from orthorhombic to tetragonal increase with increasing partial pressure of oxygen ($p_{O_2}$). After the material had cooled to room temperature, the structure was orthorhombic in oxygen and tetragonal in air and nitrogen.

At higher temperatures the material decomposes in both oxygen and nitrogen. In oxygen, secondary phases appear above 655 °C. At 697 °C a peak appear at $2\theta = 26°$, the peak increased in intensity at 739 °C before it diminished at 781 °C and 823 °C. At 739 °C and 781 °C the main reflection of YBCO is close to absent in the first measurement and minimal in the second measurement, while at 823 °C the content of YBCO seems to have increased again. In nitrogen secondary phases have appeared at 823 °C and is even more evident when cooled to room temperature (labelled End 25 in **Figure 4.11**).

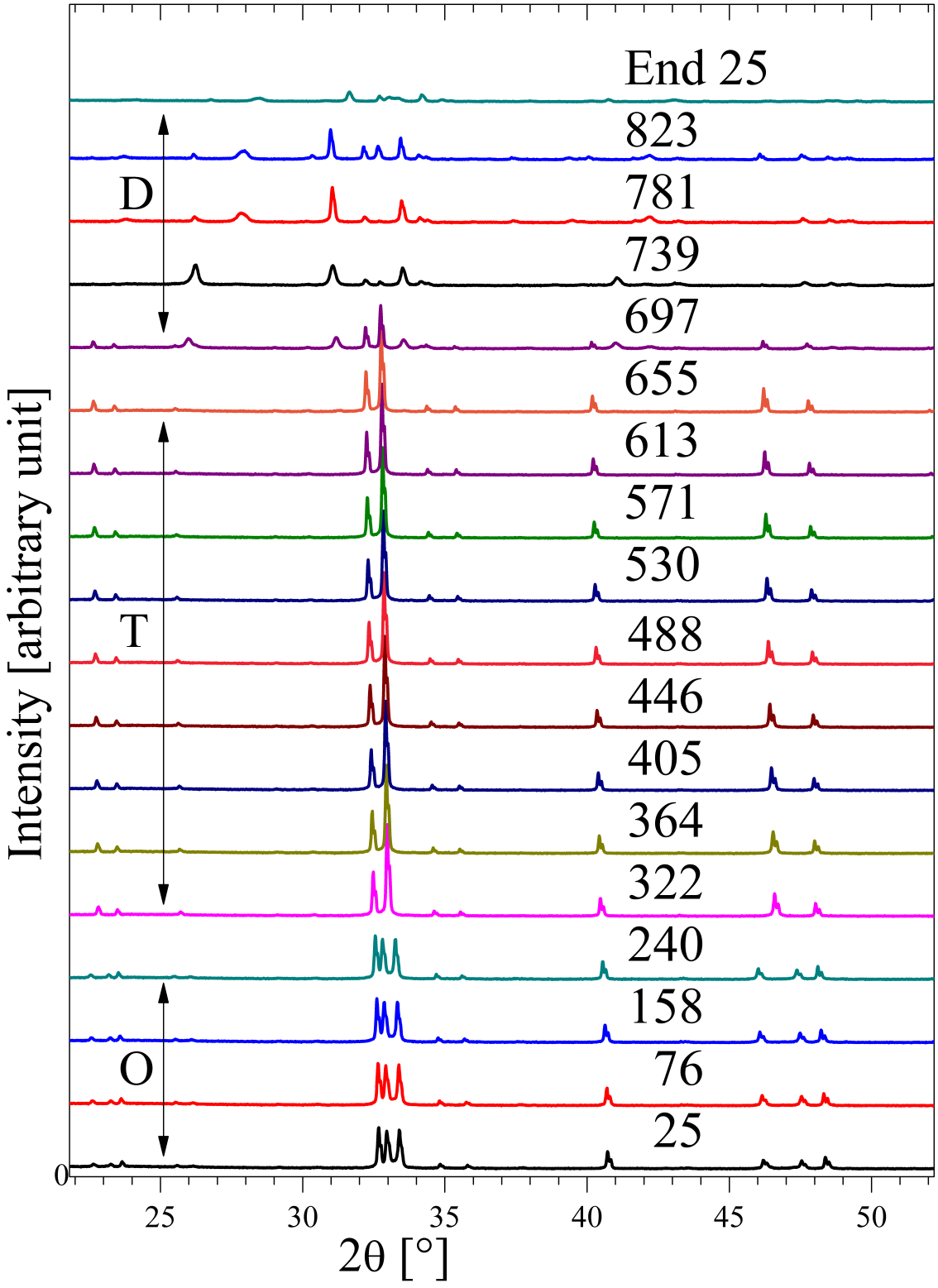


**Figure 4.8:** High temperature X-ray diffractogram of $YBaCo_2O_{5+\delta}$ from first of two experiments conducted in oxygen. The numbers in the graph area correspond to the temperature in °C of the diffractogram shown just below the number. Letters O, T and D indicates that the structure is either orthorhombic, tetragonal or (partly) decomposed, respectively.

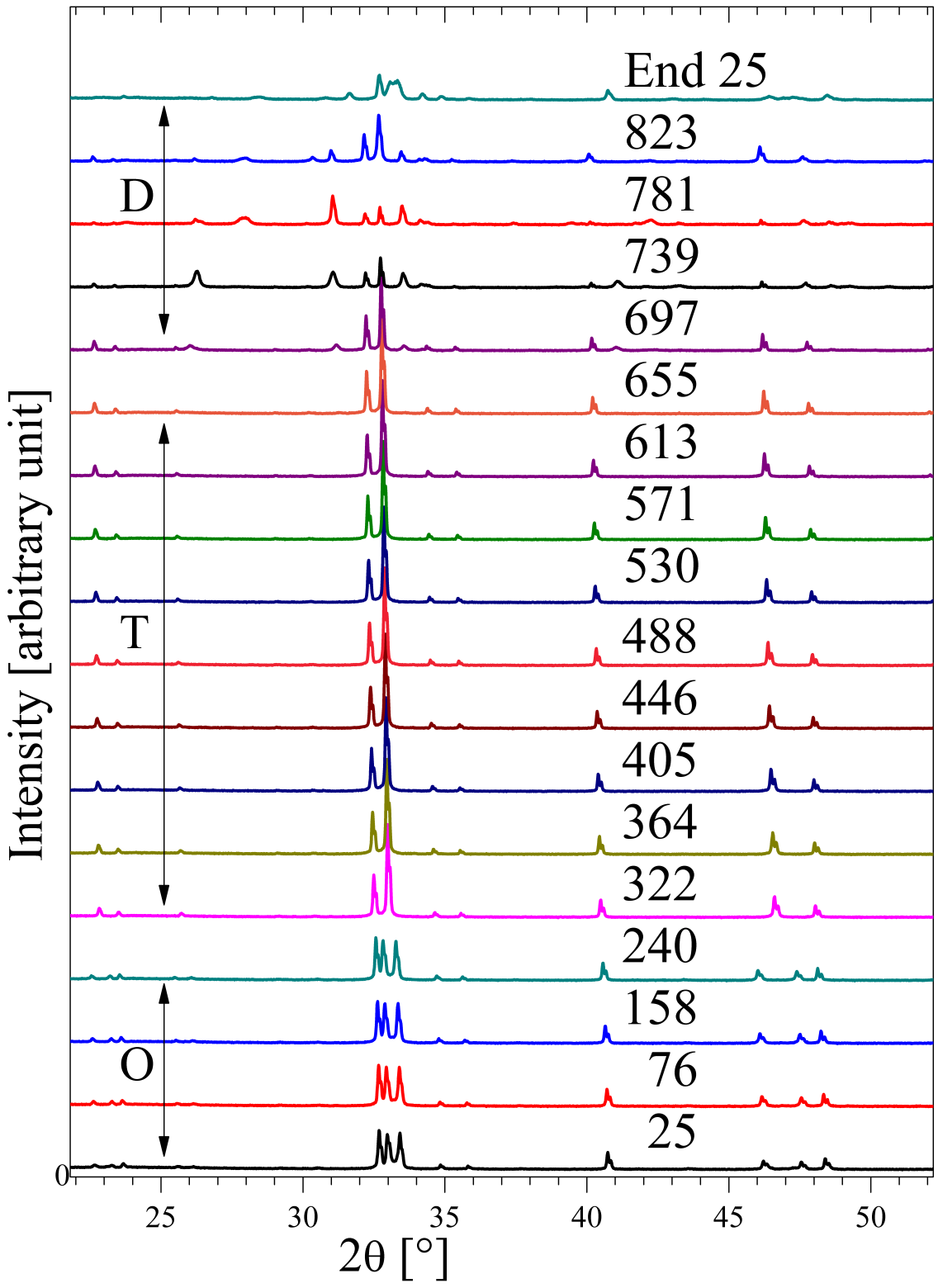


**Figure 4.9:** High temperature X-ray diffractogram of $YBaCo_2O_{5+\delta}$ from second of two experiments conducted in oxygen. The numbers in the graph area correspond to the temperature in °C of the diffractogram shown just below the number. Letters O, T and D indicates that the structure is either orthorhombic, tetragonal or (partly) decomposed, respectively.

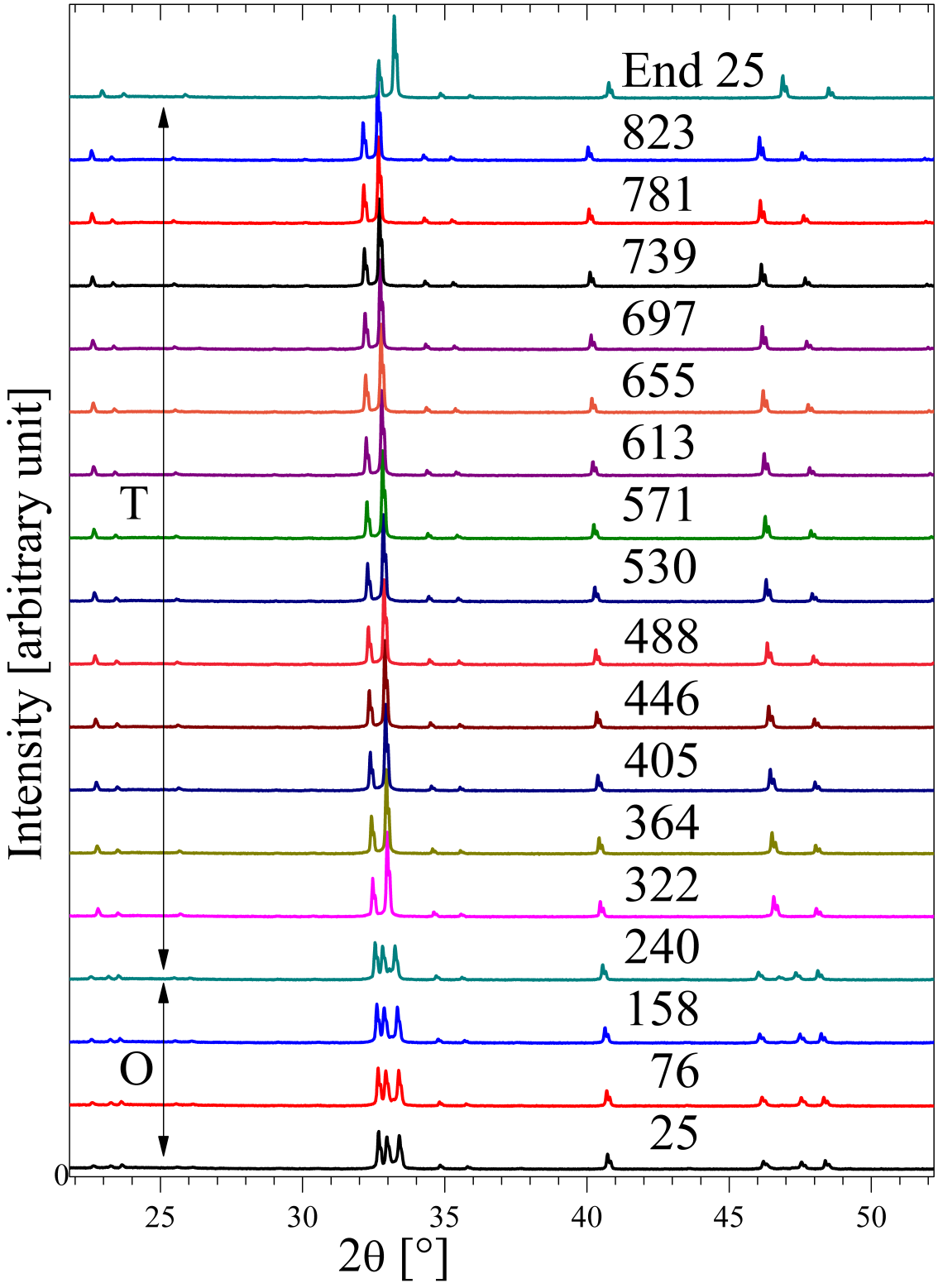


**Figure 4.10:** High temperature X-ray diffractogram of $YBaCo_2O_{5+\delta}$ in air. The numbers in the graph area correspond to the temperature in °C of the diffractogram shown just below the number. Letters O and T indicates that the structure is either orthorhombic or tetragonal, respectively. No sign of decomposition can be seen.

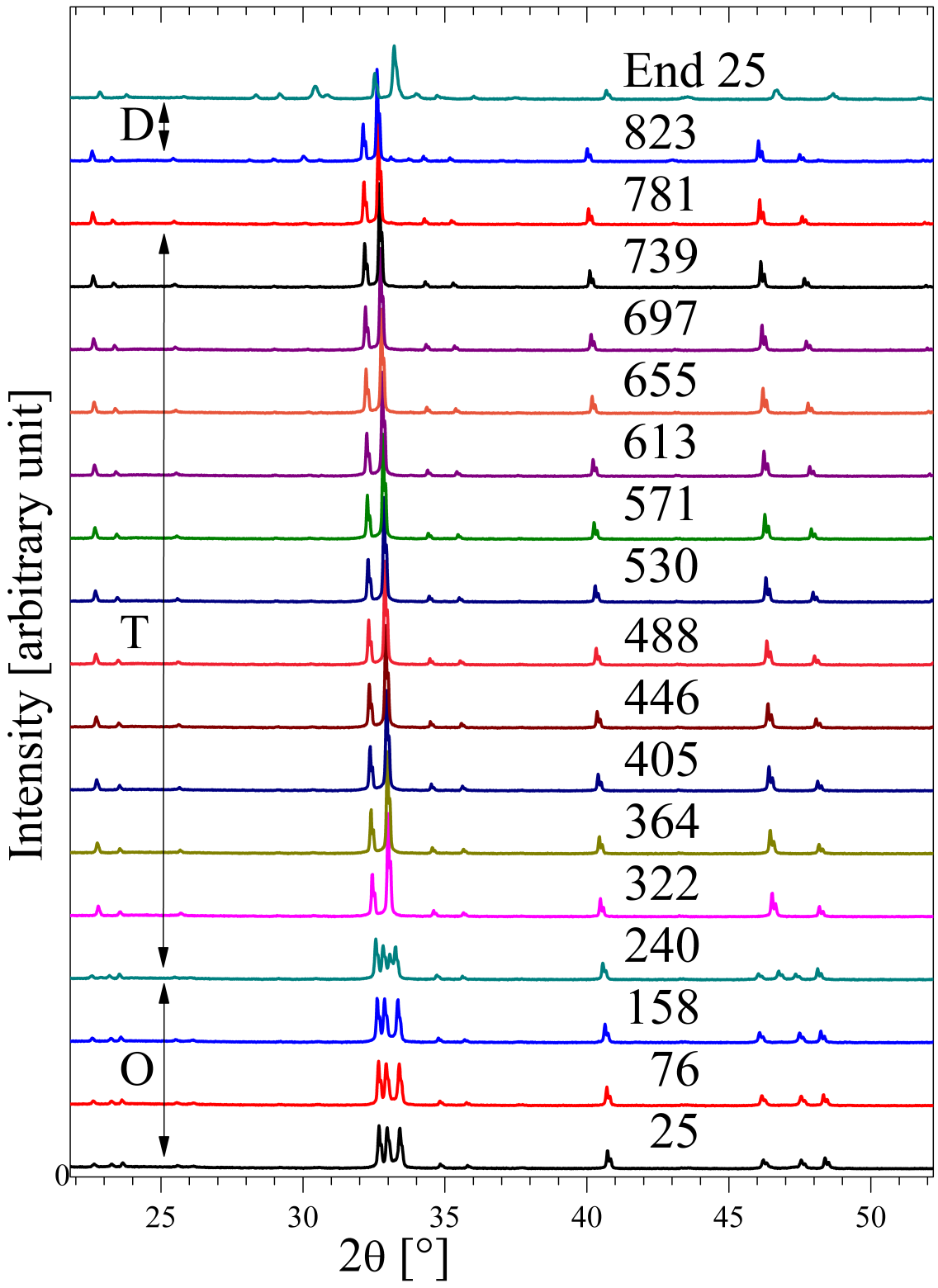


**Figure 4.11:** High temperature X-ray diffractogram of $YBaCo_2O_{5+\delta}$ in nitrogen. The numbers in the graph area correspond to the temperature in °C of the diffractogram shown just below the number. Letters O, T and D indicates that the structure is either orthorhombic, tetragonal or (partly) decomposed, respectively.

## 4.3 Oxygen stoichiometry

The oxygen content after annealing in oxygen was determined to 5.42 ± 0.02. Confirmation of reduction of cobalt to $Co^0$ (yttrium and barium still present as $Y^{3+}$ and $Ba^{2+}$) can be seen in **Appendix 6**.

The variation in oxygen content upon heating in $O_2$, air and $N_2$ is presented in **Figure 4.12**. The measurement was repeated due to unexpected increase in nitrogen. **Figure 4.13** show all seven measurements, three in $O_2$ and two in air and $N_2$. The initial increase in nitrogen was reproduced, but also occurred in air. The increase in $N_2$ and air, as well as the decrease in oxygen might be from deviation in buoyancy from background and measurement, or from measurement errors, more discussion about this is given in Section 5.4.

For temperatures below 200 °C oxygen content is quite constant with minor increase in $N_2$ and air as well as loss in $O_2$. The onset of thermal reduction occurs at the lowest temperature in nitrogen (225°C) followed by air (275°C) and oxygen (300°C).

In oxygen and air the oxygen content gradually decreases until 700 °C, where oxygen content stabilises. In oxygen atmosphere, the oxygen content shows an abrupt increase at 800 °C up to a level of 5.37, at 925 °C the oxygen content drops back to 4.9.

In air the oxygen content stays approximately constant above 700 °C, indicating that the minimum oxygen content is reached. A minor bump in oxygen content can be seen at approximately 850 °C.

In $N_2$ the oxygen content drops 0.5 in an interval less than 200 °C. It stabilises at a threshold oxygen content ~4.93, which is kept until temperature reaches 1000 °C, when a second drop in oxygen content appears.

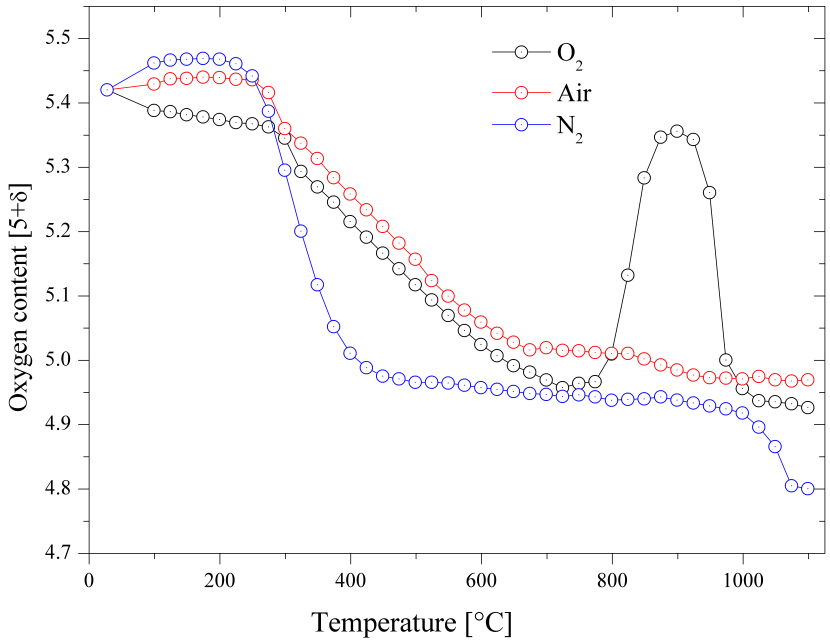


**Figure 4.12:** Oxygen content in $YBaCo_2O_{5+\delta}$ determined by TGA in oxygen (black), air (red) and nitrogen (blue)

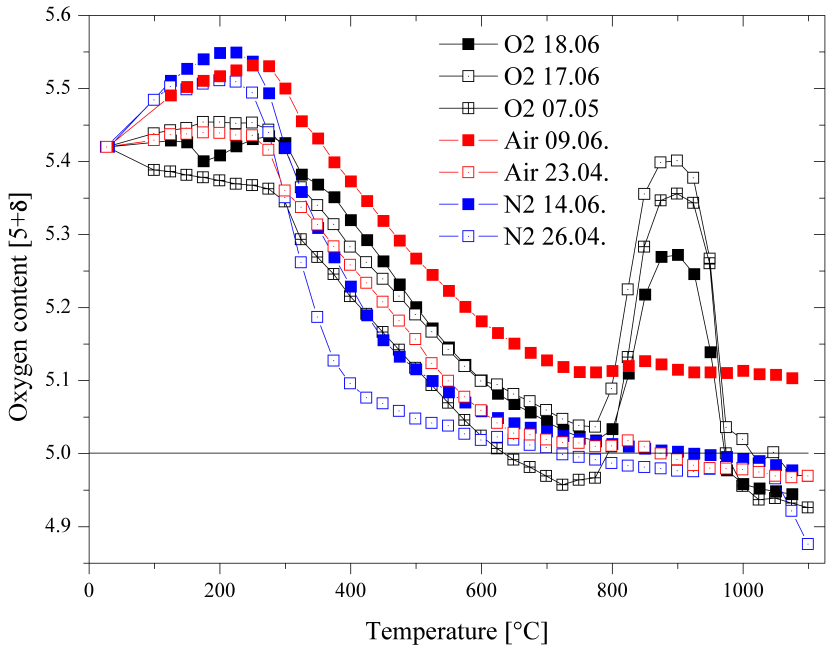


**Figure 4.13:** Oxygen content in $YBaCo_2O_{5+\delta}$ determined by TGA in oxygen (black), air (red) and nitrogen (blue)

## 4.4 Further XRD investigations

### 4.4.1 Secondary phases after HTXRD

Secondary phases in diffractoram measured at room temperature after hTXRD were identified using EVA. In oxygen, **Figure 4.14 (a)**, the pattern matches $YCO_3$ and $BaCoO_{3-\delta}$. For nitrogen, **Figure 4.14 (b)**, diffractogram matches with $BaYCo_4O_7$, $BaCo_{0.75}Y_{0.25}O_{2.55}$ and $Y_2O_3$.

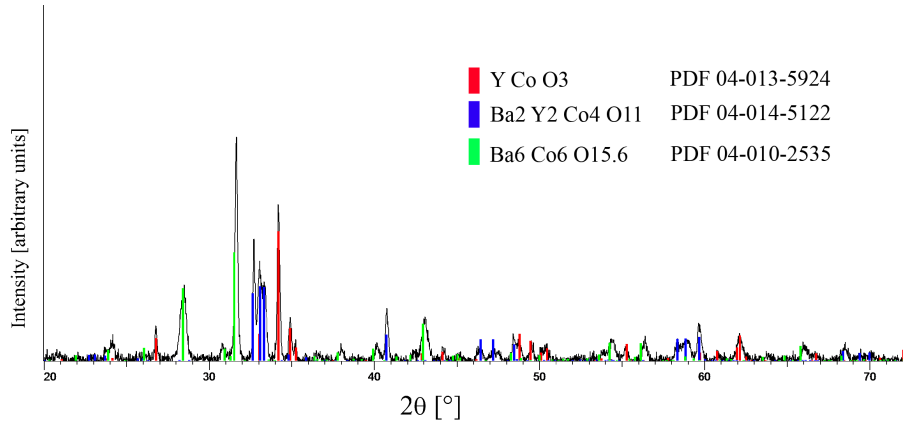


**(a)**

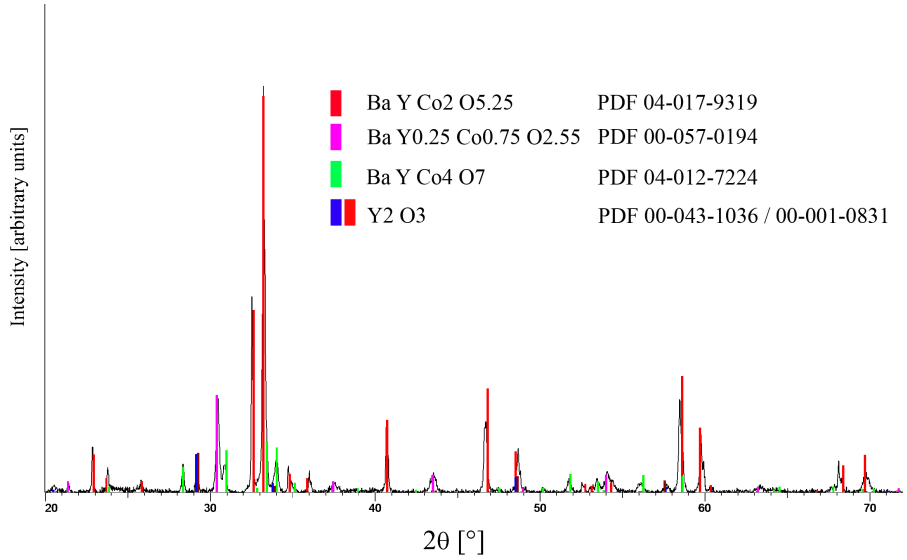


**(b)**

**Figure 4.14:** Room temperature measurement after HTXRD with secondary phases indexed with EVA. **(a)** Secondary phases $YCO_3$ and $BaCoO_{3-\delta}$ are present after oxygen measurement. and **(b)** Secondary phases $BaYCo_4O_7$, $BaCo_{0.75}Y_{0.25}O_{2.55}$ and $Y_2O_3$ are present after nitrogen measurement.

### 4.4.2 Secondary phases and crystal structure after TGA

The samples from TGA was analysed with regular XRD. **Figure 4.15** shows the phases present in $O_2$ **(a)**, air **(b)** and $N_2$ **(c)**.

In oxygen, the ex situ XRD diffractogram shows no secondary phases, but two $YBaCo_2O_{5+\delta}$ phases are co-existing. In air, the ex situ XRD pattern match tetragonal $YBaCo_2O_{5+\delta}$. In nitrogen, only the secondary phases $BaYCo_4O_7$, $BaCo_{0.75}Y_{0.25}O_{2.55}$ and $Y_2O_3$ are present.

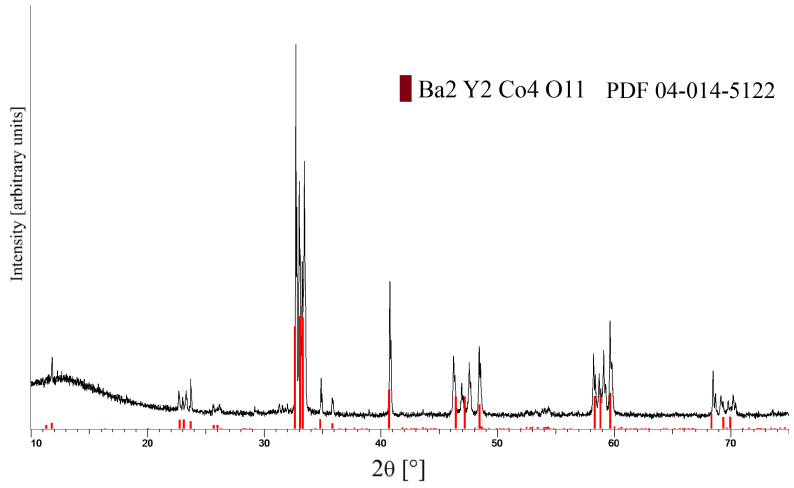


**(a)**

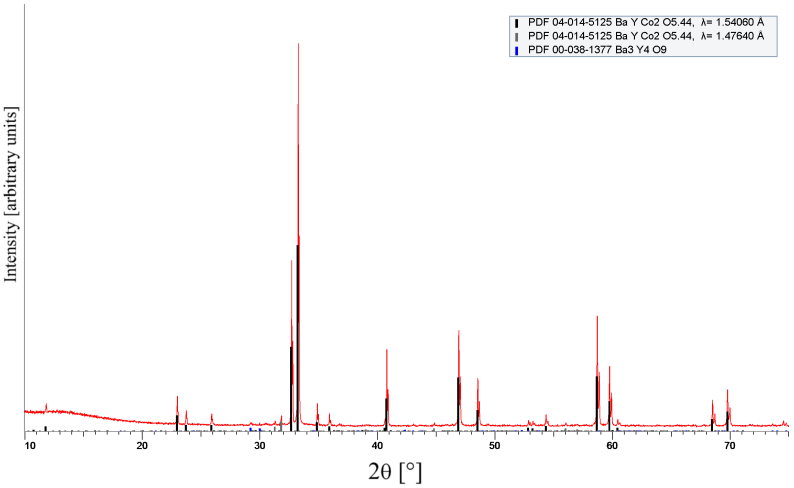


**(b)**

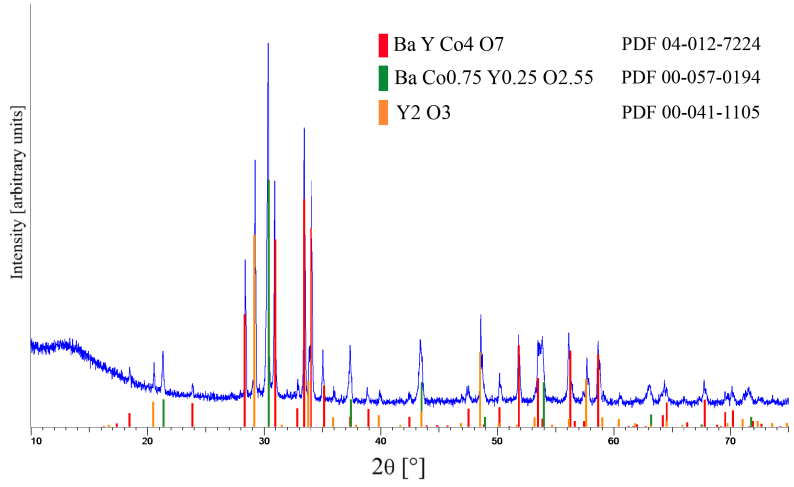


**(c)**

**Figure 4.15:** Regular XRD after TGA with phases indexed with EVA for **(a)** oxygen, **(b)** air and **(c)** nitrogen. The secondary phases $BaYCo_4O_7$, $BaCo_{0.75}Y_{0.25}O_{2.55}$ and $Y_2O_3$ are present in nitrogen.

### 4.4.3 Structure after annealing at 800 °C and 900 °C

During HTXRD in air, no secondary phases appeared in the HTXRD diffractogram. However, annealing in air for 5 h at 800 °C yield secondary phases, as shown in **Figure 4.16**. The secondary phases correspond to $YCO_3$ and $BaCoO_3$. After annealing in air at 900 °C no secondary phases were present.

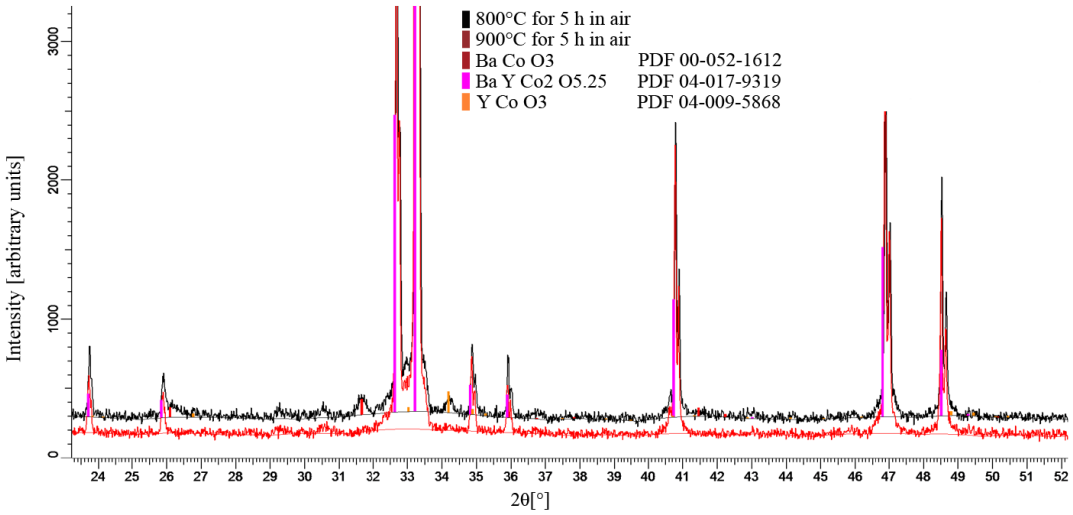


**Figure 4.16:** XRD after annealing $YBaCo_2O_{5+\delta}$ in air for five hours at 800 (black) and 900 °C (red). The lower temperature yield secondary phases. Diffraction pattern was matched to $YBaCo_2O_{5+\delta}$ (pink), $BaCoO_3$ (red) and $YCoO_3$ (orange).

## 4.5 Lattice parameters

Though the structure partly decomposed, and tetragonal and orthorhombic were both present at lower temperatures, it was possible to refine the tetragonal phase for all temperatures and atmospheres. Lattice parameters from Rietveld refinement will however not necessarily be correct outside single phase domain. In **Figure 4.18 - 4.20**, lattice parameters for orthorhombic and tetragonal phases are present also were the material is not single phase. Lattice parameters for the tetragonal single phase domain are given in **Figure 4.21**.

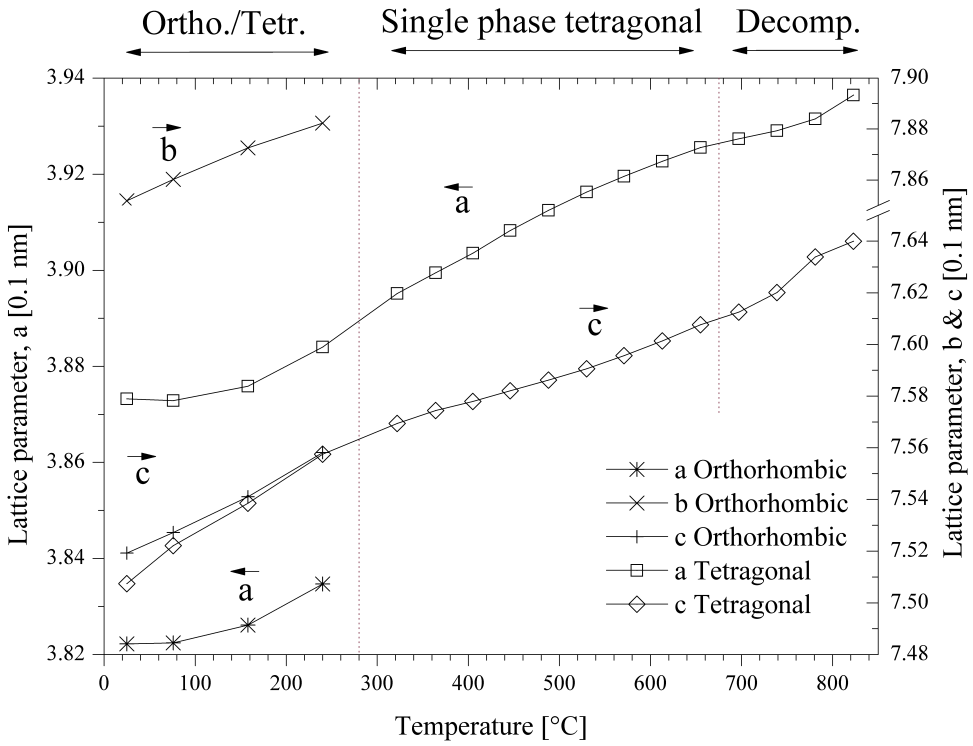


**Figure 4.17:** Lattice parameter of $YBaCo_2O_{5+\delta}$ in oxygen from Rietveld refinement (first measurement). Star, cross and plus is respectively a, b and c for orthorhombic structure. Diamond and square correspond to a and c in tetragonal cell.

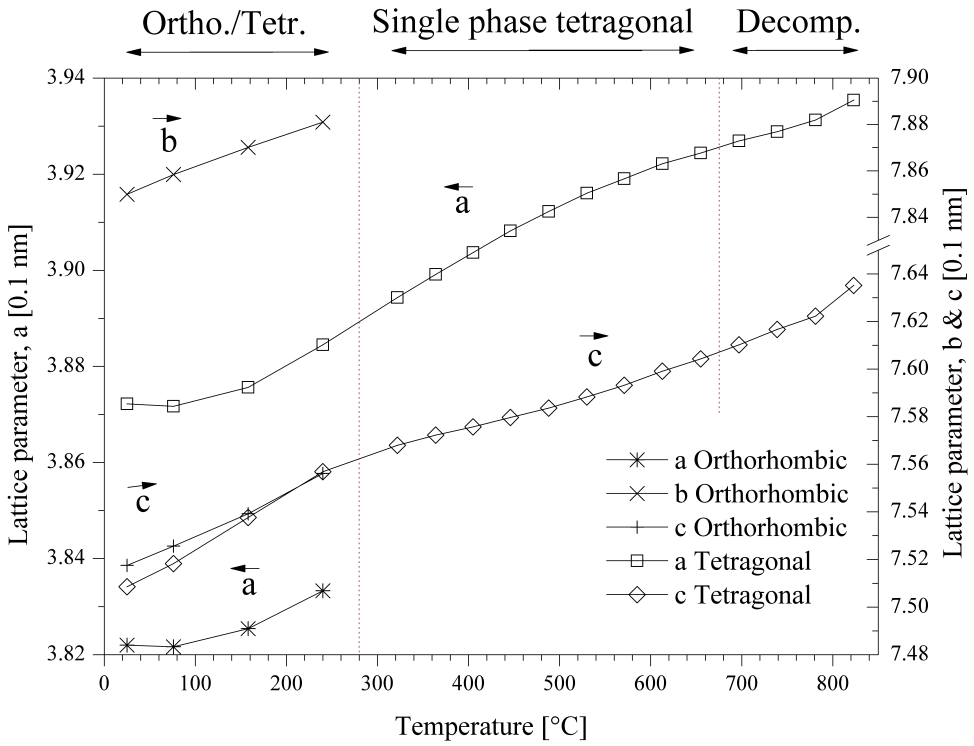


**Figure 4.18:** Lattice parameter of $YBaCo_2O_{5+\delta}$ in oxygen from Rietveld refinement (second measurement). Star, cross and plus is respectively a, b and c for orthorhombic structure. Diamond and square correspond to a and c in tetragonal cell.

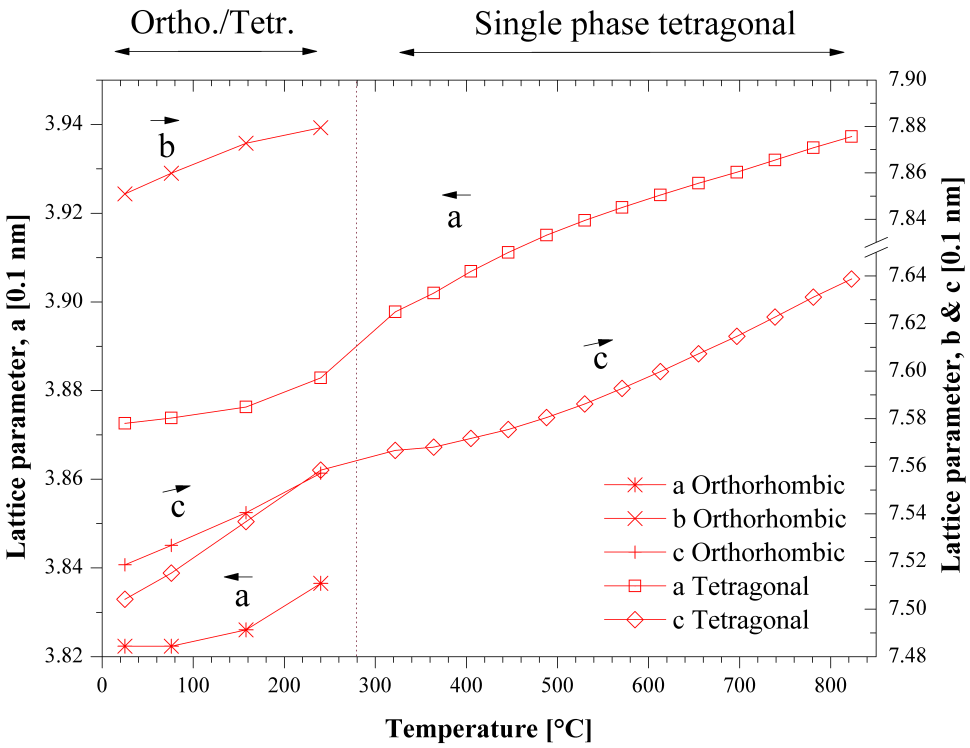


**Figure 4.19:** Lattice parameter of $YBaCo_2O_{5+\delta}$ in air from Rietveld refinement. Star, cross and plus is respectively a, b and c for orthorhombic structure. Diamond and square correspond to a and c in tetragonal cell.

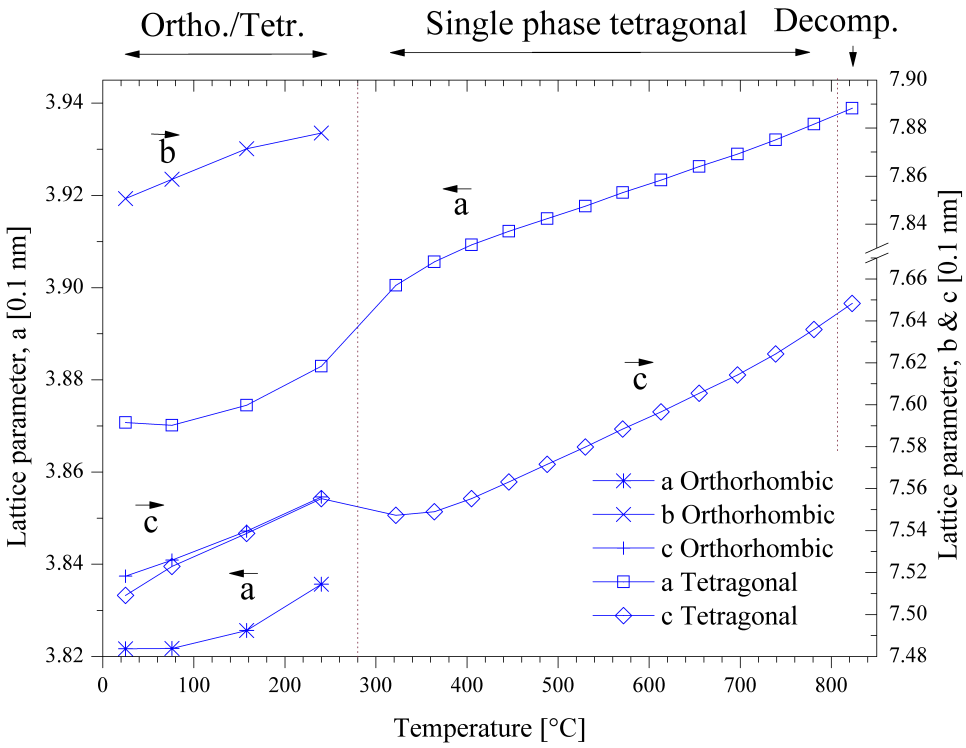


**Figure 4.20:** Lattice parameter of $YBaCo_2O_{5+\delta}$ in nitrogen from Rietveld refinement. Star, cross and plus is respectively a, b and c for orthorhombic structure. Diamond and square correspond to a and c in tetragonal cell.

## 4.6 Thermal expansion

Thermal expansion coefficients are calculated from the lattice parameters and presented in **Table 4.7**. The lines drawn in **Figure 4.21** show the slope used to calculate thermal expansion. The isotropic thermal expansion was determined to $20.0 \times 10^{-6}\,K^{-1}$ based on volume expansion, shown in **Figure 4.22**.

**Table 4.7:** Thermal expansion in a- and c-direction in tetragonal single phase region. Isotropic thermal expansion for all atmospheres was $20.0 \times 10^{-6}\,K^{-1}$

| Atmosphere | Temperature range | Thermal expansion | |
|---|---|---|---|
| | | $\frac{a-a_0}{a_0 \cdot \Delta T}$ | $\frac{c-c_0}{c_0 \cdot \Delta T}$ |
| | [°C] | $[10^{-6}\,K^{-1}]$ | $[10^{-6}\,K^{-1}]$ |
| Oxygen | 320-450 | 29.0 | 10.8 |
| | 500-650 | 18.6 | 19.2 |
| Air | 320-450 | 28.9 | 10.3 |
| | 600-800 | 15.9 | 25.3 |
| Nitrogen | 400-700 | 17.0 | 27.0 |

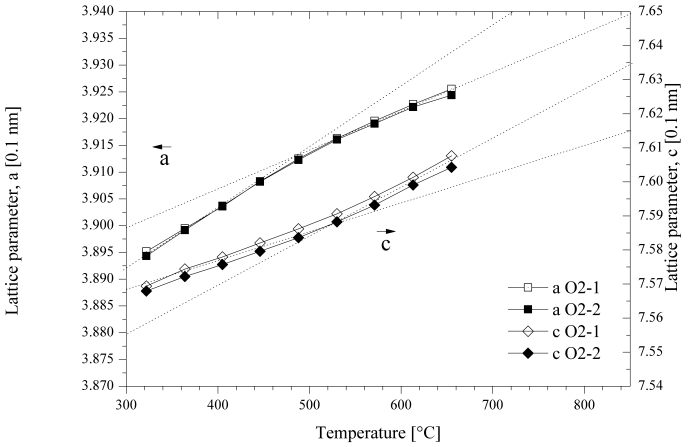


**(a)**

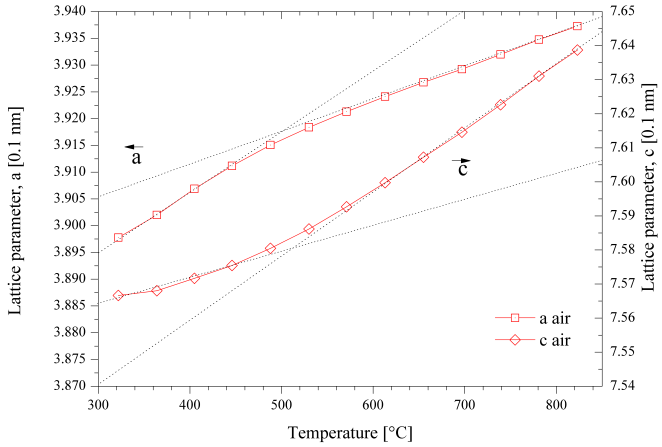


**(b)**

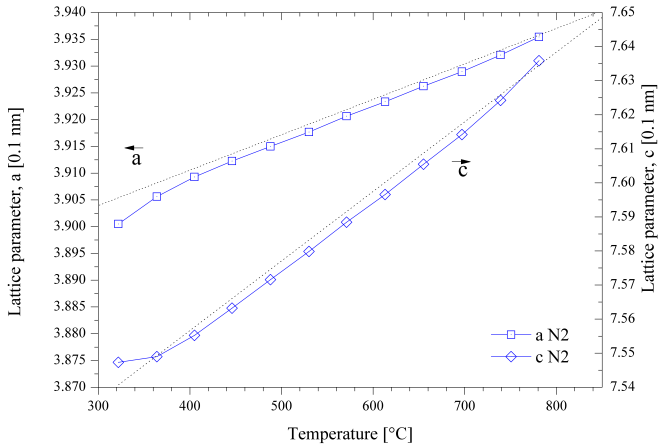


**(c)**

**Figure 4.21:** Lattice parameters in the tetragonal single phase domain. In oxygen **(a)**, air **(b)** and nitrogen **(c)**. Dotted lines show gradient used for calculating thermal expansion.

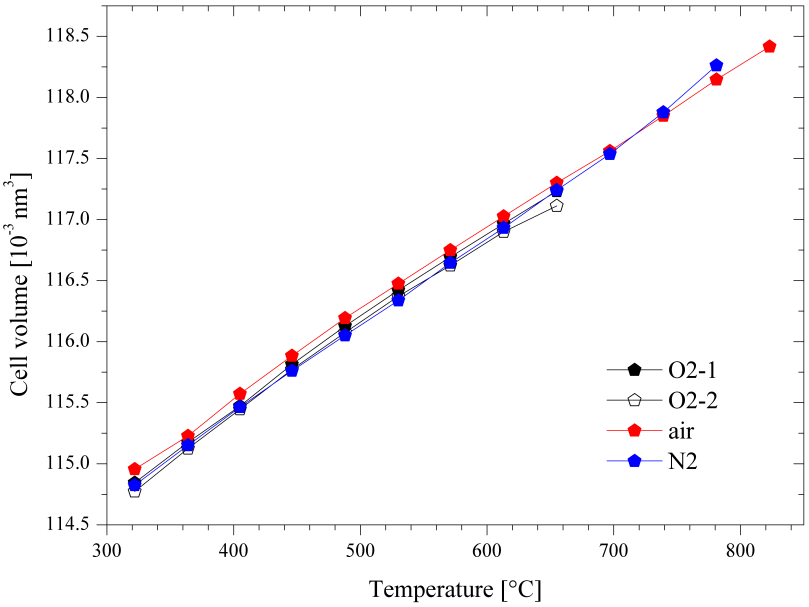


**Figure 4.22:** Unit cell volume as function of temperature for tetragonal $YBaCo_2O_{5+\delta}$ in single phase domain.

# Chapter 5

# Discussion

## 5.1 Solid state synthesis

By repeated calcination steps it was possible to obtain a phase-pure sample of $YBaCo_2O_{5+\delta}$ through solid state synthesis (SSS). Earlier trials, however, did not succeed at obtaining a phase-pure material. To obtain a phase-pure material, good mixing of the precoursors are needed as well as sufficient time and temperature for diffusion. Earlier trials did not give a phase-pure material due to several reasons. The morphology of the precursors were investigated with SEM[a], and from **Figure 5.1 (a)** it can be seen that the yttria precursor had some particles with grain size >100 µm. Diffusion lengths of a few µm in SSS makes it is impossible to make a phase-pure material with such coarse precursor without extremely energetic milling. A finer yttria precursor was therefore used, but still the phase-purity was not good enough, which was related to insufficient mixing. From an earlier batch it can be seen from EDS[b] mapping, **Figure 5.1**, that yttria agglomerates were present when using a finer precursor. The yttria agglomerate are evident by the excess of yttrium (pink) and absence of barium (yellow) and cobalt (cyan) at the lower left corner of **Figure 5.1**. By introducing ball milling to first mill yttria before ball milling it together with cobalt oxide and barium carboante, as well as increasing the calcination time to 48 h phase-purity increased. By several grinding and calcination steps phase-purity increased further.

[a] Scanning Electron Microscopy
[b] Energy-dispersive X-ray spectroscopy

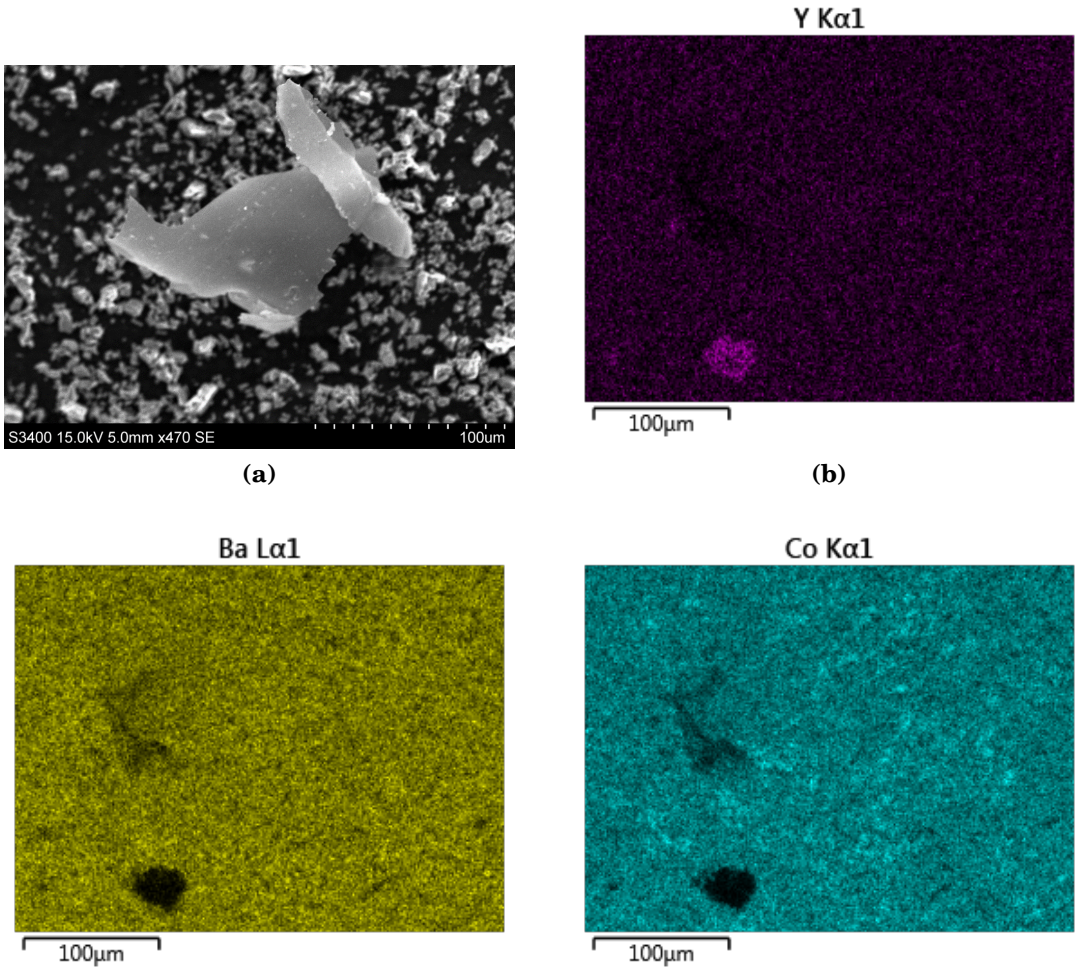


**Figure 5.1:** **(a)** SEM picture of coarse precursor yttria. **(b-d)** Element mapping by EDS of earlier failed synthesis. A more intense area can be seen for yttrium in **(b)**, while the same area is dark for both barium **(c)** and cobalt **(d)**.

## 5.2 Crystal structure

Unless annealed in oxygen, the crystal structure of $YBaCo_2O_{5+\delta}$ at room temperature is tetragonal with space group P4/mmm. The cell is doubled in c-direction (c = 7.5 Å) from A-site ordering into layers of yttrium and barium, while the a-direction (a = 3.88) is comparable to that of a single perovskite. No peaks indicating superstructures can be seen.

After annealing in oxygen the structure is orthorhombic, space group Pmmm. For annealing in oxygen the temperature was chosen to 350 °C since this showed the highest oxygen content during dynamic TGA in the fall project.[6] For this temperature the structure is tetragonal, as shown in HTXRD **Figure 4.8**. The phase transition is somewhere between 240 and 322 °C in oxygen. The orthorhombic phase was thus formed only during cooling, and to obtain a single phase orthorhombic material the annealing temperature should have been ~240 °C.

The co-existence of two phases in **Figure 4.15** after TGA measurement is logical since the cooling rate in the TGA furnace is high (500 °C/h), giving insufficient time for the tetragonal to orthorhombic phase transition.

## 5.3 Instability of $YBaCo_2O_{5+\delta}$

The instability of $YBaCo_2O_{5+\delta}$ was seen both from evolution of crystal structure as well as abrupt changes in oxygen content. The room temperature XRD measurement following the HTXRD was indexed with EVA, for all atmospheres. The phases formed are plotted in the isothermic, isobaric (T = 1100 °C, $p_{O_2}$ = 0.21) phase diagram created by Urusova et al.[7] Based on the phase diagram and diffraction patterns the decomposition reactions occurring in oxygen and nitrogen are proposed.

In **Figure 5.2** the phases present at room temperature after HTXRD in oxygen are indexed. The secondary phases present are the single perovskite $YCoO_3$ (red), [PDF 04-013-5924],[83] and $BaCoO_x$ (green) [PDF 04-010-2535].[84] The main phase is labelled as orthorhombic $Ba_2Y_2Co_4O_{11}$ (blue) [PDF 04-014-5122].[51] The fact that the structure is orthorhombic makes sense since it was cooled in oxygen, similar to the annealing in oxygen before starting HTXRD.

The three phases are indicated with the same colors in **Figure 5.3**. In high $p_{O_2}$ the double perovskite is likely unstable because it does not allow a high oxygen content, whereas the single perovskites can have higher oxygen content and thus a higher oxidation number of cobalt. The decomposition reaction is given in Equation (5.1). During HTXRD a secondary phase appeared before it disappeared again, indicating that the decomposition might be more complex. The intermediate phas(es) are likely single perovskites partially substituted by the other A-site ion.

From TGA it was seen that the oxygen content increased, before it decreased again. This indicates that the material first decomposed before it formed again at higher temperatures. The decomposition in oxidising atmosphere occurs as stated in the literature.[68,85]

$$YBaCo_2O_{5+\delta} \longrightarrow YCoO_3 + BaCoO_x \tag{5.1}$$

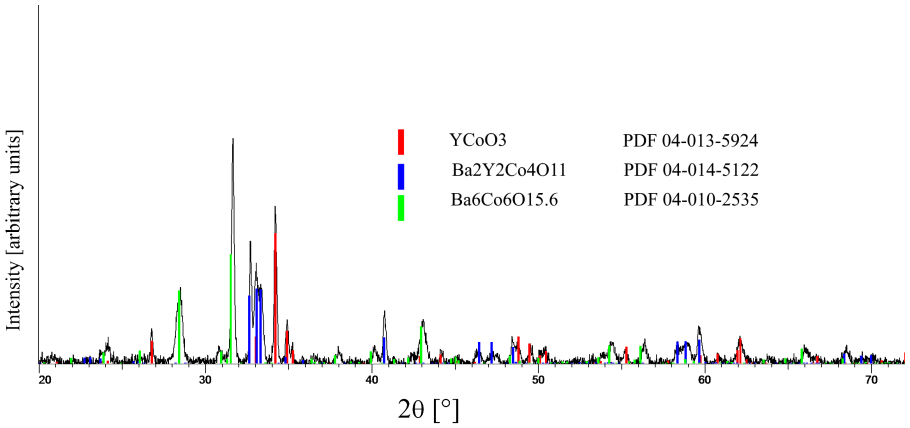


**Figure 5.2:** Room temperature measurement after HTXRD in oxygen indexed with EVA. Secondary phases $YCO_3$ and $BaCoO_{3-\delta}$ are present.

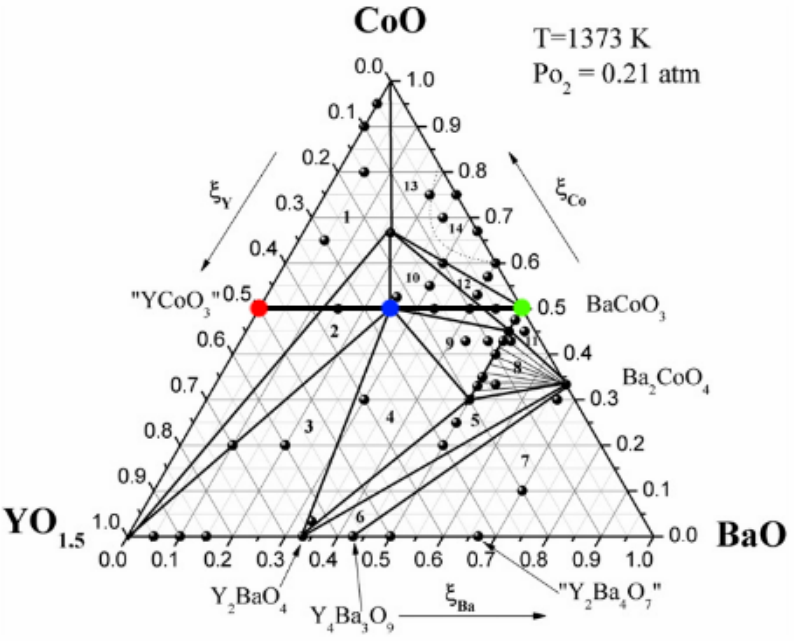


**Figure 5.3:** Phase diagram from Urusova et al.[7] with phases in decomposition reaction in oxygen highlighted.

In room temperature in nitrogen the diffractogram show primarily tetragonal $YBaCo_2O_{5+\delta}$ (red) [PDF 04-017-9319],[79] but also Y2O3 (blue and brown) [PDF 00-043-1036], $BaYCo_4O_7$ (green) [PDF 04-012-7224][86] and $BaCo_{0.75}Y_{0.25}O_{2.55}$(pink) [PDF 00-057-0194].[87] The decomposition can barely be seen at the maximum temperature scan, shown in **Figure 4.11**, which indicates that the decomposition is rather slow at these temperatures. In oxygen the drop corresponding to a decomposition is first seen at 1000 °C. Based upon the XRD results, shown in **Figure 5.4**, the decomposition reaction is proposed as shown in Equation (5.2). When a quaternary oxide decomposes ternary oxides are normally formed, and not binary oxides. Despite this fact, it seems probable from the phase diagram that yttria is formed. As stated by Zhang et al. $YBaCo_2O_{5+\delta}$ decomposes in reducing atmosphere.[85]

$$YBaCo_2O_{5+\delta} \longrightarrow Y_2O_3 + BaYCo_4O_7 + BaCo_{0.75}Y_{0.25}O_{2.55} \tag{5.2}$$

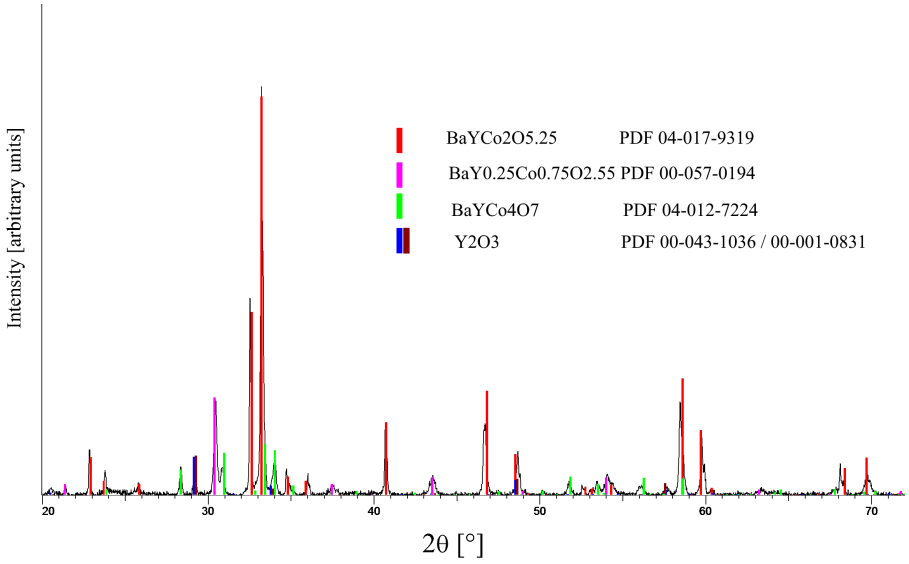


**Figure 5.4:** Room temperature measurement after HTXRD in nitrogen indexed with EVA. Secondary phases $BaYCo_4O_7$, $BaCo_{0.75}Y_{0.25}O_{2.55}$ and $Y_2O_3$ are present.

During HTXRD in air, secondary phases were not seen in the diffraction pattern. During annealing at 800 °C in air the single perovskites were formed, **Figure 4.16**, this shows that the apparent stability in air was only due to kinetics. After annealing at 900 °C no secondary peaks were seen. This fits well with the fact that $YBaCo_2O_{5+\delta}$ decomposition reaction is reversed in oxygen at higher temperatures (925 °C). Further, during TGA in air a small decrease/bump in oxygen content seen in **Figure 4.13** indicating that a fraction of $YBaCo_2O_{5+\delta}$ decomposed before $YBaCo_2O_{5+\delta}$ was formed again.

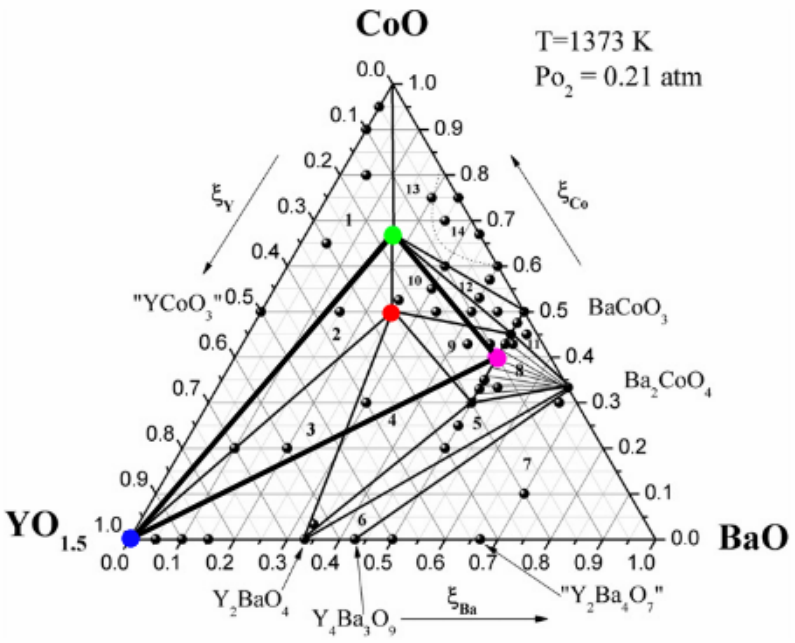


**Figure 5.5:** Phase diagram from Urusova et al.[7] with phases in decomposition reaction in nitrogen highlighted.

## 5.4 Oxygen content and thermogravimetry

The oxygen stoichiometry after oxidation, $5+\delta$ = 5.42, are similar to literature values. Hao et al. report $5+\delta$ = 5.46,[88] Urusova et al. report $5+\delta$ = 5.41,[54] Akahoshi and Yueda report $5+\delta$ between 0 and 5.52.[53] In this work oxygen content was found to stabilise below 5.0, this is probably only due to measurement error or uncertainty, since $5+\delta$ correspond to totally depleted yttrium layer. The TGA experiment was repeated, **Figure 4.13**, to hopefully remove the illogical oxidation in nitrogen and stabilisation of oxygen content below 5.0. However, both were reproduced, indicating systematic errors.

The anomaly could originate in a difference between the measurement and the subtracted background, for instance due to a difference in flow. Though a difference in flow can cause a weight change, this is usually only transient while the pressure change occurs, and the increased mass observed in nitrogen occurred for several hours. Also the measurements were conducted with different background measurements so it is not likely that the difference between background caused the apparent weight gain.

Both experiments in nitrogen (blue) and the last measurement in air (red, filled symbols) show increase in mass from the first data point to the second (the first data point after drying the compound). Comparing the two air measurements both stabilises and are rather constant from 700 to 1100 °C, however, at two different plateaus. Assuming the starting point is incorrect for the filled symbols the difference between the plateaus would decrease. Also for the nitrogen measurements the zero point is likely to be incorrect, since they follow the same trend as air initially. With an incorrect starting point the variation in oxygen content is also incorrect since the oxygen content is related to the ratio between initial and final mass. If

time allowed it recalculating the oxygen content based on the first data point after drying would lead to more expected values. Though care was taken to allow the scale to stabilise before the measurement began part of the apparent oxidation can be simply be related to a incorrect zero point. If the pressure was lower just after evacuating and venting the chamber compared with the rest of the measurement it could cause an incorrect zero point. Though drying can have minor effects of the actual oxygen content, it would be better to use the mass after drying as initial mass when calculating oxygen content. This would have removed a lot of the anomaly in the oxygen content.

The oxygen content should have been highest for oxygen atmosphere, and the lowest in nitrogen atmosphere. The oxygen content stabilises in all atmospheres indicating a threshold is reached, this threshold oxygen content is likely 5.0. In nitrogen measurement oxygen content drop close to 1100 °C due to decomposition evident from regular XRD after TGA as well as HTXRD. In the measurement conducted in oxygen the oxygen content peaks due to another decomposition reaction, which was also seen in HTXRD.

## 5.5 Chemical and thermal expansion

**Figure 5.6** shows lattice parameters of single phase tetragonal $YBaCo_2O_{5+\delta}$. Both a- and c-parameter increase with temperature due to thermal expansion, but for a-parameter the increase in lattice parameter decrease as temperature increases, while the opposite is observed for the c-parameter. With decreasing $p_{O_2}$ the a-parameter increases while c-parameter decreases. An explanation for this can be as follows: the oxygen vacancies are located in the yttrium layer.[3,40,42–45] Creating more vacancies makes the ab-plane expand since the positive charges repel each other. This is compensated by a decrease in c-parameter. At higher temperatures the cell parameter is similar for all atmospheres, which is logical since weight loss stabilised in TGA measurement. In **Figure 4.22** the slope is constant implying that the variation in a- and c-direction cancel each other out. The last point before decomposition, both in oxygen and nitrogen, deviates from linearity. This is likely due to the presence of decomposition products which are present in trace quantity so that their diffraction pattern cannot be seen, but still they can effect the lattice of the main phase.

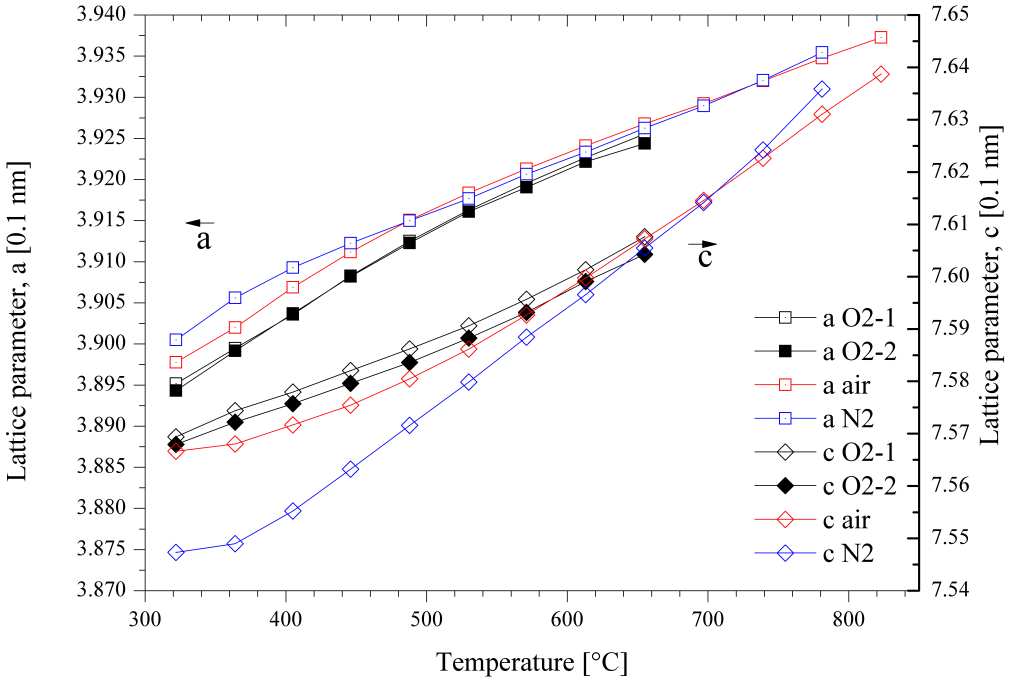


**Figure 5.6:** Lattice parameter in oxygen, air and nitrogen as function of temperature in the tetragonal single phase domain.

Thermal expansion is anisotropic with TEC from 10 to $29 \times 10^{-6}\,K^{-1}$, with isotropic TEC of $20.0 \times 10^{-6}\,K^{-1}$. A low TEC is advantageous to match thermal expansion coefficient of electrolyte (BCZY = 10.2–$12.5 \times 10^{-6}\,K^{-1}$,[70] YSZ, GDC, GSM = 10.0–$12.5 \times 10^{-6}\,K^{-1}$[15]). The calcualted TEC is low for a cobaltite and is related to the low ionicity of Y-O bond compared to other lanthanides.[5,67–69] For the same compound average TEC down to 14.5/14.9 has been reported.[54/69]

The chemical expansion can be seen from **Figure 5.6**. At 600 °C the lattice parameters show little dependence on atmosphere, and from TGA it can be seen that oxygen content has stabilised at this temperature. At lower temperatures the oxygen content is significantly lower in nitrogen. The cell parameter a is increased for lower oxygen content, while the c parameter is decreased. Due to the uncertainty the chemical expansion is only calculated between oxygen and nitrogen at 400 °C where the difference is large. Chemical expansion can be calculated from Equation (5.3) and (5.4) which gives $\frac{\epsilon_a}{\Delta\delta}$ = -0.072 and $\frac{\epsilon_c}{\Delta\delta}$ = 0.015.

$$\frac{\epsilon_a}{\Delta(5+\delta)} = \frac{\frac{a_{N_2} - a_{O_2}}{a_{O_2}}}{(5+\delta_{N_2}) - (5+\delta_{O_2})} \tag{5.3}$$

$$\frac{\epsilon_c}{\Delta(5+\delta)} = \frac{\frac{c_{N_2} - c_{O_2}}{c_{O_2}}}{(5+\delta_{N_2}) - (5+\delta_{O_2})} \tag{5.4}$$

## 5.6 Ionic conductivity

$YBaCo_2O_{5+\delta}$ shows a cation ordered, oxygen disordered structure from 400 °C to 800 °C. This is advantageous because the disordered vacancies are more free to move than the ordered structure where most of the positions are not mobile, but either occupied or not. At 400 °C the oxygen content in air and oxygen is about 5.2. If all the vacancies are located in the yttrium layer, $YO_\delta$, ~20 % of yttrium is octahedral coordinated, while the rest is pyramidal. This gives the oxygen many possibilities to adjacent pyramidal positions to jump to. If the temperature is above 600 °C the oxygen content is close to 5.0, and if the whole $YO_\delta$ plane is depleted for oxygen no oxygen is present to be conducted within this layer. It could be that oxygen from other positions could contribute to conduction, but from literature the vacancies are stated to be located only within the yttrium layer.[3,45]

Vacancies are needed two hydrate layered double perovskite, and $YBaCo_2O_{5+\delta}$ has many vacancies. For each vacancy to hydroxides are formed. However, the degree of hydration might not be that high since the structure could only occupy half of the oxygen positions in the $YO_\delta$ layer. Complete hydration of the lanthanide layer is reported to only be possible for structures with tolerance factor close to unity,[32,36] and yttrium is a small atom giving a low tolerance factor.

# Chapter 6

# Conclusion

$YBaCo_2O_{5+\delta}$ was synthesised through solid state synthesis and characterised. Its crystal structure was determined at ambient conditions and at high temperatures in oxygen, air and nitrogen. The structure is orthorhombic at room temperature if annealed in oxygen. The space group is Pmmm with a = 3.82, b = 7.86 and c =7.52, indicating a doubling of both b- and c-parameter. If not annealed in oxygen, the structure is tetragonal P4/mmm with a = 3.88 and c = 7.50. At higher temperature, above 320 °C, the structure is tetragonal in all atmospheres. The isotropic thermal expansion is $20.0 \times 10^{-6}\,\mathrm{K}^{-1}$.

The absolute oxygen content was determined to 5.42 ± 0.02 by ex situ TGA by reduction to cobalt and binary oxides. The relative oxygen content was determined with in situ TGA in oxygen, air and nitrogen.

Decomposition occurs in both oxygen, according to Equation (6.1), and in nitrogen, according to Equation (6.2). In air decomposition also occur, according to Equation (6.1), but at a slower rate. The instability of the material makes it inapplicable as material for high and intermediate temperature use, such as SOFC. Though the material seemed stable at intermediate temperature, it is only a question of kinetics when it will decompose.

$$YBaCo_2O_{5+\delta} + \mathrm{O_2} \longrightarrow YCoO_3 + BaCo_{3-\delta} \tag{6.1}$$

$$YBaCo_2O_{5+\delta} \longrightarrow \mathrm{YBaCo_4O_7} + \mathrm{Y_2O_3} + \mathrm{BaCo_xY_{1-x}O_{3-\delta}} + \mathrm{O_2} \tag{6.2}$$

Similar compounds with larger Ln, especially Ln = Pr are reported to have superior properties and are even reported to posses proton conductivity.[75] Investigation of similar compounds might lead to the discovery of cathode material with superior performance at intermediate temperature. For stable layered double perovskites

dillatommetry, conductivity as well as impedance spectroscopy to determine area specific resistance

# Bibliography


[1] J. Pan, "Defects and Transport in $RE_2WO_6$," Master's thesis, Centre for Materials Science and Nanotechnology, Department of Chemistry, University of Oslo, 2012.

[2] W. Zhou, "Solid Solution of $YBaCu_xCo_{2-x}O_5$ ($0 \leq x \leq 1$) and Its Intergrowth with $YBa_2Cu_3O_7$," *Chemistry of materials: a publication of the American Chemical Society*, vol. 6, pp. 441–447, Apr. 1994.

[3] A. Maignan, C. Martin, D. Pelloquin, N. Nguyen, and B. Raveau, "Structural and Magnetic Studies of Ordered Oxygen-Deficient Perovskites $LnBaCo_2O_{5+\delta}$ , Closely Related to the " 112 " Structure," *Journal of solid state chemistry*, vol. 142, pp. 247–260, Feb. 1999.

[4] A. McKinlay, P. Connor, J. T. S. Irvine, and W. Zhou, "Structural Chemistry and Conductivity of a Solid Solution of $YBa_{1-x}Sr_xCo_2O_{5+\delta}$," *Journal of Physical Chemistry C*, vol. 111, pp. 19120–19125, Dec. 2007.

[5] A. Manthiram, J.-H. Kim, Y. N. Kim, and K.-T. Lee, "Crystal chemistry and properties of mixed ionic-electronic conductors," *Journal of Electroceramics*, vol. 27, pp. 93–107, 24 Feb. 2011.

[6] S. L. Jørgensen, T. Grande, and C. Bernuy-Lopez, "Synthesis and properties of $YBaCo_2O_{5+\delta}$ for solid oxide fuel cell cathodes," 2015.

[7] A. S. Urusova, V. A. Cherepanov, T. V. Aksenova, L. Y. Gavrilova, and E. A. Kiselev, "Phase equilibria, crystal structure and oxygen content of intermediate phases in the Y–Ba–Co–O system," *Journal of solid state chemistry*, vol. 202, pp. 207–214, June 2013.

[8] C. Azar and K. Lindgren, "Energiläget år 2050," 2000.

[9] E. Fabbri, L. Bi, D. Pergolesi, and E. Traversa, "Towards the next generation of solid oxide fuel cells operating below 600 °C with chemically stable proton-conducting electrolytes," *Advanced materials*, vol. 24, pp. 195–208, 10 Jan. 2012.

[10] J.-H. Kim and A. Manthiram, "Layered $LnBaCo_2O_{5+\delta}$ perovskite cathodes for solid oxide fuel cells: an overview and perspective," *Journal of materials chemistry. A, Materials for energy and sustainability*, vol. 3, no. 48, pp. 24195–24210, 2015.

[11] F. T. Bacon, "Fuel cells, past, present and future," *Electrochimica acta*, vol. 14, pp. 569–585, 1 July 1969.

[12] FuelCellToday
, "History." http://www.fuelcelltoday.com/history\.

[13] A. Tarancón, "Strategies for lowering solid oxide fuel cells operating temperature," *Energies*, vol. 2, pp. 1130–1150, 25 Nov. 2009.

[14] E. Fabbri, D. Pergolesi, and E. Traversa, "Electrode materials: a challenge for the exploitation of protonic solid oxide fuel cells," *Science and Technology of Advanced Materials*, vol. 11, no. 4, p. 044301, 2010.

[15] D. J. L. Brett, A. Atkinson, N. P. Brandon, and S. J. Skinner, "Intermediate temperature solid oxide fuel cells," *Chemical Society reviews*, vol. 37, pp. 1568–1578, Aug. 2008.

[16] C. Duan, J. Tong, M. Shang, S. Nikodemski, M. Sanders, S. Ricote, A. Almansoori, and R. OHayre, "Readily processed protonic ceramic fuel cells with high performance at low temperatures," *Science*, vol. 349, pp. 1321–1326, 18 Sept. 2015.

[17] F. Zakaria, "K.R. Sridhar: Bloom Energy's Fuel-Cell Guru
." http://www.newsweek.com/kr-sridhar-bloom-energys-fuel-cell-guru-70571/ [Online; accessed 05-May-2016], 2010.

[18] B. C. Steele and A. Heinzel, "Materials for fuel-cell technologies," *Nature*, vol. 414, pp. 345–352, 15 Nov. 2001.

[19] D. Fu, F. Jin, and T. He, "A-site calcium-doped $Pr_{1-x}Ca_xBaCo_2O_{5+\delta}$ double perovskites as cathodes for intermediate-temperature solid oxide fuel cells," *Journal of power sources*, vol. 313, pp. 134–141, May 2016.

[20] A. J. Jacobson, "Materials for Solid Oxide Fuel Cells," *Chemistry of materials: a publication of the American Chemical Society*, vol. 22, no. 3, pp. 660–674, 2010.

[21] F. Meng, T. Xia, J. Wang, Z. Shi, J. Lian, H. Zhao, J.-M. Bassat, and J.-C. Grenier, "Evaluation of layered perovskites $YBa_{1-x}Sr_xCo_2O_{5+\delta}$ as cathodes for intermediate-temperature solid oxide fuel cells," *International journal of hydrogen energy*, vol. 39, pp. 4531–4543, Mar. 2014.

[22] L. Blum, L. G. J. de Haart, J. Malzbender, N. Margaritis, and N. H. Menzler, "Anode-Supported Solid Oxide Fuel Cell Achieves 70 000 Hours of Continuous Operation," *Energy Technology*, 1 May 2016.

[23] T. C. I. C. o. C. f. E. Materials, "World Record: Jülich fuel cell runs for more than 70,000 hours." Retrieved 09.06.2016. http://www.2011-ichem.com/en/shownews.asp?classid=69&ca=6&id=1535, 2016.

[24] Ceramics.org, "Jülich ceramic fuel cell sets world record with 70,000 hours of continuous service." Retrieved 09.06.2016.0 http://ceramics.org/ceramic-tech-today/julich-ceramic-fuel-cell-sets-world-record-with-70000-hours-of-continuous-service, 2015.

[25] M. Mogensen, D. Lybye, N. Bonanos, P. V. Hendriksen, and F. W. Poulsen, "Factors controlling the oxide ion conductivity of fluorite and perovskite structured oxides," *Solid State Ionics*, vol. 174, pp. 279–286, 29 Oct. 2004.

[26] G. Goupil, T. Delahaye, G. Gauthier, B. Sala, and F. L. Joud, "Stability study of possible air electrode materials for proton conducting electrochemical cells," *Solid State Ionics*, vol. 209–210, pp. 36–42, 23 Feb. 2012.

[27] H. Iwahara, "Proceedings of the 10th International Conference on Solid State IonicsProton conducting ceramics and their applications," *Solid State Ionics*, vol. 86, pp. 9–15, 1 July 1996.

[28] L. Yang, Z. Liu, S. Wang, Y. Choi, C. Zuo, and M. Liu, "A mixed proton, oxygen ion, and electron conducting cathode for SOFCs based on oxide proton conductors," *Journal of power sources*, vol. 195, pp. 471–474, 15 Jan. 2010.

[29] A. Grimaud, F. Mauvy, J. M. Bassat, S. Fourcade, L. Rocheron, M. Marrony, and J. C. Grenier, "Hydration Properties and Rate Determining Steps of the Oxygen Reduction Reaction of Perovskite-Related Oxides as $H^+$-SOFC Cathodes," *Journal of the Electrochemical Society*, vol. 159, pp. B683–B694, 1 Jan. 2012.

[30] D. Poetzsch, R. Merkle, and J. Maier, "Proton conductivity in mixed-conducting BSFZ perovskite from thermogravimetric relaxation," *Physical chemistry chemical physics: PCCP*, vol. 16, pp. 16446–16453, 16 June 2014.

[31] L. Fan and P.-C. Su, "Layer-structured $LiNi_{0.8}Co_{0.2}O_2$: A new triple ($H^+/O^{2-}/e^-$) conducting cathode for low temperature proton conducting solid oxide fuel cells," *Journal of power sources*, vol. 306, pp. 369–377, Feb. 2016.

[32] E. Fabbri, D. Pergolesi, and E. Traversa, "Materials challenges toward proton-conducting oxide fuel cells: a critical review," *Chemical Society reviews*, vol. 39, pp. 4355–4369, Nov. 2010.

[33] S. Liu, K. T. Chuang, and J.-L. Luo, "Double-Layered Perovskite Anode with in Situ Exsolution of a Co–Fe Alloy To Cogenerate Ethylene and Electricity in a Proton-Conducting Ethane Fuel Cell," *ACS catalysis*, vol. 6, pp. 760–768, 5 Feb. 2016.

[34] A. K. Kundu and B. Raveau, "Structural, Magnetic and Electron Transport Properties of Ordered-Disordered Perovskite Cobaltites," pp. 1–37, 29 May 2010.

[35] J. Mizusaki, "Oxygen nonstoichiometry and defect equilibrium in the perovskite-type oxides $La_{1-x}Sr_xMnO_{3+d}$," *Solid State Ionics*, vol. 129, pp. 163–177, Apr. 2000.

[36] K. D. Kreuer, "Proton-Conducting Oxides," *Annual review of materials research*, vol. 33, no. 1, pp. 333–359, 2003.

[37] A. K. Eriksson Andersson, S. M. Selbach, T. Grande, and C. S. Knee, "Thermal evolution of the crystal structure of proton conducting $BaCe_{0.8}Y_{0.2}O_{3-\delta}$ from high-resolution neutron diffraction in dry and humid atmosphere," *Dalton transactions*, vol. 44, pp. 10834–10846, 21 June 2015.

[38] R. Pelosato, A. Donazzi, G. Dotelli, C. Cristiani, I. Natali Sora, and M. Mariani, "Electrical characterization of co-precipitated $LaBaCo_2O_{5+\delta}$ and $YBaCo_2O_{5+\delta}$ oxides," *Journal of the European Ceramic Society*, vol. 34, pp. 4257–4272, Dec. 2014.

[39] G. King and P. M. Woodward, "Cation ordering in perovskites," *Journal of materials chemistry*, vol. 20, pp. 5785–5796, 15 Apr. 2010.

[40] G. Aurelio, J. Curiale, R. D. Sanchez, and G. J. Cuello, "Probing phase coexistence and stabilization of the spin-ordered ferrimagnetic state by Calcium addition in the $YBa_{1-x}Ca_xCo_2O_{5.5}$ layered cobaltites using neutron diffraction," 19 Nov. 2007.

[41] G. Aurelio, J. Curiale, R. D. Sánchez, and G. J. Cuello, "Enhancing spin state phase separation by strontium addition in the $YBa_{1-x}Sr_xCo_2O_{5.5}$ layered cobaltite," *Journal of physics. Condensed matter: an Institute of Physics journal*, vol. 21, p. 326002, 12 Aug. 2009.

[42] D. Khalyavin, A. Balagurov, A. Beskrovnyi, I. Troyanchuk, A. Sazonov, E. Tsipis, and V. Kharton, "Neutron powder diffraction study of $TbBaCo_{2-x}$ $Fe_xO_{5+\gamma}$ layered oxides," vol. 177, no. 6, pp. 2068–2072, 2004.

[43] N. Ishizawa, T. Asaka, T. Kudo, K. Fukuda, A. Yasuhara, N. Abe, and T.-H. Arima, "Structural Evolution of $GdBaCo_2O_{5+\delta}$ ($\delta$ = 7/18) at Elevated Temperatures," *Chemistry of materials: a publication of the American Chemical Society*, vol. 26, no. 22, pp. 6503–6517, 2014.

[44] Z. Qin, H. Song, F. Gao, J. Jia, D. Yang, and X. Hu, "Influence of $R^{3+}$ Ion Sizes on the Transport Properties of $RBaCo_2O_{5+\delta}$ Ceramics," *International Journal of Applied Ceramic Technology*, vol. 10, pp. E145–E150, 1 Sept. 2013.

[45] R. A. Cox-Galhotra, A. Huq, J. P. Hodges, J.-H. Kim, C. Yu, X. Wang, A. J. Jacobson, and S. McIntosh, "Visualizing oxygen anion transport pathways in $NdBaCo2O_{5+\delta}$ by in situ neutron diffraction," *Journal of materials chemistry. A, Materials for energy and sustainability*, vol. 1, pp. 3091–3100, 14 Jan. 2013.

[46] F. Millange, E. Suard, V. Caignaert, and B. Raveau, "$YBaMn_2O_5$: crystal and magnetic structure reinvestigation," *Materials research bulletin*, vol. 34, pp. 1–9, 1 Jan. 1999.

[47] V. Bobrovskii, V. Kazantsev, A. Mirmelstein, N. Mushnikov, N. Proskurnina, V. Voronin, E. Pomjakushina, K. Conder, and A. Podlesnyak, "Spontaneous and field-induced magnetic transitions in $YBaCo_2O_{5.5}$," *Journal of magnetism and magnetic materials*, vol. 321, no. 5, pp. 429–437, 2009.

[48] D. P. Kozlenko, Z. Jirák, N. O. Golosova, and B. N. Savenko, "Magnetic ground state and the spin-state transitions in YBaCo2O5.5," *The European physical journal. B*, vol. 70, pp. 327–334, 3 July 2009.

[49] D. Akahoshi and Y. Ueda, "Magnetic and M-I Transitions in $YBaCo_2O_{5+x}$ ($0 \leq x \leq 0.5$)," *Journal of the Physical Society of Japan*, vol. 68, no. 3, pp. 736–739, 1999.

[50] J. Zou, J. Park, B. Kwak, H. Yoon, and J. Chung, "Effect of Fe doping on $PrBaCo_2O_{5+\delta}$ as cathode for intermediate-temperature solid oxide fuel cells," *Solid State Ionics*, vol. 206, pp. 112–119, 5 Jan. 2012.

[51] D. D. Khalyavin, D. N. Argyriou, U. Amann, A. A. Yaremchenko, and V. V. Kharton, "Spin-state ordering and magnetic structures in the cobaltites $ybaco_2o_{5+\delta}$ ( $\delta$ = 0.50 and 0.44)," *Phys. Rev. B Physical Review B*, vol. 75, Sep 2007.

[52] T. V. Aksenova, L. Ya. Gavrilova, D. S. Tsvetkov, V. I. Voronin, and V. A. Cherepanov, "Crystal structure and physicochemical properties of layered

perovskite-like phases $LnBaCo_2O_{5+\delta}$," *Russian Journal of Physical Chemistry*, vol. 85, pp. 427–432, 5 Feb. 2011.

[53] D. Akahoshi and Y. Ueda, "Oxygen Nonstoichiometry, Structures, and Physical Properties of $YBaCo_2O_{5+x}$ ($0.00 \leq x \leq 0.52$)," *Journal of solid state chemistry*, vol. 156, pp. 355–363, Feb. 2001.

[54] A. S. Urusova, V. A. Cherepanov, O. I. Lebedev, T. V. Aksenova, L. Y. Gavrilova, V. Caignaert, and B. Raveau, "Tuning oxygen content and distribution by substitution at Co site in 112 $YBaCo_2O_{5+\delta}$: impact on transport and thermal expansion properties," *Journal of materials chemistry. A, Materials for energy and sustainability*, vol. 2, no. 23, p. 8823, 2014.

[55] B. Raveau, M. D. Motin Seikh, V. Pralong, and V. Caignaert, "Ordered oxygen deficient '112' perovskites, $LnBaCo_2O_{5.50+\delta}$ : complex magnetism and transport properties," *Bulletin of Materials Science*, vol. 32, pp. 305–312, 15 Aug. 2009.

[56] S. J. Skinner, "Recent advances in Perovskite-type materials for solid oxide fuel cell cathodes," *International Journal of Inorganic Materials*, vol. 3, no. 2, pp. 113–121, 2001.

[57] S. P. Jiang, *Development of lanthanum strontium manganite perovskite cathode materials of solid oxide fuel cells: A review*, vol. 43. 2008.

[58] O. L. Pineda, Z. L. Moreno, P. Roussel, K. Świerczek, and G. H. Gauthier, "Synthesis and preliminary study of the double perovskite $NdBaCo_2O_{5+\delta}$ as symmetric SOFC electrode material," *Solid State Ionics*, vol. 288, pp. 61–67, 2016.

[59] K. Zhang, L. Ge, R. Ran, Z. Shao, and S. Liu, "Synthesis, characterization and evaluation of cation-ordered $LnBaCo_2O_{5+\delta}$ as materials of oxygen permeation membranes and cathodes of SOFCs," *Acta materialia*, vol. 56, pp. 4876–4889, Oct. 2008.

[60] Y. Zhang, B. Yu, S. Lü, X. Meng, X. Zhao, Y. Ji, Y. Wang, C. Fu, X. Liu, X. Li, Y. Sui, J. Lang, and J. Yang, "Effect of Cu doping on $YBaCo_2O_{5+\delta}$ as cathode for intermediate-temperature solid oxide fuel cells," *Electrochimica acta*, vol. 134, pp. 107–115, July 2014.

[61] X. Zhang, H. Hao, Q. He, and X. Hu, "High-temperature electronic transport properties of Fe-doped $YBaCo_2O_{5+\delta}$," *Physica. B, Condensed matter*, vol. 394, pp. 118–121, May 2007.

[62] D. Chen, F. Wang, H. Shi, R. Ran, and Z. Shao, "Systematic evaluation of Co-free $LnBaFe_2O_{5+\delta}$(Ln= Lanthanides or Y) oxides towards the application as cathodes for intermediate-temperature solid oxide fuel cells," *Electrochimica acta*, vol. 78, pp. 466–474, 2012.

[63] T. Broux, M. Bahout, J. M. Hanlon, O. Hernandez, S. Paofai, A. Berenov, and S. J. Skinner, "High temperature structural stability, electrical properties and chemical reactivity of $NdBaCo_{2-x}Mn_xO_{5+\delta}$ ($0 \leq x \leq 2$) for use as cathodes in solid oxide fuel cells," *Journal of materials chemistry. A, Materials for energy and sustainability*, vol. 2, no. 40, pp. 17015–17023, 2014.

[64] A. Tarancón, M. Burriel, J. Santiso, S. J. Skinner, and J. A. Kilner, "Advances in layered oxide cathodes for intermediate temperature solid oxide fuel cells," *Journal of materials chemistry*, vol. 20, no. 19, p. 3799, 2010.

[65] J.-H. Kim, L. Mogni, F. Prado, A. Caneiro, J. A. Alonso, and A. Manthiram, "High Temperature Crystal Chemistry and Oxygen Permeation Properties of the Mixed Ionic–Electronic Conductors $LnBaCo_2O_{5+\delta}$ (Ln=Lanthanide)," *Journal of the Electrochemical Society*, vol. 156, no. 12, p. B1376, 2009.

[66] R. Pelosato, G. Cordaro, D. Stucchi, C. Cristiani, and G. Dotelli, "Cobalt based layered perovskites as cathode material for intermediate temperature Solid Oxide Fuel Cells: A brief review," *Journal of power sources*, vol. 298, pp. 46–67, 1 Dec. 2015.

[67] D. Chen, F. Wang, H. Shi, R. Ran, and Z. Shao, "Systematic evaluation of Co-free $LnBaFe_2O_{5+\delta}$ (Ln=Lanthanides or Y) oxides towards the application as cathodes for intermediate-temperature solid oxide fuel cells," *Electrochimica acta*, vol. 78, pp. 466–474, Sept. 2012.

[68] J.-H. Kim, Y. N. Kim, Z. Bi, A. Manthiram, M. P. Paranthaman, and A. Huq, "Overcoming phase instability of $RBaCo_2O_{5+\delta}$ (R = Y and Ho) by Sr substitution for application as cathodes in solid oxide fuel cells," *Solid State Ionics*, vol. 253, pp. 81–87, 15 Dec. 2013.

[69] J.-H. Kim and A. Manthiram, "$LnBaCo_2O_{5+\delta}$ Oxides as Cathodes for Intermediate-Temperature Solid Oxide Fuel Cells," *Journal of the Electrochemical Society*, vol. 155, no. 4, p. B385, 2008.

[70] D. Medvedev, J. Lyagaeva, G. Vdovin, S. Beresnev, A. Demin, and P. Tsiakaras, "A tape calendering method as an effective way for the preparation of proton ceramic fuel cells with enhanced performance," *Electrochimica acta*, vol. 210, pp. 681–688, 20 Aug. 2016.

[71] C. Bernuy-Lopez, K. Høydalsvik, M.-A. Einarsrud, and T. Grande, "Effect of A-Site Cation Ordering on Chemical Stability, Oxygen Stoichiometry and Electrical Conductivity in Layered $LaBaCo_2O_{5+\delta}$ Double Perovskite," *Materials*, vol. 9, p. 154, 3 Mar. 2016.

[72] C. Zhu, X. Liu, C. Yi, D. Yan, and W. Su, "Electrochemical performance of $prbaco_2o_{5+\delta}$ layered perovskite as an intermediate-temperature solid oxide fuel cell cathode," *Journal of power sources*, vol. 185, no. 1, pp. 193–196, 2008.

[73] B. Lin, Y. Dong, R. Yan, S. Zhang, M. Hu, Y. Zhou, and G. Meng, "In situ screen-printed $BaZr_{0.1}Ce_{0.7}Y_{0.2}O_{3-\delta}$ electrolyte-based protonic ceramic membrane fuel cells with layered SmBaCo2O5+x cathode," *Journal of power sources*, vol. 186, pp. 446–449, Jan. 2009.

[74] B. Lin, S. Zhang, L. Zhang, L. Bi, H. Ding, X. Liu, J. Gao, and G. Meng, "Prontonic ceramic membrane fuel cells with layered $GdBaCo_2O_{5+x}$ cathode prepared by gel-casting and suspension spray," *Journal of power sources*, vol. 177, pp. 330–333, 1 Mar. 2008.

[75] Y. Lin, R. Ran, C. Zhang, R. Cai, and Z. Shao, "Performance of $PrBaCo_2O_{5+\delta}$ as a proton-conducting solid-oxide fuel cell cathode," *The journal of physical chemistry. A*, vol. 114, pp. 3764–3772, 25 Mar. 2010.

[76] G. Kim, S. Wang, A. J. Jacobson, L. Reimus, P. Brodersen, and C. A. Mims, "Rapid oxygen ion diffusion and surface exchange kinetics in $PrBaCo_2O_{5+x}$ with a perovskite related structure and ordered a cations," *Journal of materials chemistry*, vol. 17, pp. 2500–2505, 3 Apr. 2007.

[77] H. Zhao, Y. Zheng, C. Yang, Y. Shen, Z. Du, and K. Świerczek, "Electrochemical performance of $Pr_{1-x}Y_xBaCo_2O_{5+\delta}$ layered perovskites as cathode materials for intermediate-temperature solid oxide fuel cells," *International journal of hydrogen energy*, vol. 38, pp. 16365–16372, 13 Dec. 2013.

[78] A. Tarancón, D. Marrero-López, J. Peña Martínez, J. C. Ruiz-Morales, and P. Núñez, "Effect of phase transition on high-temperature electrical properties of $GdBaCo_2O_{5+x}$ layered perovskite," *Solid State Ionics*, vol. 179, no. 17–18, pp. 611–618, 2008.

[79] G. Aurelio, R. D. Sánchez, J. Curiale, and G. J. Cuello, "High-temperature behavior of Sr-doped layered cobaltites $YBa_{1-x}Sr_xCo_2O_{5.5}$: phase stability and structural properties," *Journal of physics. Condensed matter: an Institute of Physics journal*, vol. 22, p. 486001, 8 Dec. 2010.

[80] T. Vogt, P. M. Woodward, P. Karen, B. A. Hunter, P. Henning, and A. R. Moodenbaugh, "Low to High Spin-State Transition Induced by Charge Ordering in Antiferromagnetic $YBaCo_2O_5$," *Physical review letters*, vol. 84, p. 2969, 27 Mar. 2000.

[81] P. S. Anderson, C. A. Kirk, J. Knudsen, I. M. Reaney, and A. R. West, "Structural characterisation of $REBaCo_2O_{6-\delta}$ phases ( RE = Pr, Nd, Sm, Eu, Gd, Tb, Dy, Ho)," *Solid State Sciences*, vol. 7, pp. 1149–1156, 2005.

[82] J. Seddon, E. Suard, and M. A. Hayward, "Topotactic Reduction of $YBaCo_2O_5$ and $LaBaCo_2O_5$: Square-Planar Co(I) in an Extended Oxide," *Journal of the American Chemical Society*, vol. 132, no. 8, pp. 2802–2810, 2010. PMID: 20131833.

[83] K. Knížek, Z. Jirák, J. Hejtmánek, M. Veverka, M. Maryško, B. C. Hauback, and H. Fjellvåg, "Structure and physical properties of Y Co O 3 at temperatures up to 1000 K," *Physical review. B, Condensed matter*, vol. 73, p. 214443, 28 June 2006.

[84] A. J. Jacobson and J. L. Hutchison, "An investigation of the structure of 12HBaCoO2.6 by electron microscopy and powder neutron diffraction," *Journal of solid state chemistry*, vol. 35, pp. 334–340, 1 Dec. 1980.

[85] X. Zhang, H. Hao, and X. Hu, "Electronic transport properties of $YBaCo_2$-$xCuxO_{5+\delta}$ ($0 \leq x \leq 1$) at high temperature," *Physica. B, Condensed matter*, vol. 403, pp. 3406–3409, 1 Oct. 2008.

[86] M. Valldor and M. Andersson, "The structure of the new compound YBaCo4O7 with a magnetic feature," *Solid State Sciences*, vol. 4, no. 7, pp. 923–931, 2002.

[87] P. Chizhov and E. Antipov 2005.

[88] H. Hao, B. Chen, L. Zhao, and X. Hu, "Oxygen removal from nitrogen using $YBaCo_2O_{5+\delta}$ adsorbent," *The Korean journal of chemical engineering*, vol. 28, pp. 563–566, 26 Nov. 2010.

# Appendices

# Appendix A

# Ex situ TGA

Oxygen content obtained from TGA data. Legend shows which atmosphere and date of the experiment.

Confirmation of reduction of cobalt to $Co^0$ (yttrium and barium still present as $Y^{3+}$, $Ba^{2+}$) can be seen in **Figure A.1** showing the diffraction pattern of the reduced material. The blue line correspond to metallic cobalt.

The figure shows three patterns, one just after reduction and two after some time. In all patterns cobalt is metallic, and barium and yttrium form different oxides or hydroxides. The reason why the pattern change with time, and that the second measurement just after reduction is excluded is that BaO is hygroscopic. The sample got spoiled as it expanded when BaO hydrated. The curved XRD sample can be seen in **Figure A.2**. The sample was weighed just after reduction giving minimal time for hydration of BaO to assure the right oxygen content was found.

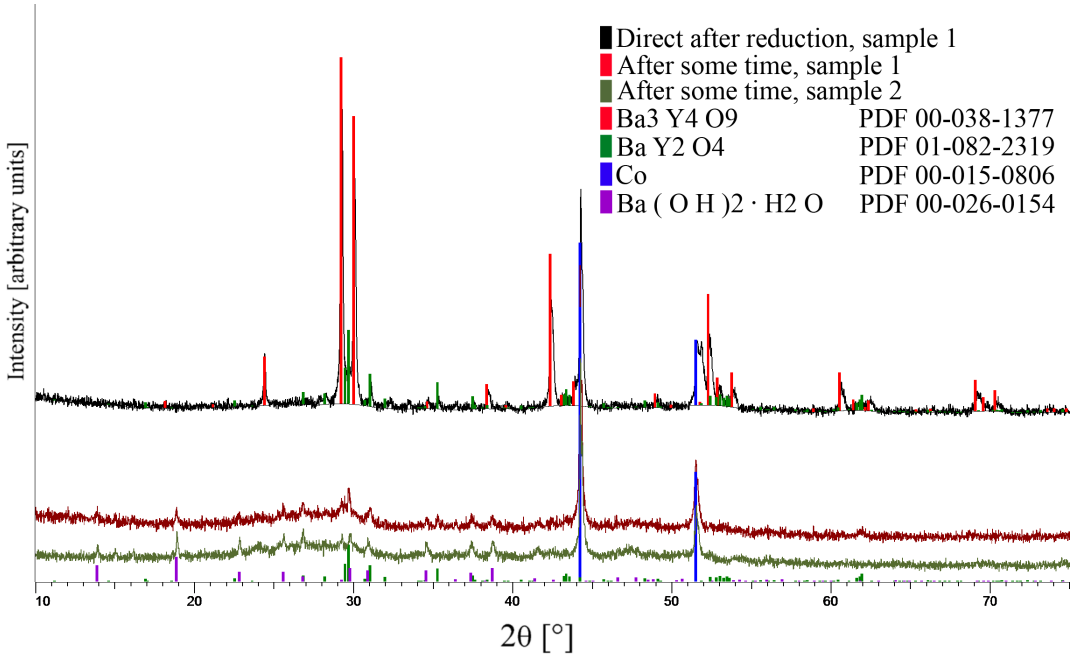


**Figure A.1:** XRD pattern after reduction of YBCO in 5 % $H_2$ in Ar. The presence of only $Ba_3Y_4O_9$, $BaY_2O_4$ and Co after reduction show that YBCO was reduced to $Ba^{2+}$, $Y^{3+}$ and Co as assumed in the calculation of initial oxygen content.

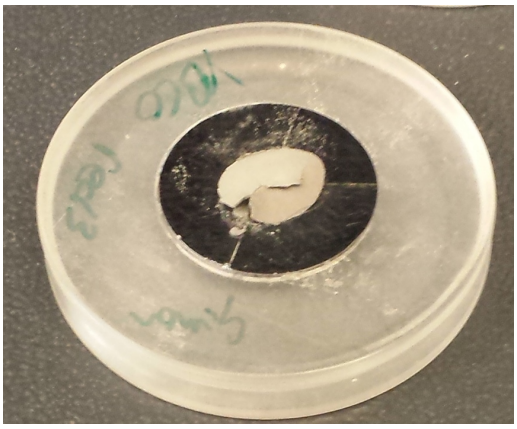

**Figure A.2:** XRD sample spoiled by expansion related to hydration of BaO.

# Appendix B

# Solid state synthesis

During the project work conducted fall 2015 it was believed that the material synthesised was obtained phase-pure. After looking more carefully at the diffraction pattern from literature, it was clear that impurities was indexed as the main phase. What was thought to be a phase-pure material, since it matched the literature was not phase-after all. This was evident from comparing other patterns of $YBaCo_2O_{5+\delta}$, yttria and barium cobaltite with the wrong diffraction pattern from literature.

Synthesis of the material was tried at 900 °C, 1000 °C and 1100 °C. Calcination at 900 °C did not lead to any formation of $YBaCo_2O_{5+\delta}$, while secondary phases were present together with the main phase at 1000 °C and 1100 °C. Repeated grinding and calcination increased phase-purity, but only to some extent. Calcination temperature of 1000 °C was mostly used to avoid sintering.

The synthesis was restarted several times, without yielding a phase pure material. Ph.D. candidates from the group recommended to investigate the microstructure of precursors. This was done with SEM, and it was found that the yttria precursor was very coarse. Finer precursors was therefore used in later synthesis. Pictures of the coarse yttria are shown in **Figure B.1**. Picture of the mix of precoursors are shown in **Figure B.2**, where seen some white dots can be seen. To remove these several rounds of grinding was done before calcination. By only mixing either yttrium (white) and cobalt (black), or barium (white) and cobalt (black) it was seen that the white dots were of yttria.

Still several synthesis trials failed. Other master students at the group used machines to mill and mix their materials, but this was chosen to avoid initially due to the risk of contamination. After two months with hand grinding for up to several hours per calcination step per batch, ball milling was introduced. Both to mill yttria, and to properly mix the materials. As can be seen on **Figure B.3** the milling-balls were old and hard to clean, to avoid contamination only the smooth balls which could be easily cleaned was used..

Supervisor told that a phase-pure material could be obtained after only one calcination steps, and some batches were tried with only calcining once. Even though the material was both ball milled and ground by hand one calcination step could not yield a phase-pure material. After increasing calcination time from 12 h to 48 h, in addition to first grind yttria before adding the other precursors, phase-purity

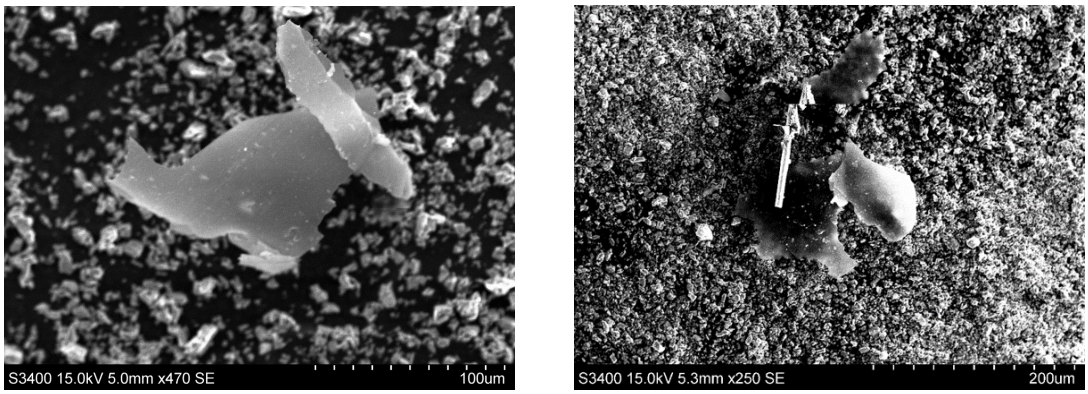


**(a)** **(b)**

**Figure B.1:** SEM picture of coarse precursor yttria.

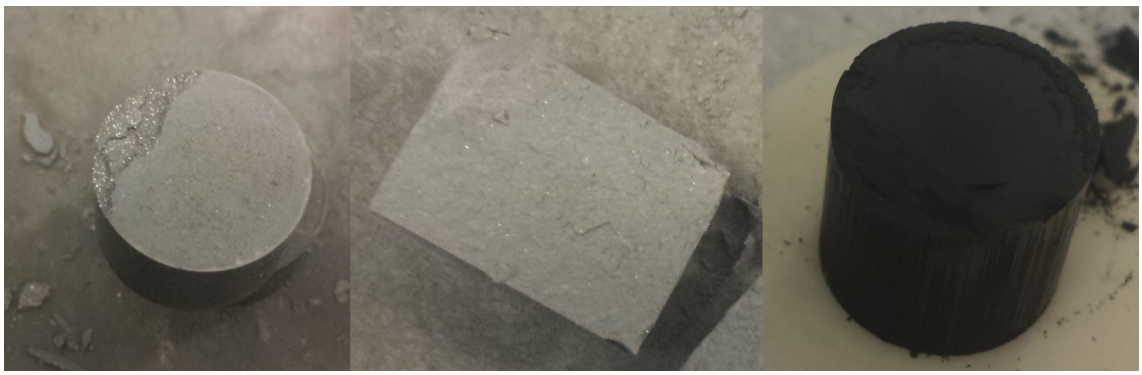

**(a)**

**Figure B.2:** Picture of mix of precursor showing increasing homogeneity with fewer white dots from yttria.

**(a)**

**Figure B.3:** Picture of milling balls after initial cleaning, indicating that balls are worn out with rough surface. If the balls were clean they would be white.

increased. By grinding and calcining multiple times phase-purity increased further.